UC Berkeley
UC Berkeley Electronic Theses and Dissertations

Title

Microfluidic Devices for Multimodal Single-Cell Biophysical Phenotyping

Permalink

https://escholarship.org/uc/item/21s8257b

Author

Lai, Andre

Publication Date

2024

Peer reviewed|Thesis/dissertation

eScholarship.org Powered by the California Digital Library
University of California

Microfluidic Devices for Multimodal Single-Cell Biophysical Phenotyping

by

Andre Lai

A dissertation submitted in partial satisfaction of the

requirements for the degree of

Joint Doctor of Philosophy
with the University of California, San Francisco

in

Bioengineering

in the

Graduate Division

of the

University of California, Berkeley

Committee in charge:

Professor Lydia L. Sohn, Chair
Professor Matthew L. Kutys, UCSF
Professor Mohammad R. K. Mofrad

Spring 2024

Microfluidic Devices for Multimodal Single-Cell Biophysical Phenotyping

Copyright © 2024, by the author(s).

All rights reserved.

Permission to make digital or hard copies of all or part of this work for personal or classroom use is granted without fee provided that copies are not made or distributed for profit or commercial advantage and that copies bear this notice and the full citation on the first page. To copy otherwise, to republish, to post on servers or to redistribute to lists, requires prior specific permission.

Abstract

Microfluidic Devices for Multimodal Single-Cell Biophysical Phenotyping

by

Andre Lai

Doctor of Philosophy in Bioengineering

University of California, Berkeley

Professor Lydia L. Sohn, Chair

The physical attributes of a cell can serve as label-free biomarkers of cellular state and behavior. In cancer, for example, malignant cells are known to be significantly more deformable than their non-malignant counterparts. I describe the development of two microfluidic platforms: Multi-Zone Visco-NPS (mz-visco-NPS) and Combo-NPS. Both approaches utilize Node-Pore Sensing (NPS), in which the ohmic resistance across a microfluidic channel is used to characterize and measure single-cell parameters. Mz-visco-NPS uses multiple sinusoidal contraction segments aligned in series to periodically deform passing cells at increasing perturbation frequencies. Using this platform, I measure the rheology of human breast epithelial cells, namely the elastic storage (G') and viscous loss (G") moduli. Combo-NPS uses DNA-directed patterning for the positioning of surface-immobilized antibodies upstream of a linear contraction channel. In this design, I demonstrate the ability to measure single-cell surface-marker expression, in addition to mechanical properties such as diameter, elasticity, and viscosity. I generate paired immuno- and mechano- phenotype datasets on single cells that enable new approaches for subpopulation screening and correlation studies. Ultimately, both platforms are powerful tools for moderate-throughput, multimodal, single-cell biophysical phenotyping.

To my family:

My JJ, my parents and my sisters.

Contents

Contents **ii**

List of Figures **v**

List of Tables **vii**

1 Introduction **1**

2 Background and Motivation **3**
2.1 Microfluidic Systems 3
2.1.1 Physical Principles 5
2.1.2 Advantages and Disadvantages 10
2.1.3 Modern Applications in Biomedical Research 11
2.2 Single-Cell and Multimodal Analysis 12
2.3 Biophysical Phenotyping 15
2.3.1 Significance of Biomechanics and Mechanobiology 15
2.3.2 Conventional Tools for Biophysical Phenotyping 16
2.3.3 Modern Microfluidic Approaches for Single-Cell Biophysical Phenotyping 18
2.3.4 Research and Clinical Applications Of Single-Cell Biophysical Phenotyping 19
2.4 Conclusion 21

3 Methods: Node-Pore Sensing **22**
3.1 Resistive Pulse Sensing (RPS) 22
3.1.1 Background and Theory 23
3.2 Node-Pore Sensing (NPS) 24
3.2.1 Mechano-NPS and Visco-NPS 25
3.3 Microfluidic Device Fabrication 26
3.3.1 Channel Fabrication 27
3.3.2 Electrode Patterning 28
3.3.3 Device Bonding 29
3.4 Hardware Implementation 30

3.4.1 Multi-Zone Electronic Hardware Configuration . . . 31
3.4.2 Experimental Hardware and Operation . . . 33
3.5 Software Implementation . . . 34
3.5.1 Data Acquisition . . . 34
3.5.2 Signal Processing . . . 35
3.5.3 Signal Analysis . . . 36
3.6 Conclusion . . . 38

4 Multi-Zone Viscoelastic Node-Pore Sensing (mz-visco-NPS) 39
4.1 Prior Work and Motivation . . . 39
4.1.1 Significance of Single-Cell Viscoelasticity . . . 40
4.2 Approach and How It Works . . . 40
4.3 Theory and Modeling . . . 42
4.3.1 Dynamic Viscoelasticity . . . 42
4.3.2 Stress Model . . . 45
4.4 Design and Experimental Methods . . . 46
4.4.1 Channel Design Overview . . . 47
4.4.2 Cell Culture and Sample Preparation . . . 48
4.4.3 Data Acquisition . . . 50
4.4.4 Signal Processing and Analysis . . . 50
4.5 Results and Discussion . . . 51
4.5.1 Measuring the Disruption of the Actin Cytoskeleton . . . 51
4.5.2 Evaluating the Effect of Zone Arrangements on mz-visco-NPS Measurements . . . 54
4.5.3 Comparing the Viscoelastic Properties of Multiple Breast Epithelial Cell Types . . . 54
4.5.4 Uncovering Viscoelastic Differences Among Average and High Rick Human Mammary Epithelial Cells (HMEC) . . . 56
4.5.5 Discussion . . . 59
4.6 Conclusion . . . 63

5 Combo Node-Pore Sensing (Combo-NPS): Integrated Surface Marker Screening and Mechanophenotyping 64
5.1 Prior Work and Motivation . . . 65
5.1.1 Significance of Surface Markers . . . 65
5.1.2 NPS with Surface Immobilized Antibodies . . . 67
5.2 Approach and How It Works . . . 68
5.3 Theory and Modeling . . . 70
5.4 Antibody Labeling and Surface Functionalization . . . 72
5.4.1 Protein Labeling Approaches . . . 73
5.4.2 Protein Purification Approaches . . . 74
5.5 Fabrication and Experimental Methods . . . 79

5.5.1 Channel Design and Fabrication 79
5.5.2 Cell Culture and Preparation 81
5.5.3 Experimental Methods 81
5.5.4 Signal Processing and Analysis 82
5.6 Results and Discussion 84
5.6.1 Inlet Pressure Characterizations 85
5.6.2 Malignant MCF-7 Versus Non-Malignant MCF-10A 87
5.6.3 Screening of Heterogeneous Cell Mixtures 89
5.6.4 Discussion 90
5.7 Conclusion 93

6 Conclusions and Future Directions **94**
6.1 Summary 94
6.2 Future Directions 96
6.3 Concluding Remarks 97

References **99**

List of Figures

2.1 Interdisciplinary Overview 4
2.2 The Length Scale of Microfluidics 5
2.3 Laminar vs. Turbulent Flow 7
2.4 Microfluidic Advantages and Applications 10
2.5 Bulk Versus Single-Cell Analysis 14
2.6 Comparison of Single-Cell Mechanical Phenotyping Techniques 18

3.1 Computational Simulation of Electric Field Across A Narrow Pore 23
3.2 Design and Signal Differences Between RPS and NPS. 25
3.3 Linear Versus Sinusoidal Contraction Channels 26
3.4 Fabrication Steps for Molding A Microfluidic Channel 27
3.5 Electrode Fabrication Steps 29
3.6 Plasma Bonding 30
3.7 Schematic of Multi-Zone Data Acquisition Hardware 31
3.8 Multi-Zone Hardware Circuit Diagram 33
3.9 Live Graphical Readout During Data Acquisition 36
3.10 Signal Processing and Analysis Pipeline 37

4.1 Multi-Zone Visco-NPS Overview 41
4.2 Example of Viscoelastic Response to Dynamic Oscillatory Input 43
4.3 COMSOL Modeling of Cell in a Contraction Zone 47
4.4 mz-visco-NPS Detects Actin Filament Perturbations in MCF-7 Cells 52
4.5 Summary of Average Viscoelastic Properties for MCF-7 Cells Treated with Latrunculin-A (Lat-A) 53
4.6 Effect of Channel Geometry on Measured Storage Modulus 55
4.7 Comparison of Viscoelastic Properties Among Three Breast Epithelial Cell Lines 57
4.8 Summary of Average Viscoelastic Properties for 3 Breast Epithelial Cell Types. 58
4.9 Viscoelastic Properties of Primary Human Mammary Epithelial Cells (HMECs) with and without the BRCA1 Mutation. 60
4.10 Summary of Average Viscoelastic Properties for Primary Human Mammary Epithelial Cell (HMEC) Strains 61

5.1 Significance of Surface Markers 66

5.2 Previous Approaches Using NPS to Screen Surface Markers 67
5.3 Combo-NPS Platform Overview 69
5.4 Computational Fluid Dynamics (CFD) Simulation of Combo-NPS Fluidic Geometry 71
5.5 Comparison of Protein Labeling Approaches 75
5.6 Protein Filtering Approaches 76
5.7 Evaluation of Protein Filtering Approaches 78
5.8 DNA Patterning and Plasma Shield 80
5.9 On-Chip DNA Patterning of Antibodies 82
5.10 Combo-NPS Event Cases 83
5.11 Combo-NPS Surface Marker Expression Gating 84
5.12 Combo-NPS Input Pressure Characterization 86
5.13 Mechanophenotype and EpCAM Expression of MCF-7 and MCF-10A Cells . . . 87
5.14 Simultaneous Mechano- & Immuno- Phenotype of Heterogenous Cell Populations 91

List of Tables

3.1 Multi-Zone Hardware Component Catalog. 32

4.1 mz-visco-NPS channel dimensions and strain applied to each cell type. 48
4.2 Microfluidic channel lengths and calculated effective diameters for 3-, 4-, and 5-zone devices. 48
4.3 Human Mammary Epithelial Cells (HMEC) Used In This Study. 49

5.1 DNA Oligo Sequences For Antibody Labeling. 73
5.2 Combo-NPS Specific Antibody-Crosslinker-Oligo Conjugations. 74
5.3 Combo-NPS Microfluidic Channel Dimensions Used For Each Cell Type. 79

Acknowledgments

This dissertation, a culmination of my doctoral journey, has been a pursuit that involved the support, dedication, and encouragement from countless people. Here, I wish to recognize and express my gratitude toward several individuals.

First, I would like to thank my advisor, Dr. Lydia Sohn, for providing me the privilege and opportunity to pursue and perform a graduate degree at UC Berkeley. I am grateful for the trust and freedom she provided when guiding me and my research. I would also like to sincerely thank my many colleagues in the Sohn Lab: Dr. Roberto Falcón-Banchs, Dr. Molly Kozminsky, Dr. Thomas Carey, Nate Liu, Dr. Brian Li, Dr. Kristen Cotner, Dr. Sean Kitayama, Rachel Rex, Stephanie Eberly, Pierre-Jean Croux, Joy Chen, Jessica Ortiz, Taylor Thomsen, and Chang Chen. Thank you for being amazing colleagues and friends throughout my graduate career, both inside and outside the lab.

I would like to thank my undergraduate research mentors: Dr. Aaron Streets and Dr. Nicolas Altemose. They believed in me from the onset, and formed the very foundation on which my academic research career rests–I am forever thankful. I would like to thank my qualifying exam and dissertation committee members for volunteering their time and knowledge in support of my scientific pursuits: Dr. Mohammad Mofrad, Dr. Matthew Kutys, and Dr. Dorian Liepmann. I would also like to thank the program's head graduate advisor, Dr. Steven Conolly, and the program admins, Victoria Starrett and Rocío Sanchez. Finally, I would like to thank my funding sources, Hearts to Humanity Eternal (H2H8) and the Siebel Scholars foundation. The weekly lunches at the Faculty Club, sponsored by H2H8, were of particular significance: the value of a fun, routine meal with friends and colleagues cannot be underscored enough.

I would like to thank my lifelong partner, Jasmine Jan. As we both embarked on our academic journey together, Jasmine has walked lock-step with me through thick and thin. She has been my advocate from day one. I am and will always be eternally grateful for her remarkable love, support, and resilience.

Finally, I would like to thank my mom, dad, and sisters, Heidi and Mandy. To my Mom and Dad, thank you for your unconditional love and support, and for raising me with all the resource in life to make this accomplishment a possibility. To my older sisters, thank you for supporting your younger brother as he decided to spend almost a decade at Berkeley.

Chapter 1

Introduction

The broader objective of this work is to contribute new methods, devices, and approaches to the wider bioengineering community. Advancements in biology and medicine are inextricably linked with advancements in engineering and biotechnology. From the inception of the microscope in the late 16th century to next-generation sequencers of the 21st century, the introduction and application of new tools have, and continue to, form the basis of biological research and development. The work described here is another innovative addition to the vast toolkit already at the disposal of modern scientists and engineers. It is meant to complement and enable new biological inquiries, contributing to the enduring cycle of inventing unique tools and approaches to answer previously inaccessible questions.

This dissertation is centered upon two primary concepts: microfluidics and single-cell biophysical phenotyping. The former is the methodology employed while the latter is the application studied. The marriage of these two concepts forms the basis of this dissertation: from conception and design, to fabrication, validation, and finally, implementation and results. Specifically, using "resistive pulse sensing" and "node-pore sensing (NPS)", I measure the ohmic resistance across sections of a microfluidic channel. These electrical methods, coupled with characteristic channel designs and novel surface functionalizations, enable the unique quantification of single-cell biophysical phenotypes.

The immediate application is to associate cellular biophysical phenotypes with specific biological states in both health and disease. Such information could serve as a biophysical biomarker, in which complex cellular states and behaviors can be identified from the rapid characterization of a single cell's biophysical properties. This would be highly advantageous in both research and clinical settings, where identifying and quantifying biophysical parameters can serve as a new avenue for scientific exploration or as a new metric for patient diagnosis.

The subsequent chapters in this dissertation describe the body of work completed towards the aforementioned application, with the specific goals of:

1. Developing unique microfluidic tools for the multimodal measurement of single-cell biophysical properties.
2. Characterizing the relationships among single-cell biophysical properties and various cellular attributes.

This disseration is organized as follows:

- In Chapter 2, I detail the background related to the work described in this dissertation, including relevant prior work and motivation. I delve into the two core concepts of this dissertation: microfluidics and single-cell biophysical phenotyping, providing an essential foundation for subsequent chapters.
- In Chapter 3, I describe the approaches employed throughout this work. I review the theoretical principles behind the main technologies used, the various design and fabrication processes, and delve upon the practical implementation of the methods.
- In Chapter 4, I describe the first core component of this dissertation: Multi-Zone Viscoelastic Node-Pore Sensing (mz-visco-NPS). Mz-visco-NPS is a custom microfluidic platform for measuring the multi-frequency rheological properties of single-cells. From introduction to discussion and conclusion, I extensively describe all aspects of this platform, including background, theory, and data from measuring human mammary epithelial cells.
- In Chapter 5, I describe the second core component of this dissertation: Combination Node-Pore Sensing (Combo-NPS). This is another custom microfluidic platform for the multimodal measurement of single cell biophysical properties. Specifically, I demonstrate simultaneous single-cell analysis of mechanical properties and surface-marker expression. Similar to Chapter 4, I thoroughly detail the unique aspects of this platform, ranging from design conception to experimental results.
- In Chapter 6, I conclude this dissertation by reviewing the background, approach, and development of mz-visco-NPS and combo-NPS. I summarize the primary results and discuss the implications of the findings. Additionally, I present future directions and a general outlook, recommending next steps for the continuation of this research.

Overall, this dissertation is the culmination of years of work, building off the advancements made by a multitude of scientists and engineers, and countless peer-reviewed publications. It is the amalgamation of a few core technologies, namely Node-Pore Sensing (NPS) and DNA-Directed Pattering, and details the development of more integrated and more capable tools. These powerful tools, aimed at measuring the diverse biophysical phenotype of cells, can help address new inquiries related to single-cell mechanics and surface properties, fueling further progress in biomedical research.

Chapter 2

Background and Motivation

This chapter will review all relevant material regarding microfluidic single-cell biophysical phenotyping. I describe prior work achieved in this area, motivate the significance of studying single-cell biophysical phenotypes, and provide additional context and perspectives that form the basis of this dissertation.

This chapter is divided into three primary sections, addressing the following questions:

- What are microfluidics? How are they utilized in science and why?
- What is the significance of multimodal single-cell analysis?
- What is biophysical phenotyping and how is it relevant in modern biomedical research?

Ultimately, the work presented in this dissertation is inherently interdisciplinary **(Figure 2.1)**, ranging from laminar flow physics to single-cell biology. The questions above are intended to lay a foundation and organize the fundamentals needed to understand the approach and results presented in subsequent chapters. I conclude this chapter by summarizing the critical aspects of microfluidic single-cell biophysical phenotyping and transition into a brief discussion of my approach employing node-pore sensing (NPS) [1].

2.1 Microfluidic Systems

Microfluidics is defined as the manipulation of fluids at the sub-millimeter scale, typically on the order from 1 to 500 microns **(Figure 2.2)**. Such manipulation is often accomplished using micro-machined channels, in conjunction with pumps and valves that enable discrete control. Microfluidics forms the basis for many biomedical microelectromechancial systems (Bio-MEMS), synonymous with Lab-On-A-Chip (LoC) Systems, in which bench-top experimental processes are integrated and miniaturized onto a single "chip". This miniaturization

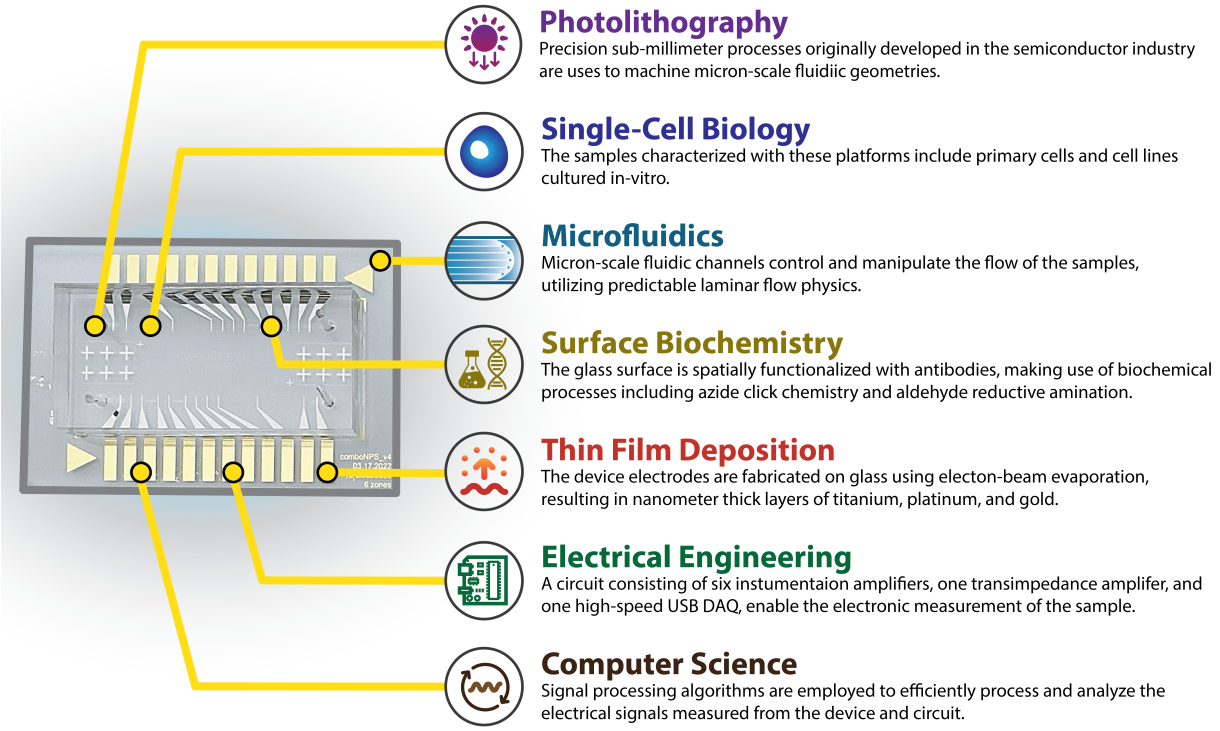


Figure 2.1: Scientific Disciplines and Processes Integrated In This Work. The engineered platforms described in this dissertation integrate multiple scientific fields and processes, including single-cell biology, photolithography, microfluidics, surface biochemistry, thin-film deposition, electrical engineering, and computer science.

has distinct benefits, including reduced sample and reagent volumes, and faster reaction times. Such benefits are described in more detail in the following subsections.

For context, an example of a commercial "microfluidic" devices that resides in offices worldwide is the inkjet printer [2]. Inkjet printers rely on a steady stream of picoliter droplets that are precisely ejected out of a microfluidic nozzle and onto a sheet paper. The microfluidic component itself is a continuous droplet generator, in which a thermal or piezoelectric component rapidly creates and ejects fluid droplets. Today, microfluidic devices are common in research, clinical, and at-home settings. Lateral flow tests [3, 4], such as at-home pregnancy tests or at-home COVID-19 tests, rely on capillary action to wick microliters of sample across a simple assay architecture. Flow cells commonly used in research equipment, such as next-generation sequencing instruments, rely on microfluidic components to route samples, reagents, and waste with precision [5]. Finally, microfluidic technologies are commonly found in point-of-care devices, such as glucometers and blood-analyzers [6, 7]. Once more, theses devices rely on a microfluidic consumable for the analysis of biofluid samples.

Overall, microfluidics deals with the handling of small amounts of fluid in precise and con-

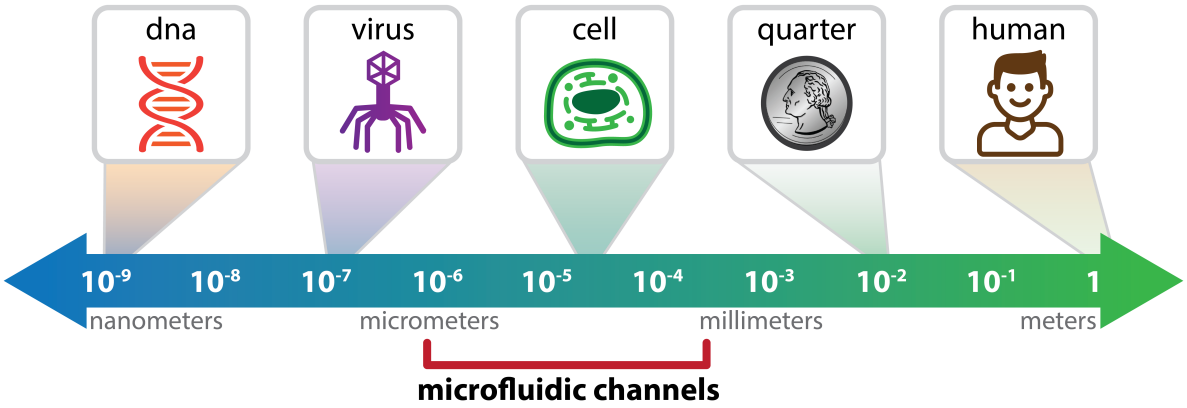


Figure 2.2: Comparing the Length Scale of Microfluidics. Microfluidic devices are typically on the order of 1 to 500 micrometers. For comparison: a human is around 1 to 2 meters tall; a typical United States quarter is approximately 25 mm in diameter; the average human cell is 20 to 50 microns wide. At the smallest end, a virus is 100 nanometers in diameter and a single DNA molecule is 2 nm in diameter. Overall, microfluidic channels are approximately 1,000 times larger than the diameter of a DNA molecule or approximately 100,000 times smaller than the height of a human.

trolled ways. It is an engineering specialty that has burgeoned not only in academic research, but also in commercial applications. As a growing scientific discipline, microfluidics remains essential for conducting innovative biomedical research at the microscale. The following subsections will detail the physical principles that are inherent to fluids at the micro scale and explore the pros and cons of microfluidic systems in modern biomedical applications.

2.1.1 Physical Principles

Flow at the micro-scale has significantly different behavior than flow at the macro-scale. The physical foundation of such behavior is based on fluid mechanics and various transport phenomena. Key facets of this microfluidic behavior include:

- Predictable Laminar Flow
- Dominance of Diffusion
- Unique Passive- and Active-Transport Mechanisms

By understanding and manipulating these physical behaviors, countless innovative devices have been developed, such as droplet microfluidics [8], cell sorters [9], and organ-on-a-chip technologies [10]. Such microfluidic advances have enabled a truly wide breadth of functionality in biology, chemistry, and physics.

The overarching mathematical expression governing the motion of viscous, incompressible, Newtonian fluids is the Navier-Stokes equations [11, 12]. It consists of partial differential equations that equate changes in momentum (due to changes in acceleration) to the sum of surface forces (pressure and viscosity) and body forces (gravity and electrostatics). The solution to the equations is a flow velocity vector field: a set of vectors, each consisting of a direction and magnitude that describe the velocity of the fluid at a specific time and at a specific spatial position. Alternatively, uniform flow in a microfluidic channel can be calculated using:

$$Q = uA \tag{2.1}$$

where Q is the volumetric flow rate in m^3/s, u is the fluid velocity, and A is the cross-sectional area of the flow. In an analogy to Ohm's Law in electronics, volumetric flow rate can also be described by:

$$\Delta P = QR_{hyd} \tag{2.2}$$

where ΔP is the change in pressure and R_{hyd} is the hydrodynamic resistance of the channel. Hydrodynamic resistance is dependent on the channel's cross-sectional area [13]. For a standard rectangular channel in microfluidics, hydrodynamic resistance can defined as:

$$R_{hyd} = \frac{1}{1 - 0.63(h/w)} \frac{12\mu L}{h^3 w} \tag{2.3}$$

where μ is the dynamic viscosity of the fluid, h is the channel height, w is the channel width, and L is the channel length. Together, Equations 2.1, 2.2, and 2.3 enable calculations on fluid motion that are vastly more simple than solving the Navier-Stokes equations.

At the heart of microscale fluid behavior is laminar flow. Laminar flow is characterized by smooth, predictable motion. In microchannels, laminar flow is the dominant behavior, inherently differently from what one might observe with macroscale flow. In macroscale systems, fluid can undergo turbulent flow: motion that is chaotic, irregular, and unpredictable. Systems dominated by laminar flow versus turbulent flow can be described by the Reynolds number, a dimensionless quantity that compares inertial forces (due to fluid acceleration) to viscous forces (due to resistance to flow) [14, 15]. The Reynolds number (Re) is defined as:

$$Re = \frac{\rho u L}{\eta} \tag{2.4}$$

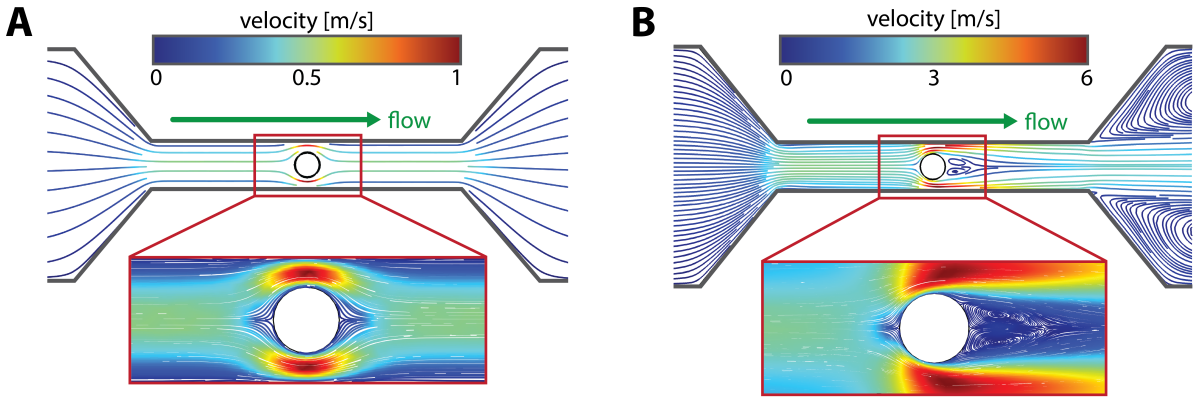


Figure 2.3: Computational Fluid Dynamics (CFD) Simulations of Laminar Versus Turbulent Flow. (A) COMSOL Multiphysics® [17] single-phase fluid simulations of laminar flow in a 15 µm pore around a cylinder. Under laminar flow conditions with a no-slip boundary condition, the streamlines closely follow the cylindrical surface, with no boundary layer separation. In this scenario, the primary force on the cylinder is from frictional drag. (B) COMSOL Multiphysics single-phase fluid simulations of turbulent flow, using the k-ε turbulent flow model interface [18]. To achieve turbulent flow, the geometry was isotropically scaled 10,000-fold, while the inlet pressure was increased by 10-fold, resulting in a 100,000-fold increase in Reynold's number. Under turbulent flow conditions, the flow separates from the boundary layer around the cylinder, creating a wake that takes the form of unpredictable eddies and vortices. This phenomena creates a pressure gradient across the cylinder, resulting in an additional drag force known as pressure drag.

where ρ is the fluid density, u is the fluid velocity, L is the characteristic length, and η is the dynamic viscosity. A system with $Re < 2000$ is considered to behave with fully-developed laminar flow [14–16]. In microfluidics, the Reynolds number is exceptionally low, often below 1, due to the small channel dimensions (L) and slow flow rates (u). As a result, viscous forces (η) prevail over inertial forces. The fluid moves in parallel layers (streamlines), without significant mixing. **Figure 2.3A** obtained using computational fluid dynamics, shows the simulated laminar flow in a microchannel as fluid flows around a stationary cylinder. The streamlines remain parallel across the microchannel, with a predictable and orderly rise in velocity as they are compressed around the cylinder. In contrast, turbulent flow is designated as systems with $Re > 3500$ [16]. In this case, inertial forces dominate, resulting in disorderly flow with unpredictable fluid streamlines. **Figure 2.3B** shows the simulated flow under the same operating conditions as **Figure 2.3A**; however, the dimensions were isotropically scaled 10,000-fold and the inlet pressure scaled 10-fold, resulting in a 100,000-fold increase in Re. This causes the flow to transition from laminar to turbulent, resulting in chaotic streamlines that are no longer uniform and parallel. Note the non-uniform fluid velocity around the stationary cylinder, caused by flow separation from the cylinder. This separation creates a low-pressure region consisting of random eddies and vortices.

Laminar flow is considered both an advantage and disadvantage for microfluidics. On the one hand, the predictability of laminar flow is advantageous for designing and modeling microfluidic behavior, enabling precise control over fluid movement. On the other hand, laminar flow can hinder fluidic mixing. In macroscale systems, turbulence naturally promotes mixing by dispersing solutes. In microchannels, achieving efficient mixing requires deliberate strategies, such as exploiting diffusive processes [19].

The dominance of diffusion is another central microfluidic behavior. Diffusion is the net movement of particles, such as atoms, ions, or molecules, from an area of higher concentration to an area of lower concentration. This process occurs spontaneously due to the inherent randomness of the diffusing entities (Brownian motion) and is driven by a gradient. This gradient can be, for example, concentration, temperature, or pressure. Diffusion can be described by Fick's 1st law, which relates diffusive flux (amount of substance per unit area per unit time) to the gradient of the concentration [14, 15]. Fick's 1st law, in one dimension, is:

$$J_i = -D_{ij}\frac{\partial C_i}{\partial x} \tag{2.5}$$

where J_i is the diffusive flux of solute i, D_{ij} is the diffusion coefficient of solute i in solvent j (with units of area per time), and $\frac{\partial C_i}{\partial x}$ is the spatial concentration gradient of solute i across dimension x. The negative sign in Fick's 1st law is necessary to point the flux in the correct direction: when ∂C_i is positive, the concentration increases as x increases. The particle flux is in the opposite direction, from the region of high to the region of low concentration. In a low Reynolds number environment, the diffusion coefficient, or diffusivity, of a spherical particle can be described by the Stokes-Einstein equation [20]:

$$D_{ij} = \frac{k_b T}{6\pi\eta r} \tag{2.6}$$

where k_b is the Boltzmann constant, T is absolute temperature, η is dynamic viscocity, and r is the radius of the the spherical particle. From Equation 2.5 and 2.6, we see that diffusion is primarily a function of concentration, length, temperature, and solvent viscosity. Finally, the characteristic length for diffusion in one dimension from a single point source can be described by:

$$\left\langle x^2 \right\rangle = 2D_{ij}t \tag{2.7}$$

where x is the characteristic diffusion length in one dimension, D_{ij} is the diffusion coefficient, and t is time. For reference, the typical diffusion coefficient of biological compounds, such

as small molecules and proteins, in water at room temperature is on the order of 1 to 500 $\mu m^2/s$ [21]. From Equation 2.7, we find that the approximate diffusion distance of a typical biological compound in the timeframe of 1 second is on the order of 1 to 30 μm, which is on the length scales of microfluidics. Thus, for microfluidic devices, diffusion plays an outsized role in the transport of biological and chemical solutes. The small length scales and lack of turbulent flow means that, in most cases, the incorporation of solutes in a microfluidic channel is dominated by diffusive mixing.

The final central characteristic of microfluidics is the unique passive and active transport mechanisms enabled by the micro length scale. Passive transport mechanisms are inherent to the system itself and do not require additional energy input. Examples include the aforementioned diffusive transport [19], and phenomena such as osmosis [22] and capillary action [23]. In contrast, active transport mechanisms make use of additional energy to drive transport, and includes techniques such as electrokinetics [24] and thermocapillary convection [25]. Here, I will highlight two mechanisms: capillary action and electrokinetics.

Capillary action, also known as capillarity, is a the phenomenon observed when fluid naturally moves through narrow tubes or spaces, without an external driving force [23]. This behavior results from the interplay of two forces: surface tension and adhesion. Surface tension arises at the interface between the fluid itself and the surrounding gas. The molecules within the fluid experience uniform cohesive forces. However, molecules at the surface of the liquid-gas interface experience imbalanced cohesive forces. This creates internal pressures that, when competing again adhesive forces between the fluid and solid surroundings, creates a net force for movement [14, 15]. Capillary effects are a common way to move fluids in microfluidic systems because they require no external inputs, making them ideal for at-home use in assays like at-home pregnancy or COVID-19 antigen tests [3, 26, 27]. Benefits in research are of similar nature: capillary effects allow engineers to "pre-program" the movement of fluid in a device without the need for peripheral equipment.

In contrast to passive transport mechanism such as capillary action, active mechanisms such as electrokinetics use voltage to manipulate fluid flow. Electrokinetics is an umbrella term specifically referring to the manipulation of ionic fluids or solid surfaces through their interaction with an electric field [24]. Two main transport phenomena under electrokinetics are electroosmosis and electrophoresis. Electroosmosis is the movement of an electrolytic fluid by an electric potential. When an electrolytic fluid interacts with a solid surface, a thin charged layer known as the electric double layer (EDL) is formed. The EDL is the result of a natural redistribution of charged ions, creating a specific surface charge at the liquid-solid boundary [28]. However, the overall system maintains charge neutrality. In microfluidics, the thickness of the EDL (known as the Debye length) is on the same order of magnitude as the fluidic channel, resulting in electroosmotic flow that would otherwise be negligible in larger channels. Likewise, electrophoresis is the movement of charged particles within a stationary liquid. In this case, surface charges on the particle are manipulated by an induced

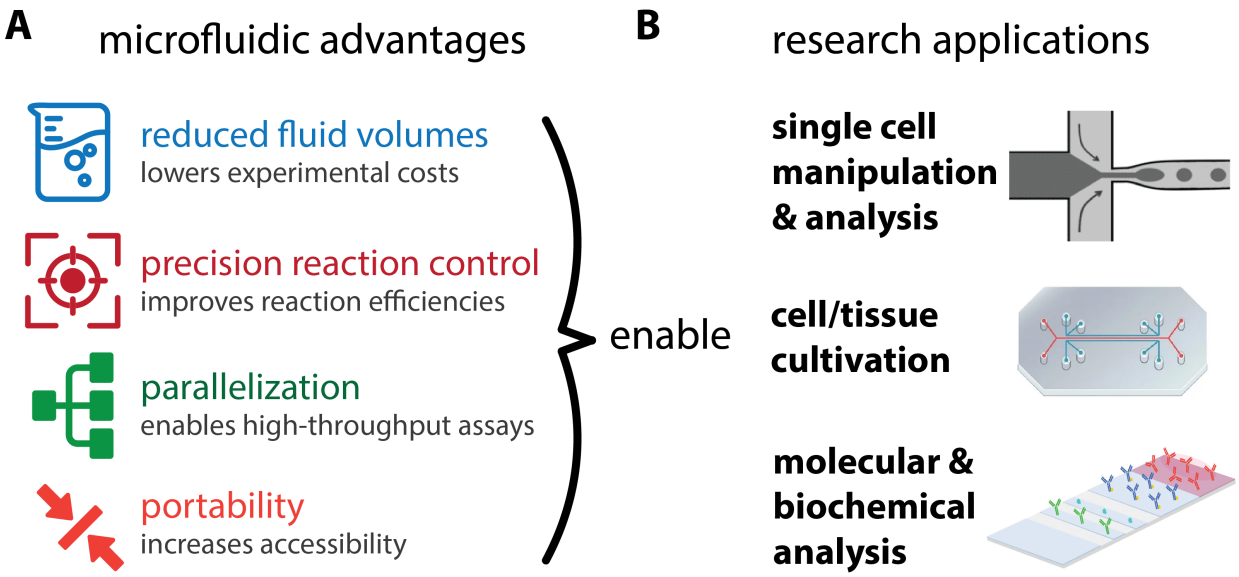


Figure 2.4: Microfluidic Advantages and Applications. Microfluidics enable a multitude of applications in biomedical research. From low reagent usage to massive parallelization, the advantages of microfluidic systems have fueled countless biomedical research innovations, including high-throughput single cell analysis and "organ-on-a-chip" technology. The applications highlighted here represent only a fraction of the developments made by the broader microfluidics community [33, 34].

electric field, allowing the particles to be moved accordingly [29]. Both transport phenomena have been widely employed in microfluidics to perform chemical separations [30], manipulate biological species [31], or for electronic flow control schemes [32].

In this summary of the physical principles behind microfluidic flow, I selected three specific properties to review: laminar behavior, diffusion, and unique microscale transport mechanism, mainly capillary action and electrokinetics. These properties form the foundation of microfluidic behavior and offer a quick glimpse at the fascinating transport phenomena present in fluids at the microscale.

2.1.2 Advantages and Disadvantages

Microfluidic systems can offer unique advantages and disadvantages when compared to traditional bench-top assays [35]. The most evident advantage is low sample and reagent volumes. Miniaturizing experiments onto microfluidic devices results in significantly reduced operating volumes. This directly translates into experimental cost savings: assays that use precious samples or expensive reagents can be executed more affordably [36]. Another distinct advantage of microfluidic devices is with throughput, scalability and automation. Devices can be designed to process samples in a high-throughput manner, without direct user interven-

tion, resulting in systems that can collect data at faster rates [37–39]. This also allows for more precise and efficient reactions, limiting user error and user fatigue [40]. Scalability also benefits fabrication, before experiments are even run. Microfluidic devices are often fabricated in batches, using economies of scale to reduce the per-device cost [41]. This again improves the affordability of microfluidic experiments. Section 3.3 will further detail the microfluidic fabrication process. Finally, microfluidic devices operate at the same scale as many biological species of interest, from cells to proteins. By replicating the physiologically relevant dimensions of biology, microfludics can uniquely perform assays that would be more challenging in macro-scale environments, such as single-cell experiments [5, 42–44].

A few indirect benefits also contribute to the appeal of microfluidic systems. The smaller footprint of microfluidic systems increases portability [45]. This enables more flexible functionality for various operating conditions, including in resource-limited environments [46]. Furthermore, microfluidic systems often allow for versatile design schemes: microvalves, micropumps, electrodes, and optics can be integrated directly into the device, satisfying a wide range of experimental needs [37, 47–50]. Microfluidic compatibility with optics and imaging has been of particular importance, enabling experimental designs that can, for example, sort cells [51] or analyze proteins [52]. Likewise, the unique mass transport phenomena described throughout Section 2.1.1 can also be exploited, resulting in emergent approaches such as inertial microfluidics [53, 54].

However, there remains some disadvantages to the use of microfluidics systems. The main limitation is the high barrier-to-entry for microfluidic incorporation [55]. The advent of microfluidic systems promised to miniaturize experiments, hence the term"lab-on-a-chip". Nonetheless, the reality is that microfluidic systems are reliant on lab-scale external hardware, such as vacuum pumps, microscopes, and pressure controllers. The moniker "lab-on-a-chip" is often ironically rephrased as "chip-in-a-lab" [56, 57]. This high barrier-to-entry limits the accessibility of microfluidic technology, often relinquishing it as a niche technique for biologists and engineers willing to make the necessary time and knowledge investment. Simultaneously, the tailored designs of many microfluidic systems, in addition to their operational complexity, further limits broader accessibility outside of specialist laboratories [58]. Despite some drawbacks, microfluidic systems remain an unique and versatile experimental technique [59]. From reduced volumes to diverse compatibility, they enable modern biomedical research at the micro-scale **(Figure 2.4A)**.

2.1.3 Modern Applications in Biomedical Research

A wide range of microfluidic systems have been developed by the research community over the past three decades. While this dissertation focuses on using microfluidics for single-cell biophysical phenotyping, I highlight a few different ways **(Figure 2.4B)** microfluidics have been employed.

The rise in microfluidic chips for single-cell analysis parallels the increased accessibility of DNA sequencing and related technologies such as single-cell RNA sequencing. Microfluidic systems are ideal for manipulating, isolating, and measuring single-cells, enabling new advances in cellular biology. A popular approach for doing so is with droplet microfluidics [8, 60–62]. Droplet microfluidics involves the encapsulation of cells and reagents into a droplet that is in an immiscible carrier fluid, typically an oil-water emulsion. The process can be encapsulate hundreds of cells per second, making it a highly viable technique for high-throughput single-cell analysis [39, 51, 63–65]. In just one example, droplet microfluidics were used to screen over 40,000 cells to identify transcriptionally distinct cells [66]. This dataset helped create a molecular atlas of gene expression, with the goal of identifying cell classes and novel candidate cell subtypes in mouse retinal cells.

Cell and tissue cultivation on microfluidic devices have been envisioned as an alternative to in vivo testing [10, 67–70]. Sometimes referred to as "organ-on-a-chip", these devices typically involve the growth of cells within microfluidic chambers that are continuously perfused with nutrients by adjacent channels. The goal of the technology is to investigate organ physiology and disease etiology, and facilitate drug discovery and development. In one study, microfluidic devices, each with active cell cultures from a single tissue type, were interconnected to form a model of a multi-organ microphysiological system [71]. Likewise, other systems have focused on single organ recapitulation or disease modeling [72–75].

Finally, microfluidic systems have also been employed for various molecular and biochemical analysis. One such example is with lateral flow assays, briefly discussed at the beginning of this section (Section 2.1). Lateral flow assays broadly fall into a category known as "paper-based microfluidics" [76–78], which rely on capillary action to drive fluid flow. Applications of paper-based microfluidics range from enzyme-linked immunosorbent assays (ELISA) [79, 80] to genetic tests for malaria [81]. Beyond paper microfluidics, alternative detection mechanisms, such as advanced imaging [82–85] or electrophoresis [29, 86–88], have also been used for microfluidic molecular analysis. These techniques all utilize microfluidic advantages such as lower volumes and improved reaction efficiencies in order to optimize experimental parameters, improve sample recovery, and gain measurement sensitivity.

2.2 Single-Cell and Multimodal Analysis

Single-cell analysis refers to the approach in which each individual cell is examined and studied. This stands in contrast to conventional approaches, in which bulk tissue-level samples are examined collectively, with the assumption that the cells in a particular tissue type are morphologically and genetically identical. Over the past decade, this assumption has been repeatedly eroded [89, 90]. It is now widely understood that, even within tissue and cell types, broad heterogeneity exists [91–95]. Each cell is regarded as a unique entity, working in concert with neighboring cells and reacting to the surrounding environment to coordinate population level responses.

The significance of single-cell approaches is evident when examining Xenopus oocytes maturation. Ferrell and Machleder observed that immature Xenopus oocytes exhibit interesting behavior when exposed to progesterone [96]. Progesterone is a critical hormone for oocyte maturation, inducing a cascade of events that lead to final cell arrest in the metaphase of meiosis. More specifically, progesterone induces the phosphorylation and activation of p42 MAPK, a key mediator that signals another cell division protein, Cdk2, to complete the final maturation of the oocyte [97]. Data from ensemble averages of oocytes responses suggested that a continuous input of progesterone would correlate with a continuous signaling output; i.e. more progesterone would result in more photphorylation of p42 MAPK, and thus more stimulus to Cdk2, and so forth. This would imply that, on average, oocytes respond proportionally to the level of progesterone stimulation. For example, an intermediate level of stimulation would result in an intermediate commitment to maturation. However, examining individual oocytes showed that rather than exhibiting a graded response, oocytes displayed an all-or-nothing commitment. In other words, the population of stimulated oocytes comprised of two distinct subpopulations: committed and noncommitted; there were no oocytes at intermediate levels of commitment. This phenomenon challenged the notion of a smooth, continuous transition and underscored the importance of understanding mechanisms at the single-cell level. While bulk averages predicted a graded response, single-cell analysis revealed a unique binary response. Biological tools and approaches must consider single cells to accurately capture underlying processes.

In similar studies, researchers used single-cell approaches to reveal new insights on cell behavior. Loo et. al. examined cell heterogenity during the adipogenesis of 3T3-L1 preadipocytes [98]. To track the progress of differentiation, bulk readouts of adiponectin hormone production and of lipid droplet expression was used. As the readouts of these parameters moved from low to high, it was expected that the average cell also progressed from an undifferentiated to differentiated internal state. However, Loo et. al. found a dynamic mixture of subpopulations instead, in which only a small subset of cells underwent full adipogenesis. Likewise, in a more direct approach, Shalek et. al. used single-cell RNA sequencing to examine heterogeneity in mouse bone-marrow-derived dendritic cells (BMDCs) response to lipopolysaccharide (LPS) [99]. LPS are large molecules commonly found on the outermost membrane of Gram-negative bacteria, and have important implications in immunology [100]. Unsurprisingly, the researchers uncovered broad single-cell heterogeneity, with many key immune genes bimodally expressed. These studies highlight the power of single-cell approaches. It allows researchers to uncover hidden diversity among cells and reach more accurate conclusions about cellular states and behaviour **(Figure 2.5)**.

Multimodal analysis refers to approaches that combine multiple measurements on a single target, in this case, a single cell. Taking multimodal measurements enables deeper conclusions versus that if the measurements were taken separately. The leading archetype of this approach is in multiomic measurements. Multiomics is a multimodal research approach in which multiple "omic" measurements are combined, such as genomics, epigenomics, tran-

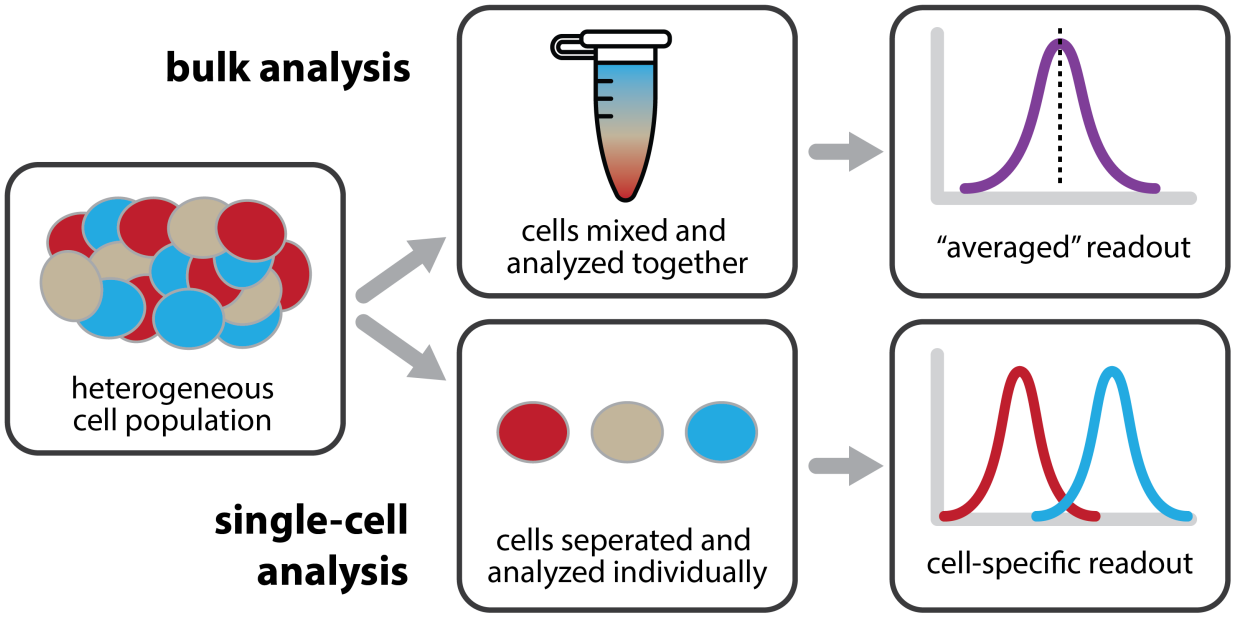


Figure 2.5: Bulk Versus Single-Cell Analysis. When analyzing a heterogeneous population of cells, a bulk analysis (top row) consists of taking measurements on the population as a whole. This results in "averaged" data (purple curve) that does not reflect the underlying heterogeneity. Meanwhile, a single-cell approach (bottom row) isolates each cell in the population, and takes individual measurements on every cell. This results in "single-cell" data (red and blue curve) that can discern subpopulation differences.

scriptomics, proteomics and metabolomics [101]. An early implementation of this approach was by Sey et. al. in a technique called DR-seq (gDNA-mRNA sequencing). In this work, the researchers examined a fundamental aspect of biology: the distinction between genotype, encoded by DNA, and phenotype, encoded by RNA. The overarching question aimed to understand how sequence variation affected phenotypic traits. With paired genomic and transcriptomic data, the authors showed that copy number variations played a critical role in the variability of gene expression among individual cells. Genes with high transcriptomic expression variablity generally had lower genomic copy numbers. In another example of multimodal measurements, researchers combined imaging and sequencing technologies to explore protein-DNA interactions in the nuclear lamina [102]. Specifically, they examined interactions between the Lamin-B1 protein and lamina-associated domains (LADs) in transfected HEK293 human embryonic kidney cells. Using a microfluidic chip, viable cells were identified, sorted and imaged prior to sequencing. A tracer protein conjugated to green fluorescent protein (GFP) enabled the visualization of the lamina associated domains within the nucleus. The imaged data of each cell was then paired with downstream sequencing data, resulting in a unique joint analysis of morphological and genetic data. One correlation identified was that cells with larger nuclei yielded more unique fragments sequenced; another showed that greater fluorescent expression correlated with higher coverage in less lamina-

associated regions of the genome. Overall, the researchers showed that their approach can be used to identify and sort cells based on visual phenotypes that correlate with sequencing measurements.

Single-cell and multi-modal measurements are powerful approaches for understanding the complex biology of cells. In chapters 4 and 5, I will describe our approach to single cell multimodal measurements using Multi-Zone Visco-NPS and Combo-NPS. These platforms capture multiple biophysical properties for each single cell, enabling novel analytical approaches.

2.3 Biophysical Phenotyping

Biological systems are often characterized through the lens of molecular biology and biochemistry. However, cells and tissue are physical entities as much as they are chemical. Interpreting cells as physical dynamic, living, materials gives rise to approaches typically reserved for engineering disciplines, such as the exploration of material rheology. The investigation of living systems, in particularly single cells, from the perspective of biophysics enables a new paradigm in biomedical research that bridges the interface of biology, physics, material science, and engineering. For this dissertation, biophysical phenotyping is co-opted to include examining surface marker expression, among other mechanical properties such as: morphology, elasticity, and viscosity.

2.3.1 Significance of Biomechanics and Mechanobiology

When examining the biophysical mechanics of a cell, there are two canonical fields of study: biomechanics and mechanobiology [103]. Biomechanics is the study of the physical mechanical properties of a cell or tissue. It explicitly examines the quantitative mechanical behavior of a biological sample of interest, characterizing. For example, Alhalhooly et. al. examined how the biomechanics of multiple cell types (brain, breast, prostate, and pancreatic cancer cells) change in response to standard chemotherapeutic drugs [104]. Alternatively, mechanobiology is the study of how mechanical forces affect biological systems. This includes investigating the molecular pathways cells utilize to sense and respond to external physical stimuli. For example, Argentati et. al. reviewed the underlying pathways in which stem cells respond to mechanical force, highlighting the intricate interplay between the ECM, focal adhesion complexes, cytoskeleton and nucleskeleton proteins for both mechanosensing and mechanotransduction [105].

The work presented in this dissertation is largely focused on development of tools that enable the measurement of cellular biomechanics, rather than the underlying mechanobiology that give rise to the distinct cellular biomechanics. Nonetheless, the two areas of study are highly interlinked. Understanding the underlying mechanobiology enables greater understanding of the fundamental reasons behind distinct biomechanical attributes. Likewise,

measuring differences in biomechanical attributes contributes and motivates further studies of mechanobiology phenomenon. In a more explicit example of the relation between biomechanics and mechanobiology, we can look at research of cancerous tissue. Quantitative biomechanics have shown that cancer cells are softer than their non-malignant counterparts [106–108]. The exact reason behind this remains an open area of research. Nonetheless, our understanding of cellular mechanobiology helps rationalize this phenomenon: cell undergo numerous changes during their path towards malignancy, including changes in cytoskeletal organization and nuclear morphology [109–112]. These various changes contribute to the mechanical transformation of a healthy cell from stiff to more compliant. Ultimately, while the work presented here is largely focused on biomechanical tools, it remains worthy of maintaining both a biomechanics and mechanobiology perspective.

Cellular biomechanics and mechanobiology are important because they reflect cell function [113], fate [114], and disease [109]. From the perspective of cancer development and progression, it is well known that biomechanical transformations of the affected tissue transpire in parallel with traditional hallmarks of cancer, such as oncogene activation and angiogenesis [109]. Thus, investigating cancer from a biophysical perspective can provide valuable quantitative information that enhances our understanding of this multifaceted and highly complex disease. Measurements on the intrinsic biophysical properties of cells could compliment conventional molecular and genetic analyses, revealing more about each individual cell.

2.3.2 Conventional Tools for Biophysical Phenotyping

The gold-standard for single-cell biophysical phenotyping is to use atomic force microscopy (AFM). AFM is a well-established, commercially-available tool that uses a cantilevered beam and a micro-fabricated tip to spatially probe the mechanics of a cell. The tip itself can be as small as a few nanometers, enabling a high-resolution, localized measurement of the cell surface. Since the first introduction of AFM in 1989, its use in research has grow exponentially, and is now one of the most popular and widely accepted tools used to study cellular mechanics [115]. In one study, Rother et. al used AFM to measure and compare the viscoelastic properties of malignant and benign cell lines [116]. Using a pyramidal cantilever-tip geometry oscillating at a frequeny between 1 to 100 Hz, the authors measured up to 10 cells under constant force. Localized force map "images" of the cells revealed that, in general, adherent cells exhibited higher stiffness at their periphery, a result attributed to the presence of a stiff actomyosin cytoskeletal ring common in cell peripheries. Furthermore, the authors found that the viscoelastic properties were distinct amongst the cells tested, where benign cell types, such as MCF-10 breast epithelial cells and NIH/3T3 fibroblast cells, were stiffer than malignant cell types, such as MDA-MB-231 invasive breast epithelial cells and SW13 malignant adrenal gland epithelial cells.

Other conventional techniques include micropipette aspiration [117, 118], microbead rheom-

etry [119, 120], and optical stretchers [121–123]. Micropipette aspiration utilizes negative pressure to deform partially a cell through a micropipette cavity. The deformation geometry is then analyzed in order to calculate mechanical properties such as the elastic (Young's) modulus. Next, microbead rheometry typically uses microbeads attached to the cell surface. The microbeads are magnetically perturbed, generating forces on the cell that can then be measured. Finally, optical stretchers use a double-beam trap in which two opposed, slightly divergent, and identical laser beams with a Gaussian intensity profile trap a cell at the center of a fluidic channel. This occurs because the light itself carries momentum. Thus, when the ray of light is reflected or refracted at an interface between the cell and the surrounding media, it is forced to change direction and velocity, resulting in a change of momentum. Because momentum is conserved, some of the light's momentum is transferred to the interface, ultimately exerting a force on the cell's surface. By applying piconewtons of force on a cell and examining the cell's deformation geometry, optical stretchers can also characterize a cell's biomechanical properties.

Conventional techniques, such as those described above, have one major limitation: sample throughput. Throughput refers to the number of cells that can be measured within a specified time-frame, and is a critical factor when conducting single-cell measurements. As emphasized in the Section 2.2, one of the main advantages of single-cell analysis is the capability to uncover underlying heterogeneity. The practical implementation of this advantage requires a sufficient sample size such that statistically significant inferences can be made. In the case of AFM and optical stretchers, the throughput remains far below 1 cell per second [115]. Traditional AFM can take up to 10 minutes just to measure one single cell; though recent improvements have significantly increased AFM speed [124]. Nonetheless, low throughputs continue to hinder conventional techniques from wider research applications and clinical adoption [125].

Another remaining issue with conventional techniques is the significant variance when measuring single cell mechanical properties. Each technique has its own unique set of operating procedures. Coupled with the diversity of analysis approaches, and it is no surprise that published results on the same sample types can vary broadly. In one study [126], the authors found up to a 1000 fold difference in the elastic modulus of breast epithelial cells when comparing measurements between AFM, optical stretchers, and microbead-based techniques.

The answer to these limitations lies with microfluidics. Microfluidics offers the capability of measuring cells at greater throughputs, all while automating much of the technique itself, improving reproducibility. The advantages of microfluidics, detailed in Section 2.1.2, remain a natural asset for measuring single-cell mechanics. The following section will describe modern microfluidic approaches toward single-cell biophysical phenotyping, and how they improve upon existing conventional techniques.

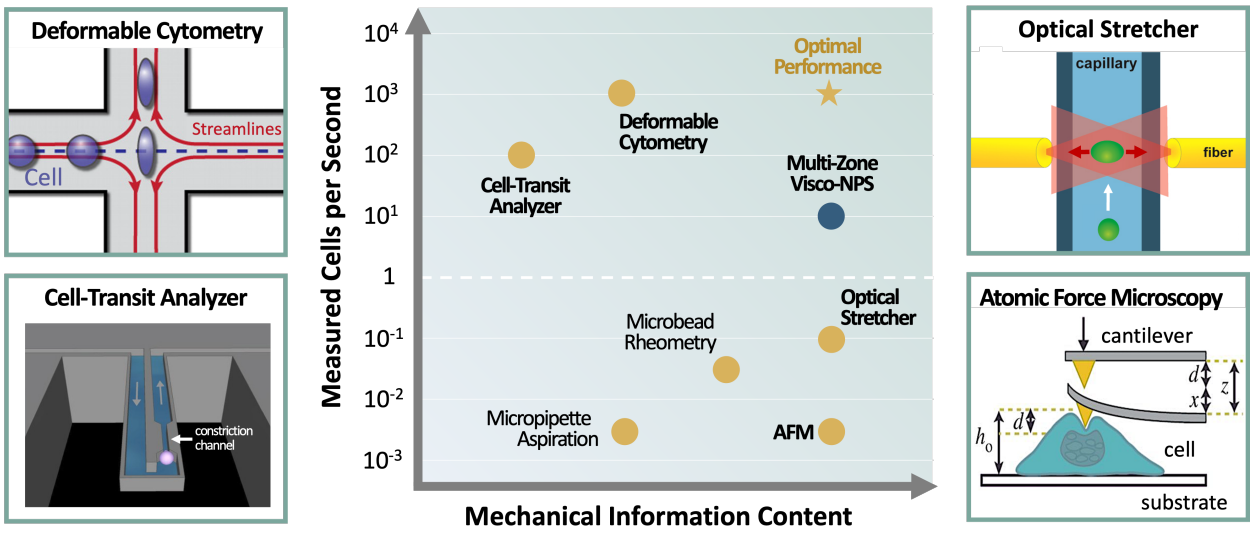


Figure 2.6: Comparison of Single-Cell Mechanical Phenotyping Techniques. Throughput (number of cells measured per second) versus mechanical information content (number of biophysical parameters captured) are compared for various single-cell mechanical phenotyping techniques. Highlighted here are four different techniques: deformability cytometry images cell shape under hydrodynamic stresses; cell-transit analyzers examine passage time through narrow constriction channels; optical stretchers use light to apply piconewtons of force on cells; AFM uses a cantilever probe to both apply force and record response. This figure is adapted from [115, 127–131].

2.3.3 Modern Microfluidic Approaches for Single-Cell Biophysical Phenotyping

Microfluidic approaches toward single-cell biophysical phenotyping increase sample throughput using a variety of techniques **(Figure 2.6)**. A common approach is to incorporate narrow constriction channels that efficiently strain cells in a moderate to high throughput manner [132, 133]. Inlet pressure forces cells to file through the constriction, deforming each passing cell in the process. Parameters such as cell morphology or transit time can then be assessed to determine mechanical properties, such as deformability. Readout of cellular physical properties can be done via cantilever resonance **(Figure 2.6)** [129] or from morphological imaging [134]. The approaches in this dissertation implement a form of narrow constriction channels, utilizing ohmic resistance as a label-free readout of cellular attributes. Chapter 3 further details this specific approach. Beyond physical constrictions by the channel walls, strain can also be applied using hydrodynamic fluid forces. In deformable cytometry (DC) **(Figure 2.6)** [128] and real-time deformable cytometry (rt-DC) [135], cells are perturbed at up to 1000 cells/s, vastly outperforming alternative mechanical phenotyping platforms. For example, Ahmmed et. al. introduced "Multi-sample deformability cytometry" (MS-DC) in which they incorporated multiple hydrodynamic deformation channels to measure a reservoir of

breast and prostate cancer cells [136]. In this approach, the authors tested up to 9 cell types at a throughput of 100 cells per second, showing the canonical result that malignant cell are indeed more deformable than non-malignant cells. The trade-off is that theses platforms can only record elementary parameters, often relying on high-speed cameras to capture the morphology of the cells during deformation. Additional physical properties, including elasticity and viscosity, are only be inferred from elementary deformability ratios. Novel approaches have been developed to address these limitations, incorporating quantitative modeling to further ascertain biophysical properties [137, 138]. New microfluidic approaches continued to be developed, enabling advanced mechanical phenotyping of single-cells with capabilities beyond conventional approaches.

2.3.4 Research and Clinical Applications Of Single-Cell Biophysical Phenotyping

Cellular biomechanics bridges the gap between physics, biology, and medicine, offering exciting avenues for understanding health and disease at the cellular scale. The study of cellular biomechanics and biophysical properties has broad research and clinical applications. Here, I highlight a few notable examples.

The archetypal example of the relevance of cellular biomechanics is to exploring the underlying cytoskeleton. The cytoskeleton is a dynamic and intricate network of interlinked protein filaments that extends from the cell nucleus to the cell membrane. It consists of three main components (actin filaments, microtubules, intermediate filaments) that support a multitude of functions, from maintaining the cell's shape and mechanical stability to serving as an internal transport highway for proteins, molecules, and other cargo [139]. Cells are constantly under internal and external forces, resulting in changes that act throughout the cytoskeleton, ultimately affecting local mechanical properties and cellular state [140–142]. How physical forces are transduced by the dynamic cytoskeleton and the responses cells form contribute to a broader understanding of cellular behavior. Studying single-cell biomechanics is just one avenue towards a more comprehensive understanding of the cytoskeleton.

Cellular biomechanics have also been useful in understanding infection, such as how Plasmodium parasites, the causative agents of malaria, attack human red blood cells (RBCs). Among other findings, Introini et. al. review critical aspects of cellular biophysical properties before and after a malaria infection [143]. They note that the complex phases of infection alter the biophysical properties of RBCs in a multitude of ways, with the conclusion that parasite-infected RBC have increased physical rigidity. This exploration of biophysical properties has contributed to a greater understanding of how malaria affects RBC mechanics during invasion, with promise for better diagnostic and treatment opportunities.

Similarly, researchers have explored the link between cellular biomechanics and metabolism. As mentioned previously, external forces can induce changes in cell state, including internal

metabolic changes. Multiple signalling pathways involved in cellular metabolism have been shown to be tied to cellular mechanosensing. One example is the RhoA GTPase pathway, which connects surface integrins and cadherins to cytoskeletal proteins in order to accelerate glucose metabolism [144]. A better understanding of the cross-talk between metabolic processes and cellular biomechanics contribute to diagnostic and therapeutic opportunities for metabolic disorders.

Finally, cellular biomechanics have been broadly regarded as an avenue to better understand the development and treatment of cancer. Physical changes in the cellular biomechanics are well documented during a transition towards tumor malignancy [106, 110]. This includes cytoskeletal remodeling due to increased solid and fluid stresses, new activated mechanosignaling pathways, and changing microarchitecture from altered growth patterns and increased extracellular matrix deposition [109, 112, 145–147]. Consequently, measuring and investigating the biomechanical changes before and after malignant transformation could be a critical component in developing new approaches toward cancer treatment. The work further presented in Chapters 4 and 5 detail my approaches on using novel microfluidic platforms to investigate and compare non-malignant and malignant immortalized cells, and to explore characteristics of primary cells with varying degree of breast cancer risk.

Beyond applications in research, novel clinical applications have also been demonstrated to take advantage of single-cell biophysical phenotyping. Advancements in measurement throughput made possible by microfluidic systems (described in the previous subsection) have made clinical adoption of biophysical phenotyping a near-term possibility [115].

In one study, Tse et. al. used mechanical phenotyping to analyze and identify malignant cells in pleural effusions [148]. Pleural effusions are unwanted fluid accumulation outside of the lungs; while the direct pathology is unknown, they can occur during infection or kidney failure [149]. The makeup of the pleural effusions can sometimes disseminate tumor cells, which can be hard to identify, complicating a clear prognosis. Moreover, conclusive diagnosis of pleural effusions is vital for patient outcomes, as the presence of malignant tumor cells often suggests a late-stage disease that requires aggressive treatment. The researchers measured the deformability of 119 patient samples, and classified the cells against known clinical outcomes: negative for malignant cells(NMC), acute inflammation (AI), chronic/mixed inflammation (CMI), atypical cells (ACs), and malignant pleural effusions (MPEs). They found that samples containing MPEs, validated by professional cytological analysis, had unique physical traits: typically larger in diameter and more deformable. Using these cellular biomechanical characteristics, the researchers successfully classify MPEs in patient samples, with a test area under the curve (AUC) of 0.86. This early work demonstrated how physical biomarkers could be useful in the clinic. The approach has potential to be implemented in a clinical workflow as a prescreening tool, reducing cytopathologist work loads.

In a similar study, Remmerbach et. al. used mechanical phenotyping to screen suspicious lesions in the oral cavity for squamous cell carcinomas. They found that malignant cells were

more deformable than their healthy counterparts, and confirmed such findings with standard histology. This is again another clear demonstration of the potential impact of single-cell biophysical phenotyping in the clinic, enabling more rapid, quantitative diagnostic readouts in a label-free manner. Beyond tumor diagnostics, mechanical phenotyping have been shown to assist in classifying drug effectiveness [150]. For example, Li et. al. examined the use of all-trans retinoic acid (ATRA) in treating acute promyelocytic leukemia (APL) [151]. In APL, the standard of care is to quickly administer ATRA; however, a proportion of patients remain resistant to the drug. The rapid identification of resistant patients is critical for positive care outcomes, as such patients require alternative interventions. Among other results, Li et. al. showed that ATRA resistant cells are much stiffer than ATRA-sensitive counterpart, opening a promising avenue in using cell mechanics to screen for drug resistance.

In summary, single-cell mechanical properties play a pivotal role in both research and clinical contexts. These properties serve as valuable indicators, shedding light on various aspects of cell state behavior, from the cytoskeleton to metabolic processes and even malignancy. From a clinical standpoint, understanding these mechanical attributes provides novel insights into disease progression and drug resistance. Overall, a multitude of research and clinical applications have been shown to utilize or incorporate single-cell mechanical properties, with growing interest and studies in the field constantly expanding.

2.4 Conclusion

I present the motivation, technical foundation, and relevant background related to my dissertation work on microfluidic devices for multimodal, single-cell biophysical phenotyping. In three comprehensive sections, I introduce and thoroughly review microfluidics, explain the significance behind multimodal single-cell analysis, and detail the motivation and applications of biophysical phenotyping in modern biomedical research. Ultimately, this chapter provides the essential foundation needed for detailed understanding of the microfluidic systems described in Chapters 4 and 5. In the following chapter, I delve further into the primary methodologies employed and detail specific design and fabrication processes.

Chapter 3

Methods: Node-Pore Sensing

This chapter is partially adapted from a previously published paper:
A. Lai, R. Rex, K. L. Cotner, A. Dong, M. Lustig, L. L. Sohn, "Mechano-Node-Pore Sensing: A Rapid, Label-Free Platform for Multi-Parameter Single-Cell Viscoelastic Measurements." J. Vis. Exp. (190), e64665, doi:10.3791/64665 (2022).

This chapter will describe my approach towards single-cell biophysical phenotyping using Node-Pore Sensing (NPS). I will start by reviewing the broader field of microfluidic resistive pulse sensing (RPS), and transition into the theory and operation of NPS. Likewise, I will describe prior work that utilized NPS, specifically two platforms named mechano-NPS and visco-NPS. Finally, I will describe the practical implementations of NPS, from device fabrication, to hardware design and software analysis. The approaches and processes described in this chapter form the fundamental methodologies utilized in Chapters 4 and 5.

3.1 Resistive Pulse Sensing (RPS)

In a standard resistive pulse sensing (RPS) configuration, the electrical resistance across a narrow fluidic channel is measured as particles traverse through [152–157]. Distinct resistive pulses are created as the non-conductive particles partially block the electric field lines. Node-Pore Sensing (NPS) [1, 132, 151, 158, 159], further discussed in Section 3.2, is a variation of resistive pulse sensing (RPS), in which signal-to-noise ratio is improved by modulating the narrow fluidic channel with a series of nodes and pores. The modulation in geometry produces unique resistive pulse signatures that help overcome low SNR [1].

An advantage of RPS (and impedance cytometry) techniques is the ability to perform label-free measurements. Because RPS relies on the partial blocking of electric fields caused by insulating particles, single-cells can be measured without the need for any exogenous labeling. Conventional methods for single-cell characterization typically use fluorescent or magnetic

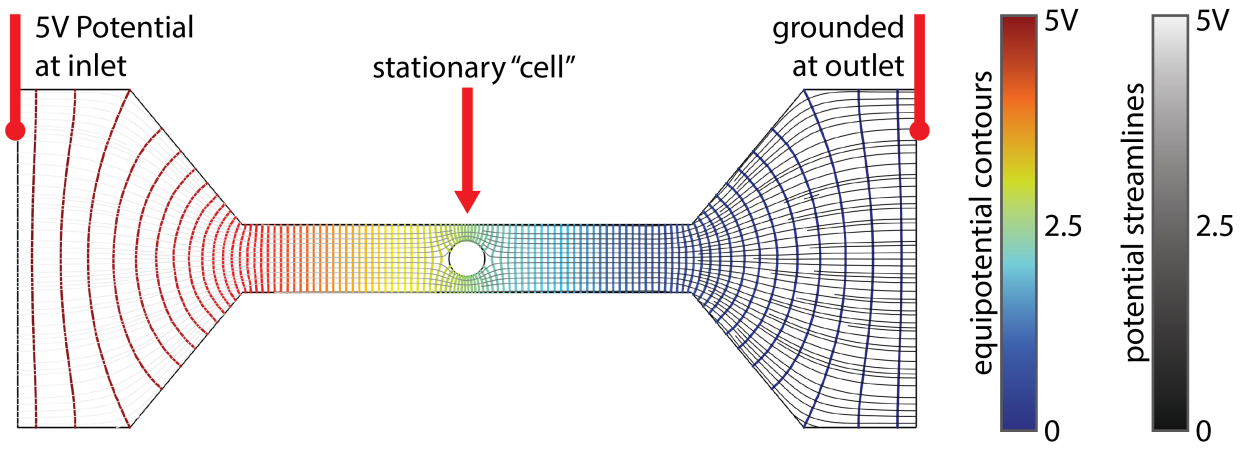


Figure 3.1: Computational Simulation of Electric Field Across A Narrow Pore. RPS is a technique that measures the changes in electrical resistance across a narrow pore. Shown here is a computational simulation performed in COMSOL Multiphysics® [17] of how the electric field lines change across a narrow pore. The pore is filled with a conductive electrolyte, with a stationary circular geometry at the center, representing the presence of an insulative particle such as a cell. A potential of 5 V is applied from left to right, as illustrated by the equipotential lines. Note how the electric field density increases around the circular geometry, representing an overall increase in the resistance measured across the pore.

labels. The biochemical alterations from the labeling process can potentially influence the state of the cell, introducing a confounding factor that results in a non-ideal measurement [160]. Furthermore, the use or exogenous labels requires previous understanding of the property being targeted–there must be existing work such that a probe of adequate specificity can be used. Finally, label-based methodologies require additional preparation time, increasing cost and reducing clinical accessibility [161]. Ultimately, label-free measurements such as RPS negate these aforementioned drawbacks and improve data quality while maintaining measurement accessibility.

3.1.1 Background and Theory

Resistive pulse sensing (RPS) is a technique based on the Coulter principle, which states that particles traversing an aperture with an applied electric current will produce a change in impedance proportional to the volume of the particle [152, 157, 162]. This change in impedance is due to the partial blocking of the electric field caused by the transiting particle. In biomedical applications, Coulter counters and RPS are broadly utilized for counting and sizing cells, bacteria, and viruses [153–156, 163, 164]. For example, in clinical hematology, Coulter counters are used to obtain information about patients' blood cells, such as blood count and size distribution [165].

For the practical implementation of the Coulter principle, three criteria need to be met:

1. The particles of interest should be suspended in a conductive fluid.
2. The electric field lines should have a sufficient high current density such that the passage of the particles sufficiently block the electric field lines, resulting in detectable changes in current **(Figure 3.1)**.
3. The passing particles should be diluted such that only a single particle passes through the pore in any given moment.

Overall, any implementation of the Coulter principle must compromise between real-world limitations. For example, creating a smaller pore to satisfy requirement #2 will improve signal-to-noise ratio, but at a loss of dynamic range and device reliability. Likewise, diluting the particle suspension will help satisfy criteria #3, but will also result in reduced sample throughput. Metrics such as sensitivity, noise, throughput, and reliability must be balanced depending on the specific application requirements.

Advancing upon the Coulter principle, DeBlois and Bean derived the quantitative relation between changes in current and particle size in 1970 [152]. They found that the total change in electrical resistance across a narrow constriction is proportional to the ratio between the particle volume (V_p) and the constriction volume (V_c):

$$\Delta R = A\frac{V_p}{V_c} \tag{3.1}$$

where A is a scalar factor that depends on variables such as constriction geometry and fluid conductivity. More specifically, the mathematical relation between a change in resistance caused a particle transiting through a narrow pore, can be described by [153]:

$$\frac{\Delta R}{R} = \frac{d^3}{D_{eff}^2 L}\left[\frac{1}{1-0.8(d/D_{eff}^3)}\right] \tag{3.2}$$

where ΔR is the change in resistance from baseline, R is the baseline resistance of the conductive pore, d is the diameter of the particle, D_{eff} is the effective diameter of the pore, and L is the length of the pore. The effective diameter (D_{eff}) is an experimentally derived constant, calibrated by measuring particles of a known diameter. Equation 3.2 is used throughout Chapters 4 and 5 to calculate the diameter of transiting cells from measured changes in resistance.

3.2 Node-Pore Sensing (NPS)

Node-pore sensing builds upon the principles of RPS by incorporating a series of nodes within a narrow pore [1, 132, 151, 158, 159]. These nodes are wider than the pore itself, and are

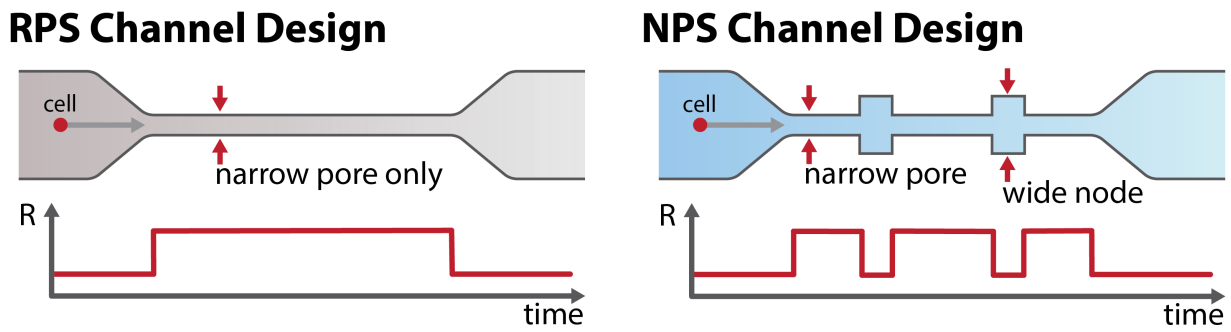


Figure 3.2: Design and Signal Differences Between RPS and NPS. Both RPS and NPS measure the electrical resistance across a narrow pore as a small particle, such as a cell, transits across. RPS consists of a simple linear pore, resulting in a rectangular pulse [152–157]. NPS incorporates nodes into a linear pore, resulting in a rectangular pulse that is periodically modulated [1, 132, 151, 158, 159].

designed to modulate the resistive pulse signal. When a cell passes from a narrow pore to a wider node, electrical resistance is allowed to momentarily return to baseline, resulting in distinctive subpulses that contribute to an overall increase in the signal-to-noise ratio (SNR) [1]. **Figure 3.2** highlights the signal pulse differences between RPS and NPS. RPS, with a single narrow pore, is useful for simple counting and sizing applications. In contrast, the addition of wider nodes in NPS divide the signal pulse, providing temporospatial information about the particle as it move through the pore.

3.2.1 Mechano-NPS and Visco-NPS

NPS was previously incorporated in two unique microfluidic devices, termed Mechano-NPS [132] and Visco-NPS [159]. Both platforms were designed to measure the mechanical properties of single-cells. The former incorporated a series of nodes and pores in conjunction with a linear contraction channel **(Figure 3.3A)**, while the latter replaced the linear contraction channel with a unique sinusoidal contraction channel **(Figure 3.3B)**. Both approaches used an identical 4-terminal measurement set-up, in which the outer electrodes applied a constant voltage, while the inner electrodes measured changes in electrical current before, during, and after cell transit events.

Using the linear contraction channel, Mechano-NPS measured cell diameter, cell deformability, and cell recovery from deformation. Deformability was quantified using a custom dimensionless index termed the whole-cell deformability index (wCDI) [132]:

$$wCDI = \frac{L_c}{U_{flow} h_{channel}} \frac{d}{\Delta T_c} \tag{3.3}$$

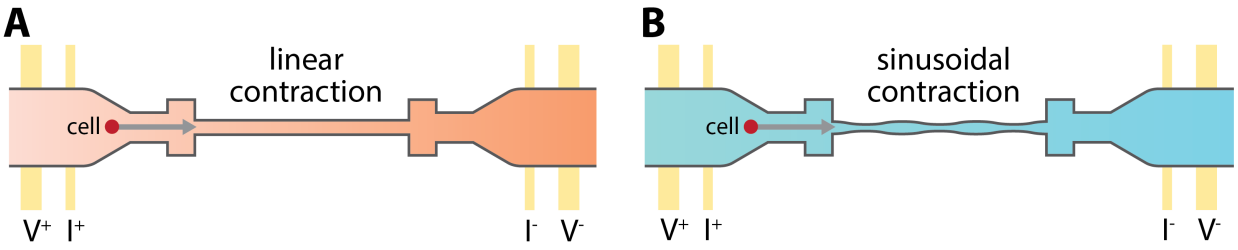


Figure 3.3: Linear Versus Sinusoidal Contraction Channels Used in Mechano-NPS [132] and Visco-NPS [159] (A) Characteristic linear contraction channel used in mechano-NPS to measure whole-cell deformability [132]. (B) Characteristic sinusoidal contraction channel used in visco-NPS to measure cellular viscoelasticity [159]. In both designs, the contraction segment was preceded by a sizing pore and node. Likewise, both approaches used a standard 4-terminal measurement to record changes in electrical current as cells were strained through the contraction. By changing the geometry that strained the cell, difference mechanical properties were measured.

where L_c is the length of the contraction segment, U_{flow} is the mean cell velocity in the pore, $h_{channel}$ is the channel height, d is the cell diameter, and ΔT_c is the duration (width) of the contraction subpulse. wCDI is a relative indicator of cell stiffness that is inversely proportional to the elastic modulus; thus, a greater value of wCDI corresponds to a softer mechanical phenotype [132]. The cell diameter (d) can be found using Equation 3.2. Finally, cell recovery was measured after the contraction channel, and was defined as the time it took for the current subpulses to return to the magnitude prior to the cell being squeezed. Kim et. al used mechano-NPS to demonstrate the malignant breast and lung cells were mechanically distinct from their non-malignant counterparts, and to differentiate between sublineages in human mammary epithelial cells (HMECs) [132].

Visco-NPS was developed as an iteration of mechano-NPS, replacing the linear contraction channel with a sinusoidal contraction channel [159]. In doing so, the cells were perturbed dynamically, enabling the modeling and readout of active viscoelastic properties. Instead of measuring a relative quantity such as wCDI, Visco-NPS could directly measure quantitative attributes of the cell, including the elastic and viscous modulus. Again, Kim et. al. used Visco-NPS to show mechanical differences between malignant and non-malignant cells, quantify perturbations to the cytoskeleton, and investigate the mechanical distinctions between cell cycle stages [159]. Chapter 4 discusses this approach in further detail and demonstrates a new microfluidic platform that expands this technology.

3.3 Microfluidic Device Fabrication

Numerous methodologies have been developed for fabricating microfluidic devices, including 3D-printing [166], etching [167], and thermoforming [168]. Here, I discuss our approach

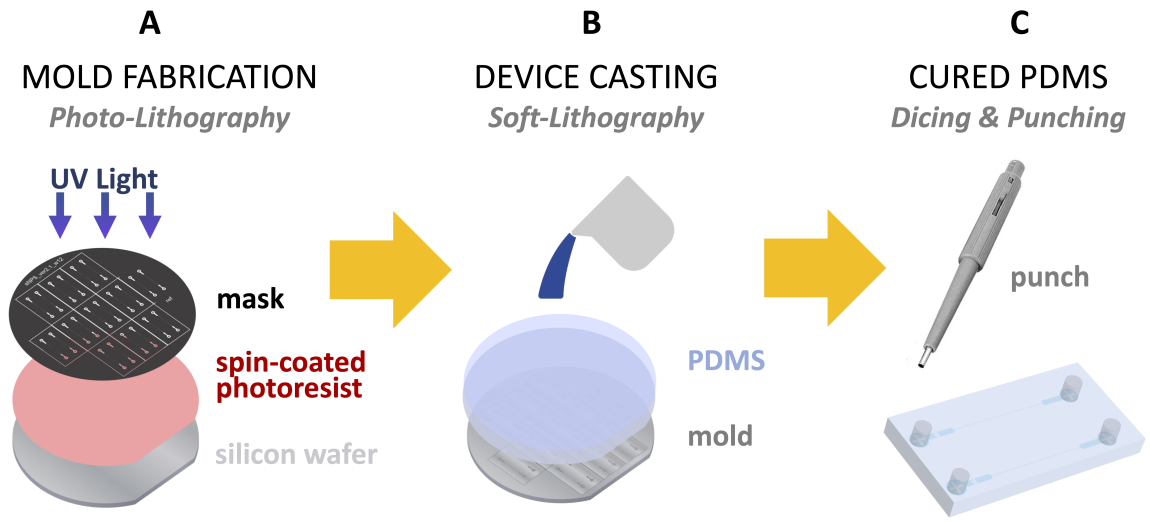


Figure 3.4: Fabrication Steps for Molding A Microfluidic Channel Molding a microfluidic channel using soft-lithography is divided into three primary steps: (A) A negative master mold is fabricated using photolithography. (B) Next, PDMS is casted onto the negative master mold. (C) Finally, the cured PDMS with the embedded microfluidic channel is excised from the master mold. Inlet and outlet access holes are created using a biopsy punch.

using soft-lithography and molded elastomeric polymers. First published in 1998 [169], soft-lithography was developed using standard photo-lithography techniques employed in the semiconductor and microelectronics industries. Photo-lithography is the process by which photoresist, a UV-light sensitive polymer, is used to create high-resolution patterns on a solid substrate, typically a silicon wafer. In soft-lithography, a master mold is created by using photo-lithography to pattern negative relief structures from a UV-light sensitive epoxy. The micro-scale negative relief structures are then used to mold a curable elastomeric polymer, transferring the exact geometric channel designs into the cured polymer. Finally, the cured polymer, with the microchannel, is bonded to another material, such as glass, to create a fully enclosed microfluidic channel. The microfluidic devices used in this work consists of channels embedded in polydimethlysiloxane (PDMS) and bonded to a glass substrate with pre-patterned electrodes. The following subsections further detail the exact processes used to create these devices.

3.3.1 Channel Fabrication

The microfluidic channel is created using soft-lithography from a master mold patterned by photo-lithography. To pattern the master mold, SU8-3025, a negative epoxy resist (Kayaku Advanced Materials), is spin coated onto a polished silicon wafer. The spin speed will dictate the resist thickness, which in turn will determine the height of the final microfluidic channel. The resist is baked on a hot plate at 95°C for 10-15 min, depending on the layer

thickness. This process evaporates excess solvent in the resist, leaving behind only the necessary photosensitive polymers. After baking, the resist is patterned by aligning the resist-coated wafer under a printed mylar mask and exposing the wafer with ultraviolet (UV) light **(Figure 3.4A)**. Because SU8-3025 is a negative resist, the areas exposed to UV light are photo-polymerized, creating permanent epoxy structures. A post-exposure bake (PEB) is performed at 65°C for 1 min, then 95°C for 5 min, to further catalyze resist polymerization. After the PEB, the wafer is submerged in SU8 developer for 5 min, washing away any unexposed resist. The wafer is rinsed with isopropyl alcohol (IPA) and deionized (DI) water. Finally, the wafer is hard baked at 150°C for 15 min to permanently set the epoxy relief structures. The completed master mold is examined under a stereo microscope and characterized using a contact profilometer.

For soft-lithography, PDMS (Sylgard 184, Dow Corning) is mixed at a 10:1 mass ratio of base polymer to initiator. PDMS is clear, compliant, and bio-compatible, making it a suitable material for microfabrication and biology-based applications. It is a two-component silicone elastomer, consisting of a base polymer and a separate crosslinking initiator. Combined with heat, the crosslinking initiator catalyzes a reaction that binds the base polymers, converting the viscous liquid into a solid, optically transparent material. After mixing at a 10:1 ratio, the PDMS is degassed in a vacuum chamber to eliminate trapped gas bubbles. The degassed PDMS is then poured over the master mold **(Figure 3.4B)** and cured in an oven at 80°C for 2 hours.

The cured PDMS is removed from the master mold, and replicate devices are diced apart. A 1 mm biopsy punch (Miltex) is used to create fluidic inlet and outlet holes **(Figure 3.4C)**. The diced and punched PDMS channels are then ready for bonding.

3.3.2 Electrode Patterning

Metal electrodes are patterned onto glass using traditional lithographic techniques and a lift-off process. First, a 1 µm thick layer of S1813, a positive photoresist, is spin-coated onto a glass slide and soft-baked at 100°C for 1 min. The resist is aligned under a mylar mask and exposed to UV **(Figure 3.4A)**. The slide is then submerged in MF-321 developer, where UV-exposed features are developed. The slide is rinsed in DI water and dried with nitrogen (N2) gas.

Patterned glass slides are place in an electron-beam evaporation chamber for thin-film metal deposition. At chamber pressures of approximately 5×10^{-6} to 5×10^{-7} torr, a thin film consisting of 75Å of titanium (Ti), 250Å of platinum (Pt) and 250Å of gold (Au) is deposited **(Figure 3.4B)**. The first, titanium layer is used as an adhesion layer between the silica glass and platinum. The second, platinum layer is used as a biocompatible layer, reducing biofouling effects during fluidic contact with cells and proteins. The third, gold layer serves as a low-resistance, soft contact pad for direct electrical connection.

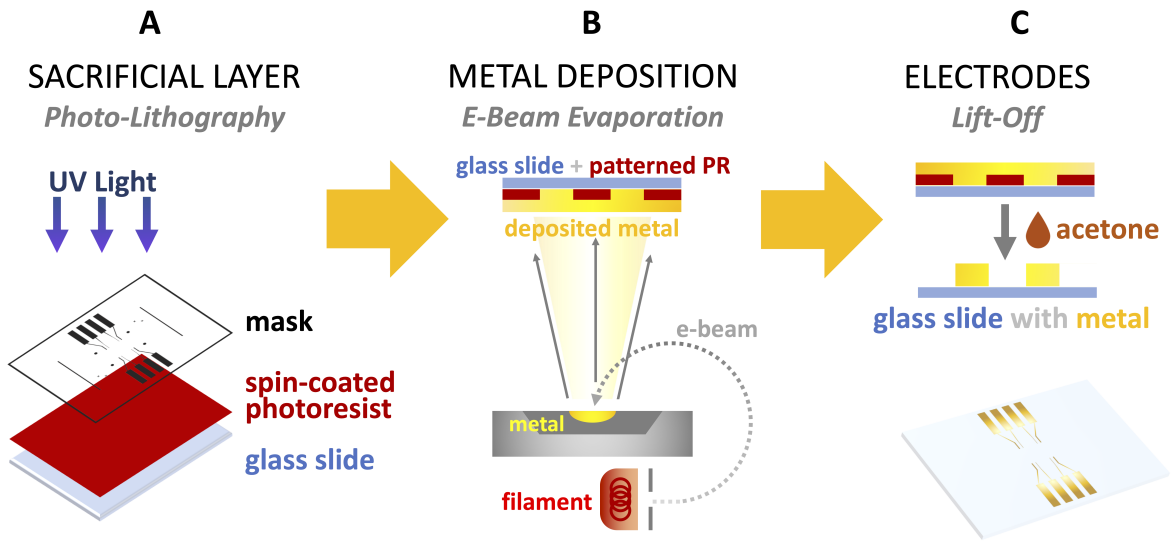


Figure 3.5: Electrode Fabrication Steps Patterned electrodes consisting of titanium (Ti), platinum (Pt), and gold (Au) are fabricated on glass substrates. (A) Positive photoresist is patterned using photolithography on a glass slide. (B) E-beam evaporation deposits a conformal layer of Ti/Pt/Au onto the patterned glass. (C) A lift-off process removes excess metal, leaving only the desired patterned electrodes.

Finally, the patterned glass substrate is submerged in a bath of acetone for 15 min. Excess metal (on top of photoresist) is lifted off, while patterned metal (in contact with the glass) remains **(Figure 3.4C)**. Gold etchant (Gold Etchant TFA, Transene) is the carefully pipetted onto electrode areas that would make direct contact with the fluidic channel, exposing the underlying platinum. The patterned glass slide with electrodes is then ready for bonding with the microfluidic channels embedded in PDMS.

3.3.3 Device Bonding

The prepared PDMS channel and electrode slide are bonded together using plasma-activated oxygen bonding. The surface properties of PDMS and glass are ideally suited for oxygen plasma, largely consisting of repeating silicon-oxygen-silicon (Si-O-Si) moieties **(Figure 3.6A)**. Plasma treatment bombards each exposed surface with high energy oxygen ion under near-vacuum conditions, "cleaning" the surface or any organic impurities and activating the surface with silanol (Si-OH) groups **(Figure 3.6B)**. Bringing the two plasma-activated surfaces (PDMS and glass) together forms a permanent silicon-oxygen-silicon (Si-O-Si) covalent bond between the two surfaces **(Figure 3.6C)**. To perform plasma-activated oxygen bonding, the PDMS channel and electrodes slide are exposed to an oxygen plasma for 2 min (100 mTorr, 30 W, Harrick Plasma). Because plasma bonding is contact based, the two treated surfaces brought together will immediately bond. This immediacy presents difficulties in aligning the bottom electrode layer with the top PDMS microfluidic channel. Instead, 30

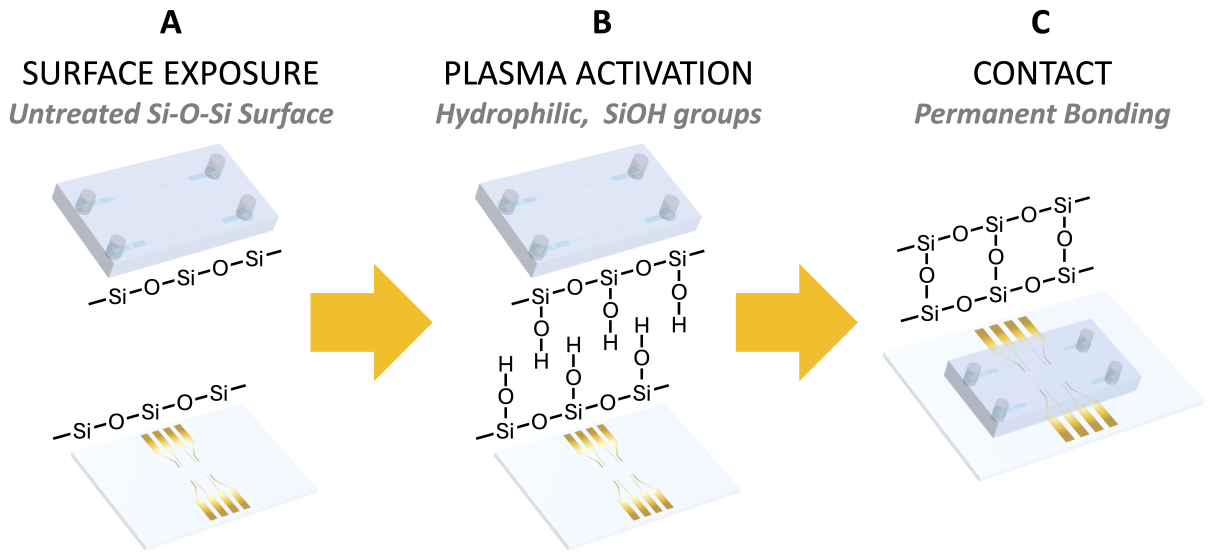


Figure 3.6: Plasma Bonding of PDMS and Glass. The cured PDMS with the embedded microfluidic channel is permanently bonded to a glass slide with pre-patterned electrodes. (A) Each surface, consisting of Si-O-Si groups, is treated with oxygen plasma. (B) The oxygen plasma activates each surface, rendering the surfaces hydrophilic with available Si-OH groups. (C) The activated surfaces are brought into contact, creating a covalent bond of Si-O-Si between the two surfaces. The microfluidic channel is fully sealed and ready to be used.

µL of a 2:1 mixture of methanol and DI water is pipetted on the glass electrodes slide after plasma treatment to facilitate alignment. The fluid serves as a temporary buffer between the PDMS channel and electrodes slide, giving time for the two components to be aligned under a microscope. Once aligned, the device is baked on a hotplate at 50°C for 2 hours to drive off excess solution and complete the contact-based plasma bonding.

3.4 Hardware Implementation

To measure the electrical resistance across the microfluidic channel, custom hardware and circuitry is required. The hardware used in Mechano-NPS [132] and Visco-NPS [159] implemented a standard 4-terminal measurement, which measured changes in current across a pair of inner electrodes as a feedback-loop constrained the outer electrodes to a constant 1 V potential. This set-up used bench-top components, including a power-supply, current pre-amplifier, and DAQ (data acquisition) terminal block. For this work, I implement a new hardware configuration that utilizes compact integrated circuit elements. This set-up uses new circuitry to enable simultaneous, multiplexed measurements of current and voltage across multiple electrode pairs. The following subsection will describe this new configuration in further detail.

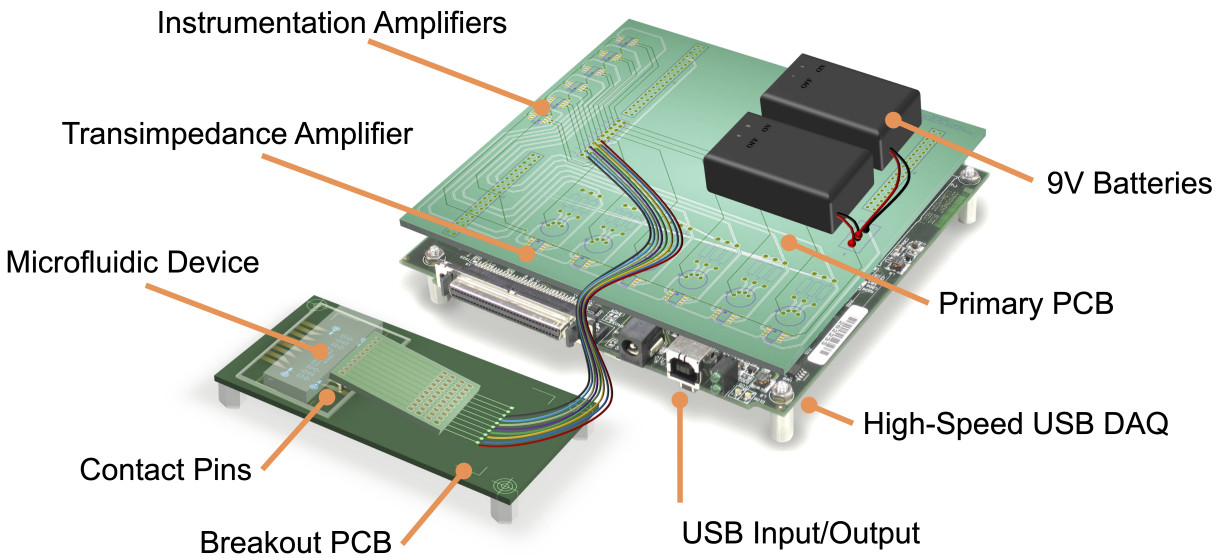


Figure 3.7: Schematic of Multi-Zone Data Acquisition Hardware Custom hardware circuitry is used to enable electrical resistance measurements across the microfluidic devices employed in this dissertation. The primary batter-powered PCB houses all the active components, including instrumentation amplifiers and transimpedance amplifiers. It directly connects to an off-the-shelf USB DAQ beneath. A separate breakout PCB, connected to the main PCB via re-configurable jumper wires, interfaces with the electrodes on the microfluidic device [170].

3.4.1 Multi-Zone Electronic Hardware Configuration

The hardware set-up described here, and used for the measurements described in Chapters 4 and 5, is termed the "Multi-Zone" configuration. Multi-Zone refers to the ability to simultaneous measure multiple, distinct "zones" along a microfluidic geometry. **Figure 3.7** details the primary components of the multi-zone hardware configuration. The design consists of a custom battery-powered primary PCB that includes six instrumentation amplifiers for measuring differential voltage and one transimpedance amplifier for measuring current. A separate breakout PCB interfaces with the contact electrodes on the microfluidic device. The breakout PCB and primary PCB are connected by jumper wires, allowing the circuitry to be reconfigured as needed. This flexible hardware layout ensures measurement compatibility with devices that have a various number of zones or a different electrode layout. The primary PCB is connected to a commercial high-speed USB DAQ, which sends power and data though a single USB to the computer. The USB Daq used for this set-up (MCC USB-2627) contains 16 single-ended analog inputs, enabling the simultaneous "multi-zone" measurement. Table 3.1 summarizes the specific components needed to replicate this hardware set-up.

The six instrumentation amplifiers on the multi-zone hardware allows for up to six voltage

Table 3.1: Multi-Zone Hardware Component Catalog.

Item	Description	Quantity
Electrical Enclosure	Type 4 Mild Steel Junction Box	1
Spring-Loaded Pogo Pin Connector	For Clamp: Position Spring Piston Connector, Through Hole, 10 pins, 2mm Pitch	1
Male Pin Rectangular Connector (Unshrouded)	For Clamp & Main PCB: Connector Header, Through Hole, 20 position, 2.54mm Pitch	3
Male Pin Rectangular Connector (Shrouded)	For Breakout: Male Connector Header, Through Hole, 10 position, 2.54mm Pitch	1
Female Socket Rectangular Connector	For Main PCB: Female Receptacle Connector, Through Hole, 40 Position , 2.54mm Pitch	3
9-Volt Battery Holder	For Main PCB: SBH-9V Battery Holder with Cover and Switch and 6 Inch Wires	2
9-Volt Battery	Standard 9-Volt Battery	2
Header Wire Terminal Block	For Main PCB: 3-Position Wire to Board	1
Female-to-Female Jumper Wires	Jumper Wire Female to Female 6.00” (152.40mm) 28 AWG	9
Transimpedance Amplifier (TIA)	TI OPA172	1
Instrumentation Amplifier (INA)	TI INA818	6
PCB Rotary Switch	For Selecting Variable Resistance	1
Resistors	For Matching Channel Resistance	3
Custom PCB (Main)	Primary PCB, Mounted Directly to USB DAQ via 3 Sets of 40 Position Female Receptical Connector	1
Custom PCB (Breakout)	Breakout PCB, Intermediary Between Main PCB and Clamp,Connected to Main PCB via Female-to-Female Jumper Wires	1
Custom PCB (Clamp)	Clamp PCB, Interfaces with Device via Pogo Pins, Connected to Breakout PCB via 2 Sets of 20 Position Connector Header	1
USB DAQ	MCC USB-2627, 1 MS/s sample rate, no enclosure	1
USB Cable	USB-A to USB-B cable	1

measurements, while a single transimpedance amplifier (TIA) measures the current. The TIA is set-up in a negative feedback loop, using a resistance value matched to the electrical resistance of the microfluidic channel itself. A typical channel, ranging in length from 10 to 25 mm, and filled with phosphate-buffered saline (PBS), has a total resistance of 10-25 $M\Omega$. **Figure 3.8** illustrates the circuit, with the electrical equivalent of a microfluidic channel modeled as a series of resistors. The amplifiers used are high-precision, low-noise

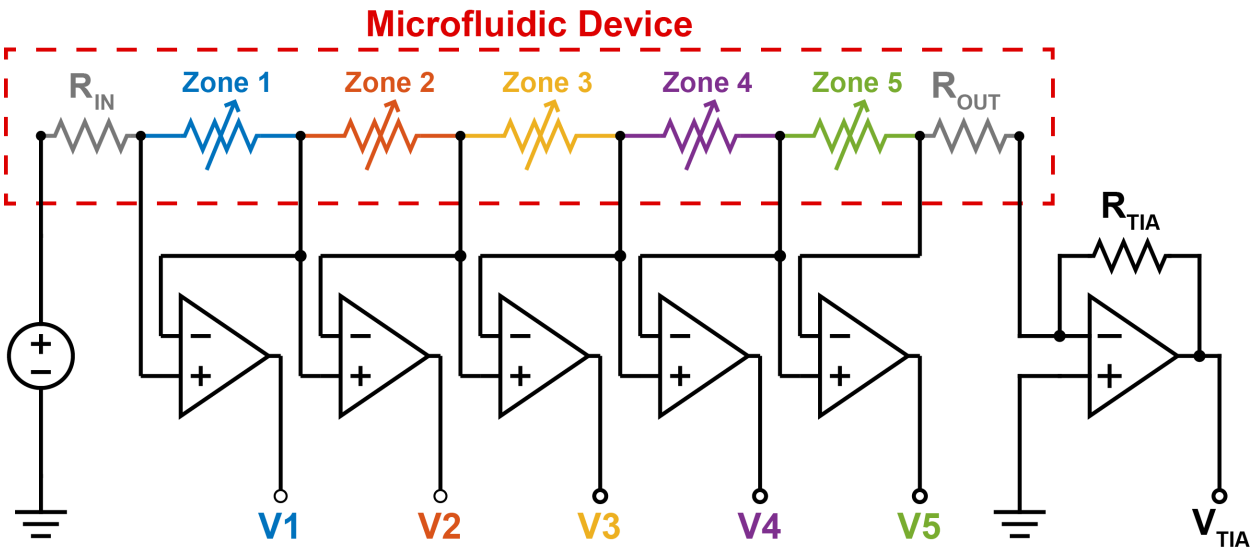


Figure 3.8: Multi-Zone Hardware Circuit Diagram The multi-zone hardware employs a simple circuit consisting of multiple operational amplifiers. In this diagram, the electrical equivalent of a microfluidic channel is divided in five distinct zones, with each zone modeled as a variable resistor. Additional fixed resistances are incorporated at either end of the modeled microfluidic channel, to account for reservoir resistances and interfacial resistances. Each "zone" is directly connected to a instrumentation amplifier that measures differential voltage, while the series current is measured by the a single transimpedance amplifier. Together, the variable resistance in each zone can be calculated.

components: the instrumentation amplifier can detect changes as low as 8 nV, while the transimpedance amplifier can measure down to 8 pA. This enables low-SNR, high sensitivity measurements, which is necessary given that a single cell transit event can result in signal deltas as low as a few hundred nanoamps. In summary, the multi-zone hardware outputs up to 6 independent voltages, and one current. Assuming a linear system, Ohm's law:

$$V = IR \tag{3.4}$$

is used to calculate the resistance of each zone, where V is the measured voltage, I is the measured current, and R is the ohmic resistance. Overall, this hardware enables new resistance-based measurements across microfluidic channels, providing new accessibility in design, and reducing the size and cost of components compared to previous hardware set-ups.

3.4.2 Experimental Hardware and Operation

For the microfluidic platforms described in this dissertation, the experimental set-up and operation largely relies on one bench-top component: the pressure controller. Pressure

driven flow is used to drive fluid flow, forcing the flow of cells through pores and narrow contraction channels. As opposed to volumetric driven flow (actuated via a syringe-pump), pressure driven flow creates more controllable, instantaneous flow. This simplistic set-up improves platform accessibility, removing the need for bulky bench-top hardware such as power supplies or complex high-speed cameras.

A Fluigent pressure controller (MFCS-EZ) is used to apply a constant pressure at the inlet of the microfluidic channel. Polytetrafluoroethylene (PTFE) tubing, a nonreactive, hydrophobic, biocompatible fluoropolymer is used as the interface between the device inlet and pressure source. A syringe is used to draw reagent or sample into one end of the tubing. The same end is then inserted into the microfluidic inlet hole, while the opposite end is connected to the pressure controller.

The typical experimental operation of a microfluidic chip is as follows: The PDMS channel is first passivated by introducing a solution consisting of 2% volume/volume of Tween-20 in PBS. Tween-20 is a polysorbate-type nonionic surfactant that coats the porous PDMS surface, reducing downstream biofouling effects [171] when biological samples, such as a cell suspension, is introduced. The solution is allowed to incubate in the channel for 15 to 30 min. After incubation, the solution is flushed out of the channel with PBS. A cell suspension, typically at a concentration of $1-2\times10^5$ cells/mL is then introduced into the device. Visual inspection under a microscope confirms free sample flow without any fluidic occlusion from debris particles. The device is then connected to the multi-zone electronic hardware, and a data acquisition session is begun and typically run for 5 - 10 min.

3.5 Software Implementation

Key to implementing NPS systems is the ability to record, analyze, and quantify electrical resistance signals. Here, I describe the generalized software implementation for recording and analyzing NPS signals. Various signal processing algorithms are implemented to process the signals and extract relevant parameters. Specific signal processing techniques unique to the platforms described in Chapters 4 and 5 will be later detailed in those respective chapters. First, the Multi-Zone hardware is controlled using a custom command-line based interface with a live graphical readout. After data acquisition, recorded signals are processed in two parts. First, the signal is refined to remove noise, artifacts, and baseline drift. Second, the refined signal is analyzed for relevant quantitative features relevant to the specific application. The following subsections review each part, from acquisition to analysis. The code described in this section is available in an online repository at: https://github.com/sohnlab.

3.5.1 Data Acquisition

A custom software interface written in MATLAB using built-in application packages from supported vendors, in this case Measurement Computing Corporation (MCC), is used to

interface with the Multi-Zone hardware set-up. Only a single USB is needed to interface between the computer and hardware, with power, commands, and data being transferred simultaneously. Because the output voltage is directly generated by the DAQ, the frequency and voltage of the signal is set within the script. The acquisition script also contains additional parameters to set, including sampling frequency and input recording duration, and plotting window duration. In a typical setup, a constant voltage of 5 to 10 V is applied across the device, with a sampling frequency of 10 kHz. The resulting DC current is measured using the transimpedance amplifier (TI OPA172) set to a gain of 10^{-7} V/A.

During an active data acquisition session, a live window readout of the measurement will be displayed **(Figure 3.9)**. This graphical window will show the measured resistances of each zone, as well as plots for the combined resistances and noise present in the system. This interface is critical for live user assessment of the signal quality and device condition. Device disruptions during measurement, such as from a sudden fluidic occlusion, can be actively monitored using this graphical window. This ensures that that the data recorded remains of consistent quality, and allows for flexibility in restarting an experimental run should anomalies arise.

3.5.2 Signal Processing

The raw data outputted by Multi-Zone Visco-NPS consists of a single dimension vector interlaced with the voltage of each zone (V1, V2, V3, etc.) and the single current for each sample taken (typical sample rate sufficient for NPS measurements is 10 kHz). The raw voltage and current recorded **(Figure 3.10A)** is parsed out and divided according to Ohm's law (Equation 3.4) to get the resistance **(Figure 3.10B)** for each zone. After the resistance signal for each zone is calculated, a baseline is fitted to the signal. Accurate baseline fitting is critical, because it enables 1.) the accurate calculation of signal deltas (like ΔR), used to estimate cells diameters (see Equation 3.2) and 2.) the accurate identification of cell transit events. To perform baseline fitting, an asymmetric least squares (ASLS) fitting algorithm is employed [172]. This algorithm takes into account the relative noise margin of the signal, down-weighting data points outside the noise margin, and fitting a curve to the remaining up-weighted data points. Given the right input settings, ASLS is robust enough to fit accurate baselines for NPS signals with varying pulse magnitudes and widths. Once an accurate baseline is fitted to the signal for each zone **(Figure 3.10C)**, cell transit events can be identified by tracking pulses that deviate significantly from the baseline **(Figure 3.10D)**. By identifying cell transit events from the first zone, the full signal cascade can be established by tracking immediate and sequential pulses in the following zones **(Figure 3.10E)**.

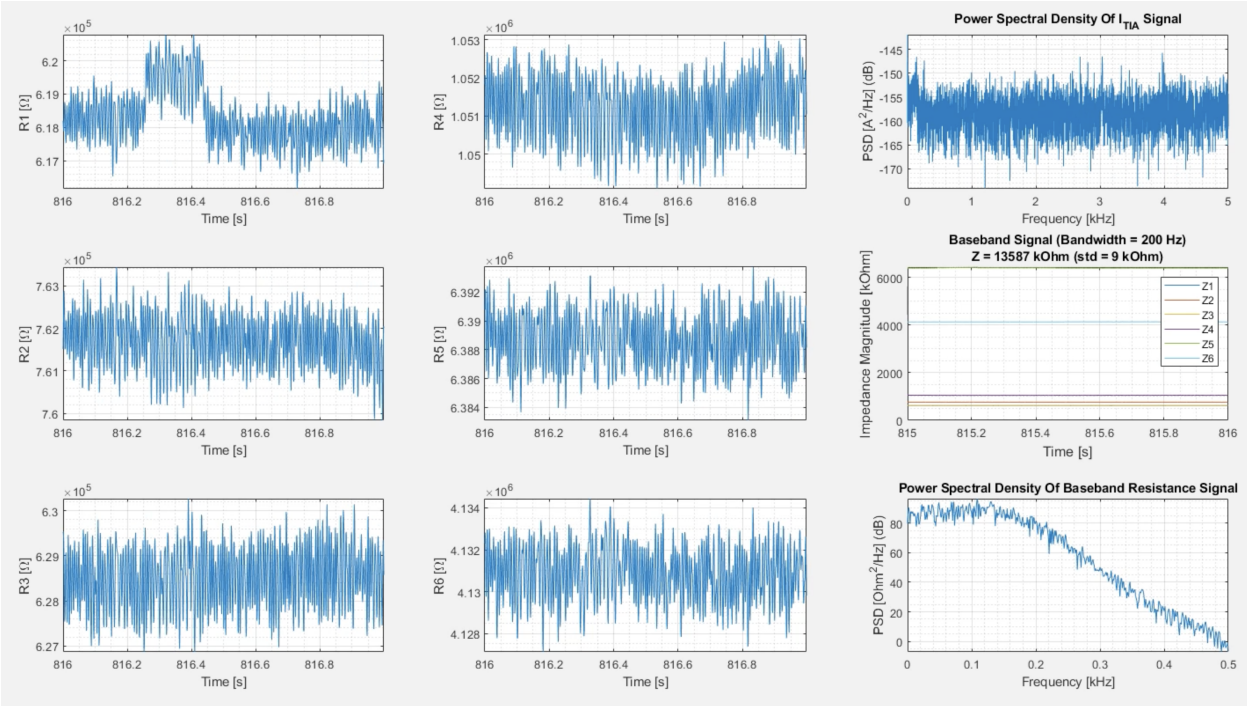


Figure 3.9: Data Acquisition Window Snapshot Displaying A Live Graphical Readout During Experimental Session. The data acquisition code used for NPS measurements presents a live readout during an active data acquisition session. The first 2 columns readout the resistances of up to 6 independent zones. In this static example, a cell has just entered the first zone, resulting in a rectangular pulse in the first, top-left graph. In the third column, the top graph displays the power spectral density of the current. This is useful for estimating the amount of noise present in the system. The middle graph in the third column displays the overall resistances of all the zones together. This is useful for ascertaining relative zone resistances and the total channel resistance. Finally, the bottom graph in the third column displays the power spectral density of the resistances, an alternative measure of noise present in the system.

3.5.3 Signal Analysis

Once cell transit events are identified, with the full corresponding signal cascade from each zone, the signal features themselves can be analyzed to extract quantitative metrics that relate back to the cellular biophysical properties. This includes pulse magnitude (see Equation 3.2) to determine cell size, or pulse width to determine deformability (see Equation 3.3). Local maximums and minimums in the subpulses can be identified be taking an approximate derivative of the signal ($\delta R/\delta T$). To do so can allow the extracted subpulse to be represented as a rectangularized signal [173], facilitating the extraction of features such as pulse magnitude and width. In the example presented in **Figure 3.10E**, the relevant features of the pulse include the sinusoidal component of the pulse. In this case, the sinusoidal feature

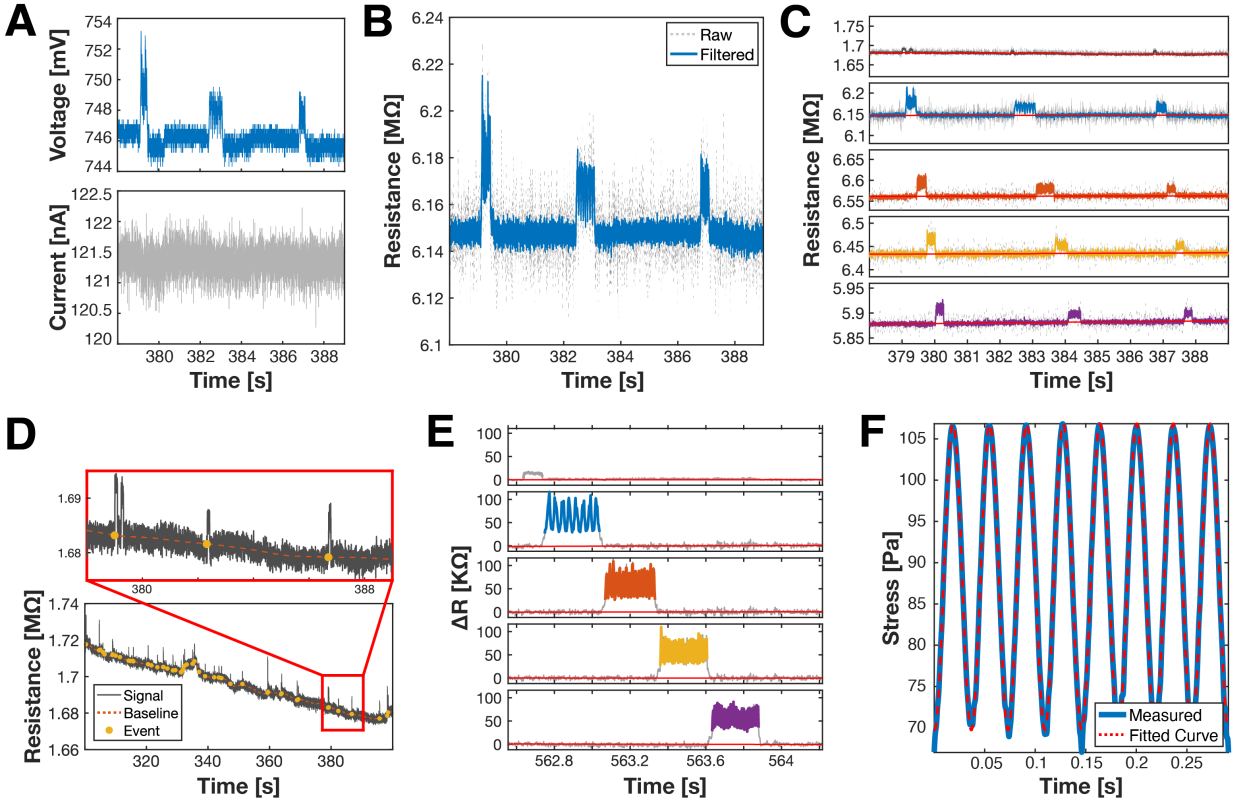


Figure 3.10: Signal Processing and Analysis Pipeline Using Custom MATLAB Code. (A) Raw voltage (top) and current (bottom) signals are recorded as a cells transit a Multi-Zone Visco-NPS microfluidic channel (see Chapter 4). (B) The resistance across the channel (obtained via Ohm's law from the raw current and raw voltage) is low-passed filtered to remove high frequency noise. (C) The baseline resistance (red line) is fitted to the resistance signal for each zone. (D) By tracking deviations from the baseline resistance, cell transit events are identified and parsed out from the full signal. (E) Relevant components from each parsed cell transit event are extracted, mainly pulse magnitude and width in the sizing pore, and sinusoidal pulses from the contraction zones. The baseline resistance is shown in (red), the parsed signal in (light grey), and the color highlights (dark grey, blue, orange, etc.) indicate the relevant signal components. (F) The sinusoidal signal component (shown is Zone 1) is used to model the stress on the cell. See Chapter 4 for further details [170].

is used to model cell stress, and is subsequently fitted to a standard stress-strain rheological relationship to extract specific viscoelastic properties **(Figure 3.10F)**. Chapter 4 presents additional details on this approach and methodology. Overall, multiple varying approaches, including manual user input, are employed to accurately analyze and quantify the features in the processed signals.

3.6 Conclusion

In this chapter, I introduced resistive pulse sensing (RPS) and node-pore sensing (NPS), the primary technology used in the microfluidic platforms described in Chapters 4 and 5. I extensively review the background and theory behind RPS and NPS and introduce previous approaches that have utilized NPS. Next, I thoroughly describe the methods used to fabricate microfluidic devices using soft-lithography. This section also included the patterning of the Ti/Pt/Au electrodes on glass and the final plasma-activated bonding of the devices. Finally, I detail the practical hardware and software implementation for the microfluidic platforms, from the data acquisition circuitry to the custom signal processing approaches in MATLAB. In the next chapter, I detail the development and application of Mult-Zone Visco-NPS (mz-visco-NPS), a comprehensive microfluidic platform for multi-frequency viscoelastic phenotyping of single cells.

Chapter 4

Multi-Zone Viscoelastic Node-Pore Sensing (mz-visco-NPS)

This chapter is adapted from a pre-print manuscript:
A. Lai, S. Hinz, A. Dong, M. Lustig, M. A. LaBarge, and L. L. Sohn, "Multi-Zone Visco-NPS: Microfluidic Platform for Multi-Frequency Viscoelastic Phenotyping of Single Cells", Under Review, 2024.

In this chapter, I introduce multi-zone visco-NPS (mz-visco-NPS), an optics-free, resistance-based microfluidic platform for single-cell viscoelastic phenotyping. mz-visco-NPS implements a series of sinusoidal contraction zones that deform cells at multiple distinct strain frequencies. Electrodes record resistance pulses as cells traverse the unique microfluidic geometry, enabling the measurement of whole-cell elastic storage (G') and viscous loss (G") moduli at throughputs of 600 cell/hr. I detail the theory and modeling behind the measurement, in addition to specific details about channel design and fabrication. In the results, I show differential measurements of single-cell viscoelastic phenotypes between Latrunculin-A treated and control cells, as well as between malignant (MCF-7), non-malignant (MCF-10A), and invasive (MDA-MB-231) breast epithelial cells. I also identify viscoelastic differences between average risk and high-risk breast cancer human mammary epithelial cells (HMECs). Overall, single-cell viscoelastic phenotypes reflect cell state and behavior and can serve as label-free biomarkers for fundamental and applied research. I demonstrate a versatile platform that can rapidly measure single-cell viscoelasticity, enabling a new dimension when investigating cellular traits and malignant progression.

4.1 Prior Work and Motivation

Viscoelastic measurements have previously been done using techniques such as atomic force microscopy (AFM) [116, 174] and optical stretchers or tweezers [175–177], but, as discussed in Section 2.3.2, there are important limitations to these technologies. AFM, the current

"gold standard", is only capable of measuring about 10 cells/hr while optical stretchers and tweezers are capable of marginally greater throughputs of 50 cells/hr [115, 127, 178, 179]. In the case of AFM, cell viscoelastic properties are dependent on the substrate stiffness to which a cell is adhered [159, 180]. High-throughput microfluidic techniques, described in Section 2.3.3, utilize constriction channels [129, 132], hydrodynamic stretching [128], or shear flow [135] to deform cells rapidly, up to 6×10^4 cells/hr. A key disadvantage with these methods is their inability to characterize frequency-dependent elastic G' and viscous G" of cells. They instead provide elementary parameters such as transit velocity through a constriction or morphology ratios, e.g. relative deformability. Further, these techniques rely on expensive, complex optical hardware. To address these limitations, we previously developed a microfluidic approach, visco-node-pore sensing (visco-NPS). Visco-NPS is a moderate-throughput (up to 600 cells/hr), all electronic-based microfluidics platform that utilizes NPS to measure the viscoelastic properties of single cells [159]. However, while this approach measured single cells, the accompanying rheological readouts were effectively a bulk measurement–the frequency dependent storage and loss moduli could only be determined for populations of cells and not individual cells. Multi-zone visco-NPS (mz-visco-NPS) is an new iteration of the original visco-NPS platform, enabling a true single-cell approach for viscoelastic phenotyping.

4.1.1 Significance of Single-Cell Viscoelasticity

Cells are intrinsically dynamic viscoelastic materials, consisting of elastic biopolymers and viscous fluids that comprise the cytoskeleton and the cytoplasm, respectively [181–183]. Fluctuations in a cell's viscoelastic phenotype have been correlated with a range of biological processes—from cell growth, motility, and behavior [141, 184, 185] to the epithelial-to-mesenchymal (EMT) transition [159]. Previous studies have described how viscoelasticity can reflect metastatic potential in breast epithelial cells [186], assess cell viability after cryopreservation [187], or monitor nuclear reorganization during osteoblast differentiation10. Overall, viscoelasticity is an inherent physical trait of cells that serves as a label-free biomarker of cell state and function. Measuring the viscoelastic properties of cells could complement canonical molecular biology approaches, such as genetic sequencing or protein assays, and potentially broaden mechanical phenotyping as a tool for both fundamental and applied research [109, 113, 115, 125]. As discussed thoroughly in Section 2.3.4, single-cell biomechanics have already been used to explore malignant pleural effusions [148], detect oral cancer [188], and differentiate drug-resistant leukemia cell lines from their drug-sensitive counterparts [151].

4.2 Approach and How It Works

Mz-visco-NPS **(Figure 4.1A)** consists of multiple sinusoidal contraction "zones"—each with a unique periodicity—aligned in series. Using the multi-zone hardware (see Section 3.4), Mz-visco-NPS incorporates a four-point probe measurement with additional sensing electrodes

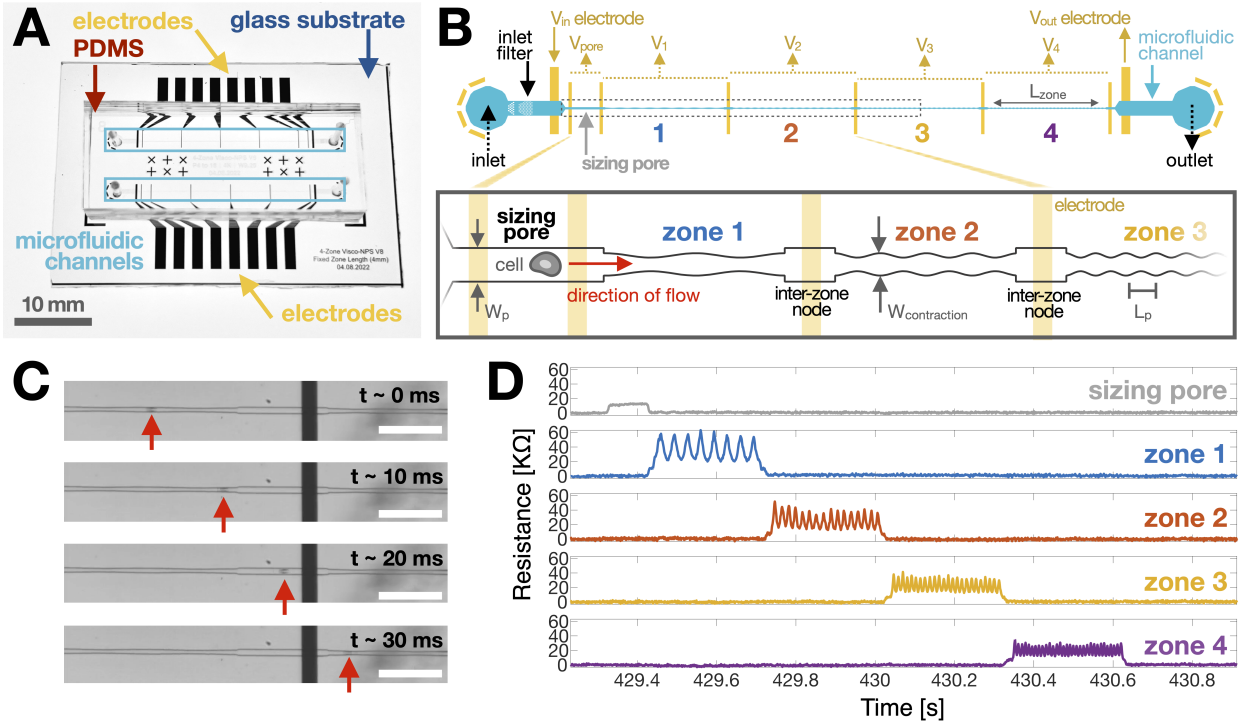


Figure 4.1: Multi-Zone Visco-NPS Overview. (A) Photograph of the microfluidic platform, which consists of 2 independent microfluidic channels (blue boxes) embedded in PDMS and aligned to a glass substrate with prefabricated Pt electrodes and Au contact pads. Scale bar = 10 mm. (B) Schematic of a single mz-visco-NPS device (blue), consisting of an inlet filter, a sizing pore, and 4 contraction zones. The electrodes (gold) are aligned to the microfluidic channel. The outer electrodes, V_{in} and V_{out}, apply a DC voltage across the channel. Pairs of inner electrodes, labeled as V_{pore}, V_1, V_2, etc., measure the differential voltage across the sizing pore and each zone. The inset illustrates the sinusoidal geometry of the contraction zones: the width of each zone is described by $w_{contraction} = w_0 + acos(\omega t)$, where w_0, a, and ω are the initial width, the strain amplitude, and deformation frequency, respectively. Each zone has a constant total length (L_{zone}) and a different period length (L_p). (C) From top to bottom, time snapshots of a single MCF-7 cell (indicated by a red arrow) exiting one sinusoidal contraction zone (L_{zone} = 2 mm, L_p = 300 μm, $w_{contraction} = 11.25 + 2.75cos(\omega t)\mu m$), transiting though an inter-zone node of width w_p = 21 μm, and finally entering a new sinusoidal contraction zone of different frequency (L_p = 200 μm). The vertical black bar shown is an electrode. Scale bar = 200 μm. (D) Representative resistive pulses caused by an MCF-7 cell transiting an mz-visco-NPS microfluidic channel (L_{zone} = 4 mm, L_p = 500, 250, 167, 125 μm, $w_{contraction} = 11.25 + 2.75cos(\omega t)$ μm). The signals are aligned in time; resistive pulses cascade (starting from the sizing pore to zone 1, zone 2, etc.) as the cell transits the microfluidic zones. The periodicity of the signal reflects the periodicity of the applied strain: as the cell transits from zone 1 to zone 4, L_p is reduced from 500 μm to 125 μm. Correspondingly, the applied strain frequency increases from approximately 30 to 126 hz. An applied pressure of 13.8 kPa was used.

that border each contraction zone **(Figure 4.1B)**. As pressure drives cells through the microfluidic channel **(Figure 4.1C)**, the corresponding resistance pulse in each zone **(Figure 4.1D)** reflects each cell's viscoelastic response to the specific applied strain within that zone. With mz-visco-NPS, we achieve a moderate-throughput rate of up to 600 cells/hr while measuring the dynamic rheology of each single cell, namely the frequency-dependent complex shear modulus: G* = G' + iG", where G' is the storage (elastic) modulus and G" is the loss (viscous) modulus. G' describes the in-phase response to applied oscillatory stress, whereas G" describes the out-of-phase response. Section 4.3.1 further defines the complex shear modulus. We show that mz-visco-NPS can detect breast epithelial cells shifting toward a more compliant, less elastic phenotype when subject to actin cytoskeletal perturbation. Additionally, we identify viscoelastic differences among single cells from three different breast epithelial cell lines, MCF-10A, MCF-7, and MDA-MB-231. We also characterize different zone configurations, exploring how the applied frequency order and strain duration affect our viscoelastic measurements. Finally, we show that mz-visco-NPS measurements uncover broad single-cell heterogeneity and population differences among average- and high-risk primary human mammary epithelial cells (HMECs).

4.3 Theory and Modeling

To measure viscoelastic properties, mz-visco-NPS models that stress and strain applied on each transiting cell. The following subsections describe the specific approaches used, and methodically detail the model and background theory.

4.3.1 Dynamic Viscoelasticity

Viscoelasticity is a material property that describes encompasses both the elastic and viscous characteristics of a material under stress or strain [189–191].

Elasticity is the tendency of a solid to return to its original shape or form after an applied force is released. For example, rubber bands are a common material that is highly elastic. Elastic materials exhibit a time-independent behavior, and is a material property that describes solids. For an elastic material, the relationship between stress σ and strain ε is:

$$\sigma = E\varepsilon \tag{4.1}$$

where E is a scalar material factor called the elastic modulus, or Young's modulus. From Equation 4.1, we see that a fully elastic material will have a linear response between stress and strain.

On the other hand, viscosity describes a fluid's resistance to flow. For example, syrup has a higher viscosity (greater "resistance to flow") than water. Unlike elasticity, viscosity exhibits

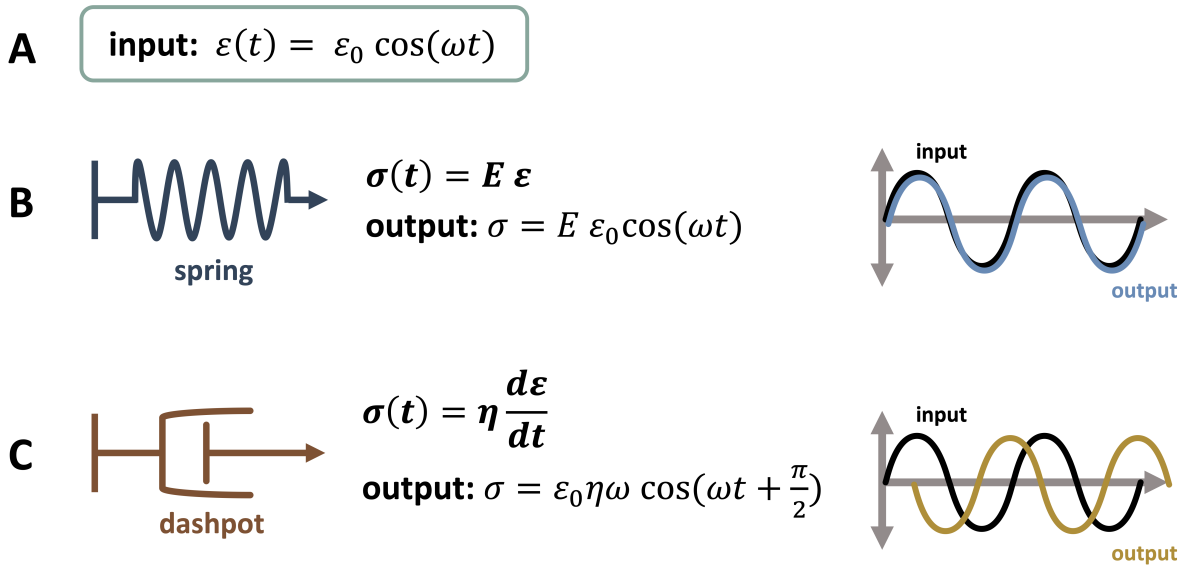


Figure 4.2: Example of Viscoelastic Response to Dynamic Oscillatory Input. In dynamic viscoelastic measurements, an oscillatory stress or strain is applied. In this example, (A) an oscillatory strain in the form of a cosine function is the input to either an elastic spring or viscous dashpot. (B) The resulting output stress for a purely elastic component. Note that the input and output are in-phase. (C) The resulting output stress for a purely viscous component. Note that the input and output are out-of-phase by 90°.

a time-dependent behavior, and is a material property that describes fluids. For a Newtonian fluid, the relationship between stress σ and strain ε is:

$$\sigma = \eta \frac{\partial \varepsilon}{dt} \tag{4.2}$$

where η is the material viscosity, and $\frac{\partial \varepsilon}{dt}$ is the strain rate.

Viscoelastic materials exhibit both elastic and viscous behavior. Together, from Equation 4.1 and 4.2, stress on a viscoelasticity material is a function of both strain magnitude and strain rate. Many materials, including plastics, metals, and most biological matter, such as cells, exhibit viscoelastic behaviors. Viscoelastic materials are commonly described with linear models, consisting of elastic springs or viscous dashpots, connected in series or in parallel.

In static rheological testing, viscoelastic material properties are probed by applying a constant stress (known as creep) or a constant strain (known as stress relaxation). The resulting stress-strain relationship is used to characterize the material's viscoelastic proprieties. In dynamic rheological testing, the input stress or strain is oscillatory, with a specific wave

frequency. **Figure 4.2A** gives an example of an oscillatory input, in the form of a cosine wave. When this input is given to a purely elastic material, as modeled by a spring, or a purely viscous material, as modeled by a dashpot, we get two distinctive behaviors. From Equation 4.1, a purely elastic material has a linear stress-strain relationship. Thus, a cosine strain input results in an in-phase cosine stress output **(Figure 4.2B)**. In contrast, from Equation 4.2, a purely viscous material has a non-linear stress-strain relationship. Here, a cosine strain input results in an 90° out-of-phase cosine stress output **(Figure 4.2C)**. In this example, a viscoelastic material would have a phase-delayed response that is between purely elastic (0°), and purely viscous (90°). Critical to dynamic viscoelastic measurements is the frequency dependency: the frequency of the input impacts the resulting measurements. In doing so, we get add additional time component information with the resulting data. Time information can be crucial: given a long enough observation time (low frequency), a solid material might appear to flow, and vice versa. As a crude analogy, consider taking a time-lapse video of a mountain: at human time scales (tens of years), it would appear motionless and solid; however, at geological time-scales (billions of years) the mountain would appear fluid, moving and evolving with the surrounding landscape. Hence, the duration or time an observation is made, or the frequency at which the measurement is taken, is important to the resulting data.

To characterize dynamic, frequency-dependent viscoelastic measurements, we use a quantity known as the complex shear modulus (also known as dynamic modulus).

To define the complex shear modulus, Euler's equation is used for complex analysis:

$$p^* = cos(\omega t) + isin(\omega t) = e^{i\omega t} \tag{4.3}$$

Where p^* simply represents any complex quantity. From Euler's, we define an arbitrary complex stress input, in the form of:

$$\sigma^* = \sigma_0 cos(\omega t) + i\sigma_0 sin(\omega t) = \sigma_0 e^{i\omega t} \tag{4.4}$$

From the analysis in **Figure 4.2**, we know that an oscillatory input, as defined in Equation 4.4, to a viscoelastic system results in a phased-delayed output. Thus, the output to the complex input stress (Equation 4.4) will be:

$$\varepsilon^* = \varepsilon_0 cos(\omega t - \phi) + i\varepsilon_0 sin(\omega t - \phi) = \varepsilon_0 e^{i(\omega t - \phi)} \tag{4.5}$$

where each component is phase delayed by ϕ. Finally, similar to the elastic modulus in Equation 4.1, the complex shear modulus (G^*) is defined as the complex stress divided by the complex strain:

$$G^* = \frac{\sigma^*}{\varepsilon^*} \tag{4.6}$$

Plugging in Equation 4.4 and 4.5 into equation 4.6, we get:

$$G^* = \frac{\sigma_0 e^{i\omega t}}{\varepsilon_0 e^{i(\omega t - \phi)}} = \frac{\sigma_0}{\varepsilon_0} e^{i\phi} = \frac{\sigma_0}{\varepsilon_0}(cos(\phi) + isin(\phi)) \tag{4.7}$$

The complex modulus is typically described in the form:

$$G^* = G' + G" \tag{4.8}$$

where G' is the in-phase storage modulus:

$$G' = \frac{\sigma_0}{\varepsilon_0}(cos(\phi) \tag{4.9}$$

and $G"$ is the out-of-phase loss modulus:

$$G" = \frac{\sigma_0}{\varepsilon_0}(sin(\phi) \tag{4.10}$$

All together, the storage and loss moduli reflect the material's elastic and viscous behavior, respectively. A larger G' indicates a stiffer phenotype, while a greater G'' indicates a more viscous phenotype.

4.3.2 Stress Model

The working principle behind single-cell viscoelastic measurements using an electronics-based node-pore-sensor was previously described by J. Kim, et. al. [159]. Fundamentally, the electric resistance across a microfluidic channel is proportional to a transiting cell's diameter—a larger cell will partially block more current than a smaller cell. Measuring the channel resistance can thus quantitatively assess a cell's dynamic deformation in response to the oscillatory stress applied by the contraction channel walls.

If we consider all external forces surrounding the cell and assume constant velocity, the stress on the cell within each contraction zone in mz-visco-NPS, σ, can be modeled as:

$$\sigma = \frac{2\Delta P_{avg} w_{contraction}}{\mu_f \pi D_d} \tag{4.11}$$

where ΔP_{avg} is the average pressure difference across a strained cell of a given diameter d , $w_{contraction}$ is the oscillating width of the contraction channel, μ_f is the coefficient of friction between the strained cell and channel wall, and D_d is the diameter of the deformed cell in contact with the channel wall. ΔP_{avg} is a scalar value that is computationally modeled by COMSOL® [17] **(Figure 4.3)**.

We can determine D_d by using the measured resistance signal and Equation 3.2, which rearranging, gives:

$$D_{\text{cell}} = \frac{\Delta R D_{\text{eff}}^2 L}{\frac{\Delta R 0.8 L}{D_{\text{eff}}} + R} \tag{4.12}$$

where D_{cell} is the diameter of the free cell, ΔR is the change in resistance, R is the base resistance, D_{eff} is the effective diameter of the channel, and L is the length of the channel. D_{eff} is determined empirically for each device design by calibrating the cell diameters measured with the device to those obtained by a commercial cell counter (Millipore Scepter 2.0). From Equation 4.12, we can measure the dynamic deformation of the cell as it transits the contraction channel. D_{cell} is related to D_d by conservation of volume:

$$D_d = \sqrt{\frac{2D_{\text{cell}}^3}{3w_{\text{contraction}}}} \tag{4.13}$$

The stress on the cell can then be determined using Equation 4.11. Using least squares fitting, we fit the modeled stress to the following standard rheological relationship [159]:

$$\sigma = \sigma_p + G'\varepsilon_0 \cos(\omega t) + G''\varepsilon_0 \sin(\omega t) \tag{4.14}$$

where is σ_p prestress, and ε_0 is prestrain. From Equation 4.14, we can numerically calculate the frequency dependent storage G' and loss G'' moduli.

4.4 Design and Experimental Methods

In this section, I describe the unique sinusoidal geometry employed in mz-visco-NPS. Likewise, I describe the relevant characterizations made on the channel design, and the specific

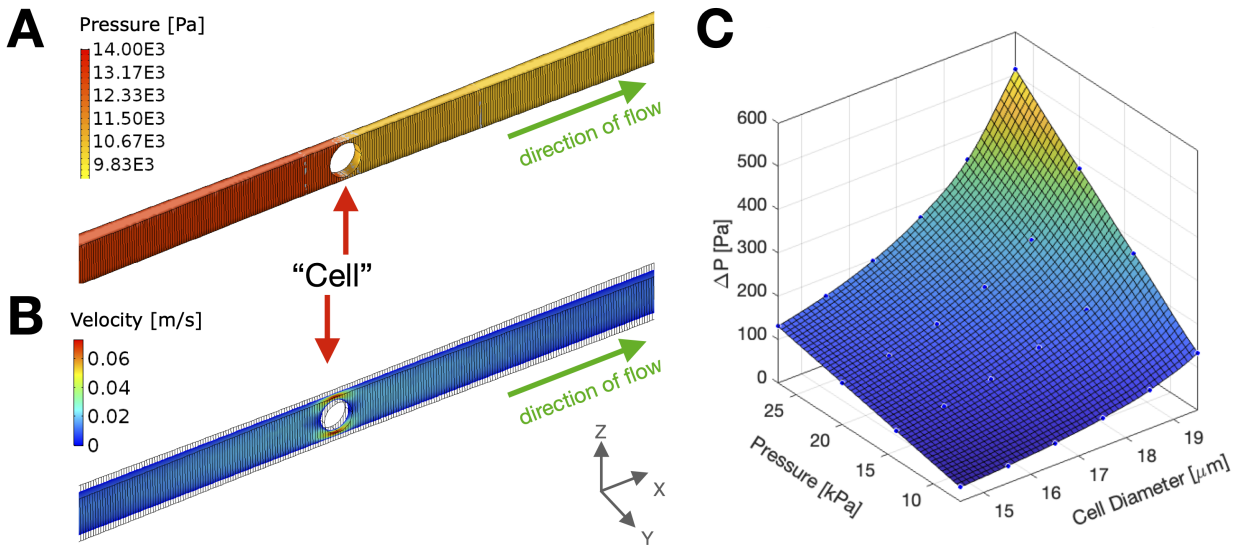


Figure 4.3: COMSOL Modeling of Cell in a Contraction Zone. The average pressure across a deformed cell is modeled via COMSOL to estimate the stress on the cell. (A) Pressure gradient across the channel with a cell present. The cell is modeled as a cylindrical open gap in the channel geometry. (B) Velocity gradient across the channel with a cell present. (C) Surface plot interpolation of the average pressure across a deformed cell (ΔP_{avg}), which is a function of inlet pressure and cell diameter.

experimental methods. The mz-visco-NPS device consists of a microfluidic channel embedded into a polydimethylsiloxane (PDMS) mold that is bonded to a glass substrate with pre-fabricated platinum electrodes (Pt) and gold (Au) contact pads. Specific methods and techniques related to mz-visco-NPS device fabrication are described in Section 3.3

4.4.1 Channel Design Overview

The mz-visco-NPS platform consists of 3 primary features: an inlet filter, a sizing pore, and multiple sinusoidal contraction zones in series, each separated by an "inter-zone" node. Multiple platinum (Pt) measurement electrodes are aligned to the channel inlet, outlet, and inter-zone nodes **(Figure 4.1B)**. This electrode configuration helps maintain adequate signal-to-noise ratio (SNR) across each contraction zone. The voltage across each zone is recorded using custom hardware that enables multi-zone data acquisition in an inexpensive, compact form factor that does not rely on optical hardware **(Figure 3.7)**. The two outermost electrodes (V_{in} and V_{out}) drive current through the microfluidic channel, while pairs of inner electrodes measure the potential across the sizing pore (V_{pore}) and each contraction zone (V_1, V_2, etc.). The inlet filter removes cellular clusters or debris that might otherwise obstruct the sinusoidal contraction zones and is comprised of an array of pillars spaced W_p apart. W_p is designed to be two standard deviations greater than the mean cell diameter (Table 4.1) to ensure that transiting cells do not experience an applied strain. The sizing pore

measures the free-cell diameter of a cell, D_{cell}, via the Coulter principle (see section 3.1.1). As it transits the pore, a cell partially blocks the flow of current, leading to a temporary increase in the pore's resistance **(Figure 4.1D)**. The magnitude of the change in resistance is proportional to the volume ratio of the cell to the pore, i.e. $\Delta R \quad Vol_{cell}/Vol_{pore}$. The contraction zones measure the cell's viscoelastic response to the specific applied strain and frequency in each zone. The zones are positioned in series, each with a periodically changing width, $W_{contraction} = W_0 + acos(\omega t)$, where W_0, a, and ω are the initial width, the strain amplitude, and deformation frequency, respectively. ω is modulated by controlling each zone's period length, L_p. For the experiments described here, we employed a $W_{contraction}$ corresponding to an approximate strain of $\varepsilon = 0.4 + 0.15cos(\omega t)$. Specific channel geometries used for each cell type are detailed in Table 4.1 and Table 4.2. The measured resistance pulses are processed **(Figure 3.10)** and fitted to a rheological stress-strain relationship (see subsection 4.3.2) to calculate the frequency dependent elastic G' and viscous G" moduli.

Table 4.1: mz-visco-NPS channel dimensions and strain applied to each cell type. W_p corresponds to the width of the inter-zone nodes and $W_{contraction}$ is the contraction channel width. D_{cell} is the free cell diameter (mean ± standard deviation), and ϵ is the applied strain to the cells.

Cell Type	Avg. D_{cell} [μm]	W_p [μm]	$W_{contraction}$ [μm]	Height [μm]	ϵ
MCF7	18.91 ± 0.67	21	$11.25 + 2.75\cos(wt)$	32.97 ± 1.91	$0.4 + 0.15\cos(wt)$
MDA-MB-231	15.27 ± 0.63	17	$9.25 + 2.25\cos(wt)$	28.43 ± 1.15	
MCF10A	15.39 ± 0.76				
HMEC	16.11 ± 1.06				

Table 4.2: Microfluidic channel lengths and calculated effective diameters for 3-, 4-, and 5-zone devices. D_{eff} is the calculated effective diameter of the pore. L_{pore} is the length of the sizing pore, L_{zone} is the length of the contraction zone, and L_{p1}, L_{p2},..., L_{pn} where n is the zone number, are the period lengths of zones 1, 2, ..., n, respectively.

No. Zones	L_{pore} [mm]	L_{zone} [mm]	L_{p1} [μm]	L_{p2} [μm]	L_{p3} [μm]	L_{p4} [μm]	L_{p5} [μm]	D_{eff} [μm] $W_p = 21$ μm	D_{eff} [μm] $W_p = 17$ μm
3	1	6	500	200	125	–	–	18.95	16.70
4	1	4	500	250	167	125	–	18.85	16.70
4	1	6	500	250	167	125	–	19.25	16.65
5	1	2	500	286	200	154	125	20.35	16.4

4.4.2 Cell Culture and Sample Preparation

MCF-10A (ATCC CRL-10317) cells were cultured in DMEM/F12 (Gibco 11320033), supplemented with 5% horse serum, 1% Pen-Strep, 20 ng/mL human Epidermal Growth Factor, 0.5

µm/mL hydrocortisone, 100 ng/mL Cholera Toxin, and 10 µg/mL insulin. MCF-7 (ATCC HTB-22) cells were cultured in RPMI-1640 (Gibco A1049101) supplemented with 10% fetal bovine serum (FBS) and 1% Pen-Strep. MDA-MB-231 (ATTC HTB-26) cells were cultured in 50:50 DMEM:RPMI-1640 supplemented with 10% FBS and 1% Pen-Strep. All cell cultures were maintained at 37°C in 5% CO2 and routinely passaged, per published protocols [192], once they reached 80-90% confluence. Cells were dissociated with 0.25% trypsin/EDTA for either 3-5 min (MCF-7 or MDA-MB-231 cells) [193, 194] or 10-15 min (MCF-10A cells) [195] at 37°C, washed with respective growth media, centrifuged at 200 RCF for 5 min, and re-suspended at a concentration of 1-2 $\times$ 10^5 cells/mL in PBS. Single-cell suspensions were subsequently filtered with a 20 µm filter to remove cellular clumps and then placed on ice prior to being injected into prepared devices for measurement.

Primary HMECs were cultured using previously published protocols [196, 197]. HMECs were grown in M87A medium. Table 4.3 identifies the strain, age, and breast cancer risk status. Comprehensive details regarding the development and culture of the HMECs used in this study can be found at the Human Mammary Epithelial Cell (HMEC) Bank Website [198].

Table 4.3: Human Mammary Epithelial Cells (HMEC) Used In This Study. Primary HMECs were grown at 37°C in M87A medium containing cholera toxin (CT) and oxytocin (X).

Spec ID	Media	Freeze-down #	Age	Risk Status
C051C	M87A+CT+X	CB318	33	Average Risk
C064PDL	M87A+CT+X	CC475	40	Average Risk
C073C	M87A+CT+X	CB317	33	Average Risk
C023SCL	M87A+CT+X	CC340	35	High Risk (BRCA1)
C078SCL	M87A+CT+X	CA993	24	High Risk (BRCA1)
C147SCL	M87A+CT+X	CC507	33	High Risk (BRCA1)

For experiments involving pharmacological treatment for cytoskeletal perturbations, Lat-A was used to destabilize actin polymerization in MCF-7 cells [199, 200]. Lat-A (Abcam) was reconstituted in ethyl alcohol and added to MCF-7 cell culture medium at a concentration of 1 µg/mL. Cells were then incubated at 37°C for 90 min. The concentration and incubation time of LatA was chosen to have a sufficient effect on the cells and is based on previously published work [151, 201]. Cells were dissociated with 0.25% trypsin/EDTA, rinsed with growth medium, centrifuged at 0.2 RCF for 5 min, re-suspended in PBS at a concentration of 1-2$\times$$10^5$ cells/mL, filtered with a 20 µm filter, and placed on ice before injection into devices for measurement. To confirm actin disruption, cells were fixed with 4% w/v paraformaldehyde in PBS for 15 min and permeabilized with 0.2% v/v Triton-X (Sigma-Aldrich) in PBS for 5 min. Cell nuclei and actin filaments were counter-stained with 4',6-diamidino-2-phenylindole (DAPI, Sigma-Aldrich) and rhodamine phalloidin (Thermo-Fisher Scientific), respectively,

using the manufacturers' protocols. Stained cells were imaged with a Nikon Eclipse TE2000 inverted fluorescent microscope.

4.4.3 Data Acquisition

To measure simultaneously the resistance of multiple zones, a multi-zone measurement was employed, as described in Section 3.4. A constant voltage of 5 to 7 V was applied across the outermost electrodes, and the resulting DC current, I_m, was measured using a transimpedance amplifier (TI OPA172) set to a gain of 107 V/A. The voltage across each zone was independently measured by an instrumentation amplifier (TI INA818) connected to the electrode pairs across each contraction zone **(Figure ??)**. The measured voltages, up to 6 differential voltages (V_{pore}, V_1, V_2 etc.), and one transimpedance amplifier output voltage (V_{TIA}) were sampled with a USB-2627 multi-channel data acquisition board (Measurement Computing Corporation) at 10^4 samples/s. The data was transferred by USB to a PC running a custom MATLAB data acquisition interface, available on GitHub (https://github.com/sohnlab/mz-visco-NPS). Because all zones were electrically in series, the current through each zone was equivalent to the measured current, I_m. The resistance of each zone (R_{pore}, R_1, R_2, etc.) was therefore calculated by dividing the measured zone voltage with the single measured current ($R_{pore} = V_{pore}/I_m$, $R_1 = V_1/Im$, etc.).

4.4.4 Signal Processing and Analysis

As described in Section 3.5, custom MATLAB code was used to process and analyze the measured resistance signals. The command-line interface code used for processing is available on GitHub (https://github.com/sohnlab/mz-visco-NPS). To recap briefly, raw resistance signals **(Figure 3.10A)** are processed through a low-pass filter and a moving median window **(Figure 3.10B)**. The signals are then normalized to the baseline resistance **(Figure 3.10C)**, and distinct cell transit events are identified by tracking signal deviations from the baseline resistance **(Figure 3.10D)**. Relevant signal features are then extracted from each identified cell transit event **(Figure 3.10E)** and used to model single-cell stress (see subsection 4.3.2). The modeled stress (from the measured resistance pulses) are processed and fitted to a rheological stress-strain relationship **(Figure 3.10F)** to numerically calculate the elastic G' and viscous G".

To determine statistical significance, a non-parametric Wilcoxon signed-rank test or Kruskal-Wallis rank test was performed in R. All tests used a significance level of $\alpha = 0.05$. For experiments with multiple comparisons, a Benjamini-Hochber procedure was applied to correct for Type 1 false positive errors. To determine sample sizes, a power analysis, with means estimated from previous studies [132], was performed to ensure that $n \geq 99$ cells provided adequate power ($\pi \geq 80$) for all experimental groups.

4.5 Results and Discussion

We evaluated different breast epithelial cells for their viscoelastic properties. Immediately prior to introducing cells, mz-visco-NPS devices were exposed to an oxygen plasma (200 mTorr, 30 W, 2 min, Harrick Plasma) to render the PDMS channel hydrophilic. After plasma treatment, a nonionic surfactant solution of 2% v/v Tween-20 in PBS was incubated in the channel for 5 min to prevent potential biofouling [171]. Finally, pressure-driven flow (20.7-27.5 kPa for MCF-10A and MDA-MB-231 cells; 13.8-20.7 kPa for MCF-7 cells; 20.7 kPa for HMEC; Fluigent MFCS-EZ) was used to drive cells through the channel.

4.5.1 Measuring the Disruption of the Actin Cytoskeleton

To demonstrate that mz-visco-NPS is capable of distinguishing different viscoelastic properties, we screened MCF-7 cells whose cytoskeleton was perturbed with the actin polymerization inhibitor, Latrunculin-A (Lat-A) **(Figure 4.4A)** [199, 200]. We determined that the average cell diameter of Lat-A-treated (n=99) and untreated control (n=99) cells populations were 17.8 ± 1.0 µm and 18.4 ± 0.9, respectively **(Figure 4.4B i)**. Although Lat-A treated cells traveled faster than untreated control cells through the platform **(Figure 4.4B ii)**, this did not lead to significantly different applied frequencies between the two **(Figure 4.4 B iii)**: a range of 30-126 Hz was achieved across the device, with the lowest frequency in zone 1 and successively higher frequencies in subsequent zones.

In contrast to the untreated control cells, we observed a decrease in elastic G' in Lat-A treated cells for all measured frequencies, indicating that they had become more compliant **(Figure 4.4C and Figure 4.5A)**. This is consistent with previous studies that also report a softening of the cell after drug-induced actin filament disruption [159, 201]. The smaller diameter, faster transit time, and lower elastic G' modulus of the Lat-A treated population are all representative of a more compliant cell due to a disrupted actin cytoskeleton. Beyond population-level differences in elastic G', we also observed significant cell-to-cell heterogeneity, with cells showing a range of elastic G' from soft to stiff. Nearly 20% of the Lat-A treated cells had an elastic G' similar in magnitude to the mean elastic G' of the control cells. We hypothesize that these particular cells may have recovered more quickly from actin depolymerization. Cells can recover from actin depolymerization in as little as one hour [202], well within the timeframe of our mz-visco-NPS experiments (see Section 4.4).

When comparing the viscous G" between the Lat-A-treated and control cells **(Figure 4.4D and Figure 4.5B)**, we did not observe significant differences. Broad viscoelastic heterogeneity was observed between the two groups and among single cells. Up to 50% of our single-cell observations had no discernible viscosity, defined as a viscous G" modulus ¡ 0.1 Pa in at least one zone. Nonetheless, mz-visco-NPS is still capable of measuring the contribution of the actin cytoskeleton to the whole-cell elastic phenotype.

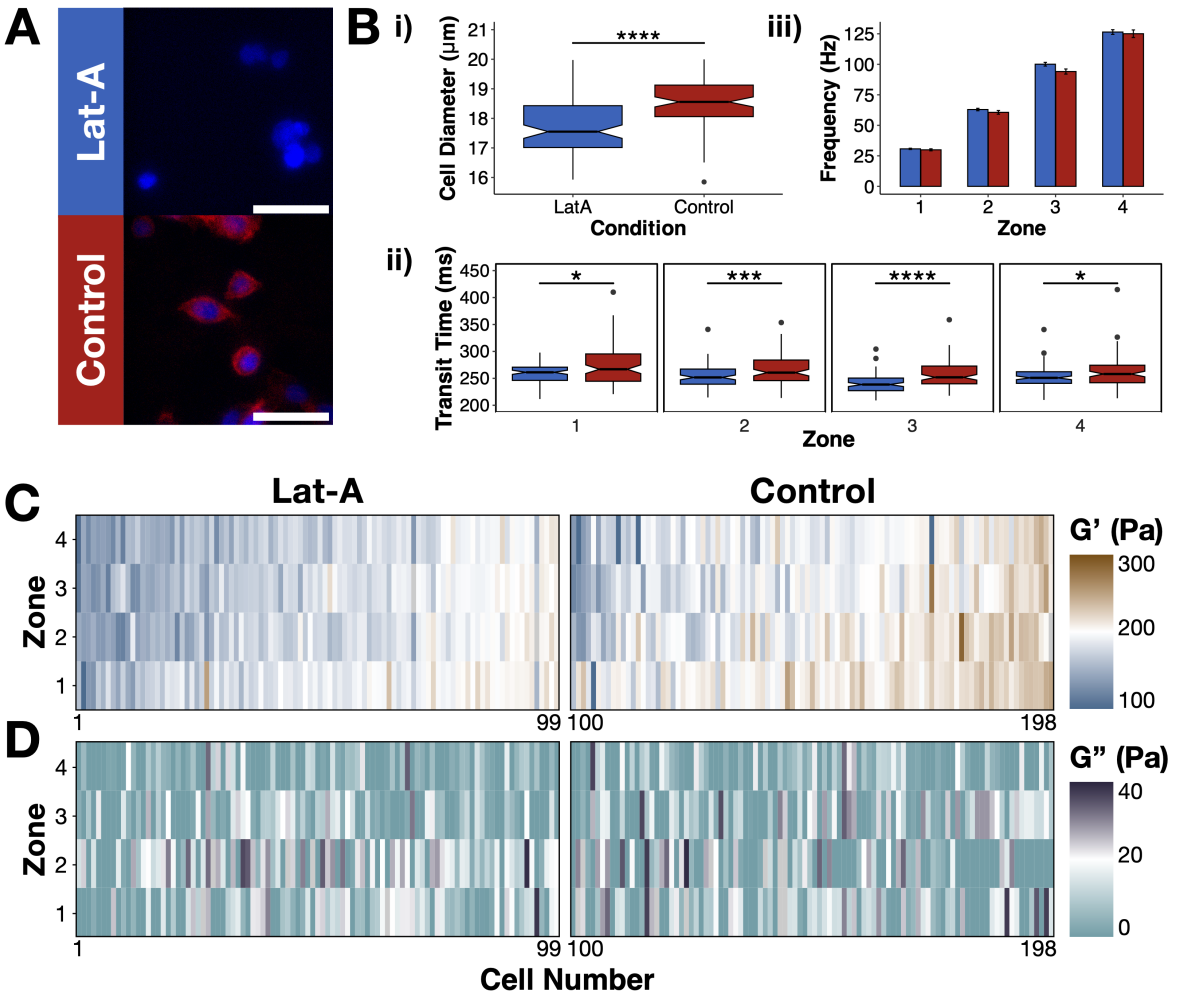


Figure 4.4: mz-visco-NPS Detects Actin Filament Perturbations in MCF-7 Cells. (A) Fluorescent images of Latrunculin-A (Lat-A)-treated (top) and untreated control) (bottom) MCF-7 cells. 4',6-diamidino-2-phenylindole (DAPI, blue) and rhodamine phalloidin (red) were used to stain the nucleus and actin filaments, respectively. Because Lat-A disrupts actin filaments, rhodamine phalloidin is not visible in the Lat-A treated cells. Scale bar = 50 µm. (B) Treated (blue) and untreated (red) cells were measured in a 4-zone mz-visco-NPS device (shown in Figure 1), with Lzone = 4 mm and Lp = 500, 250, 167, 125 µm. An applied pressure of 13.8 kPa was used. The measured (i) cell diameter, (ii) cell transit time through each zone, and (iii) applied deformation frequency. (C) Heatmap of the measured storage modulus (G') for each single cell in each zone, grouped by Lat-A-treatment and untreated control conditions. Each column is a single cell. (D) Heatmap of the measured loss modulus (G") for each single cell in each zone, grouped by Lat-A-treatment and untreated control conditions. Each column is a single cell.

Lat-A treated cells n = 99; Untreated control cells n = 99 cells. Error bars in (B, iii) correspond to standard error. ns, not significant, * $p \leq 0.05$, ** $p \leq 0.01$, *** $p \leq 0.001$, and **** $p \leq 0.0001$. Notches in the boxplots (B, i and ii) represent the 95% confidence interval of the median.

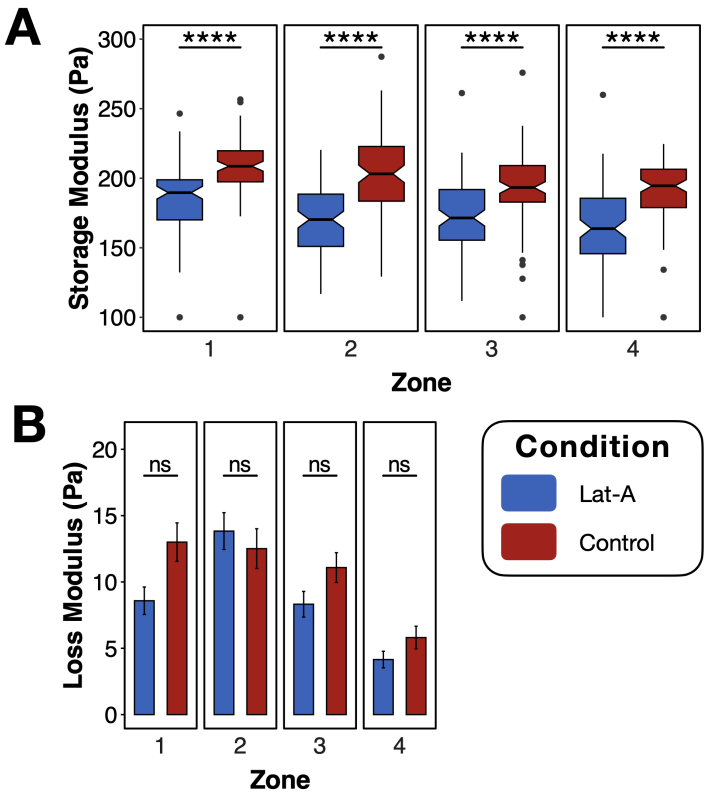


Figure 4.5: Supplemental Data on Population Averages of Viscoelastic Properties for MCF-7 Cells Treated with Latrunculin-A (Lat-A). (A) The measured average storage modulus and (B) average loss modulus of untreated control and Lat-A MCF-7 cells measured in each zone with an average applied frequency as detailed in Figure 2 (B, iii). As expected, Lat-A treated cells have a reduced average storage modulus as compared to that of untreated control cells.
Lat-A treated cells n = 99; Control cells n = 99. Error bars in (B) correspond to standard error. ns, not significant, * $p \leq 0.05$, ** $p \leq 0.01$, *** $p \leq 0.001$, and **** $p \leq 0.0001$. Notches in the boxplots represent the 95% confidence interval of the median.

When examining the viscoelasticity of Lat-A-treated and control cell populations with respect to average strain frequency, we did not observe the widely reported power-law increase in elastic G' and viscous G" with respect to increasing frequencies [116, 181, 203]. One possible explanation is that a power-law relationship does not always accurately describe cell behavior at low frequencies [106, 204, 205], such as those achieved in our experiments. Additionally, such power-law relationships are typically only observed over a frequency range that spans multiple orders of magnitude [206]. In our experiments, the frequency range spanned less than one order of magnitude. Overall, we consistently observed that cells became less elastic (i.e. showed decreasing elastic G') with increasing frequency for both Lat-A and untreated control cells in the limited frequency range we measured **(Figure 4.5A)**. To

determine whether this behavior is the result of our unique device implementation or design, we assessed the effect of multiple microfluidic geometries on single-cell viscoelasticity.

4.5.2 Evaluating the Effect of Zone Arrangements on mz-visco-NPS Measurements

Because cells are nonlinear materials [141], the frequency order in which they are perturbed can affect their viscoelastic measurements. Thus, we fabricated multiple devices with different zone arrangements and measured MCF-7 cells to determine the effect of perturbation order and measurement duration.

To confirm that perturbation order is not an influencing variable in our measurements, we designed devices in which the applied frequency ranged from low-to-high, high-to-low, or remained constant (all-low or all-high) across five zones **(Figure 4.6A and B)**. When measuring MCF-7 cells, we observed no significant differences in elastic G' based on frequency order **(Figure 4.6C i)**. Both the low-to-high and the high-to-low frequency devices showed decreasing elastic G' with respect to increasing frequency, just as in our previous experiments. Thus, perturbation order is not a significant factor in mz-visco-NPS. Measuring cells in an all-low frequency device produced a higher elastic G' than those in the all-high frequency device **(Figure 4.6C ii)**, again consistent with our observation that elastic G' decreases with increasing frequency. Notably, there was minimal zone-to-zone variance in both the "all-low" and "all-high" frequency devices, suggesting that cells were not experiencing "material fatigue" despite undergoing repeated stress.

We next determined the effect of zone length (L_{zone}), i.e. the duration cells are perturbed at a specific strain frequency, on elastic G' and viscous G". We designed a 3-zone device with increasing zone lengths of 2, 4, and 6 mm **(Figure 4.6D)**. Zone lengths greater than 6 mm was not possible to test, given that the total "footprint" of the mz-visco-NPS channel would have surpassed the physical length of the glass substrate. The transit time of cells in each zone was linearly proportional to the zone length **(Figure 4.6E i)** and the frequency of strain experienced by cells in each zone was nearly identical **(Figure 4.6E ii)**. Although viscous G" continued to increase with respect to zone length **(Figure 4.6E iv)**, elastic G' plateaued with a zone length of 6 mm **(Figure 4.6E iii)**. Thus, for the remaining results discussed below, we employed a microfluidic geometry with a 6 mm zone length.

4.5.3 Comparing the Viscoelastic Properties of Multiple Breast Epithelial Cell Types

Using a 4-zone device with a 6-mm zone length, we measured the viscoelasticity of three breast epithelial cell lines: non-malignant MCF-10A, malignant MCF-7, and invasive MDA-MB-231. We measured mean diameters of 16.3 ± 1.5 µm for MCF-10A, 18.9 ± 0.9 µm for MCF-7, and 16.5 ± 1.2 µm for MDA-MB-231 **(Figure 4.7A i)**. All cell lines took

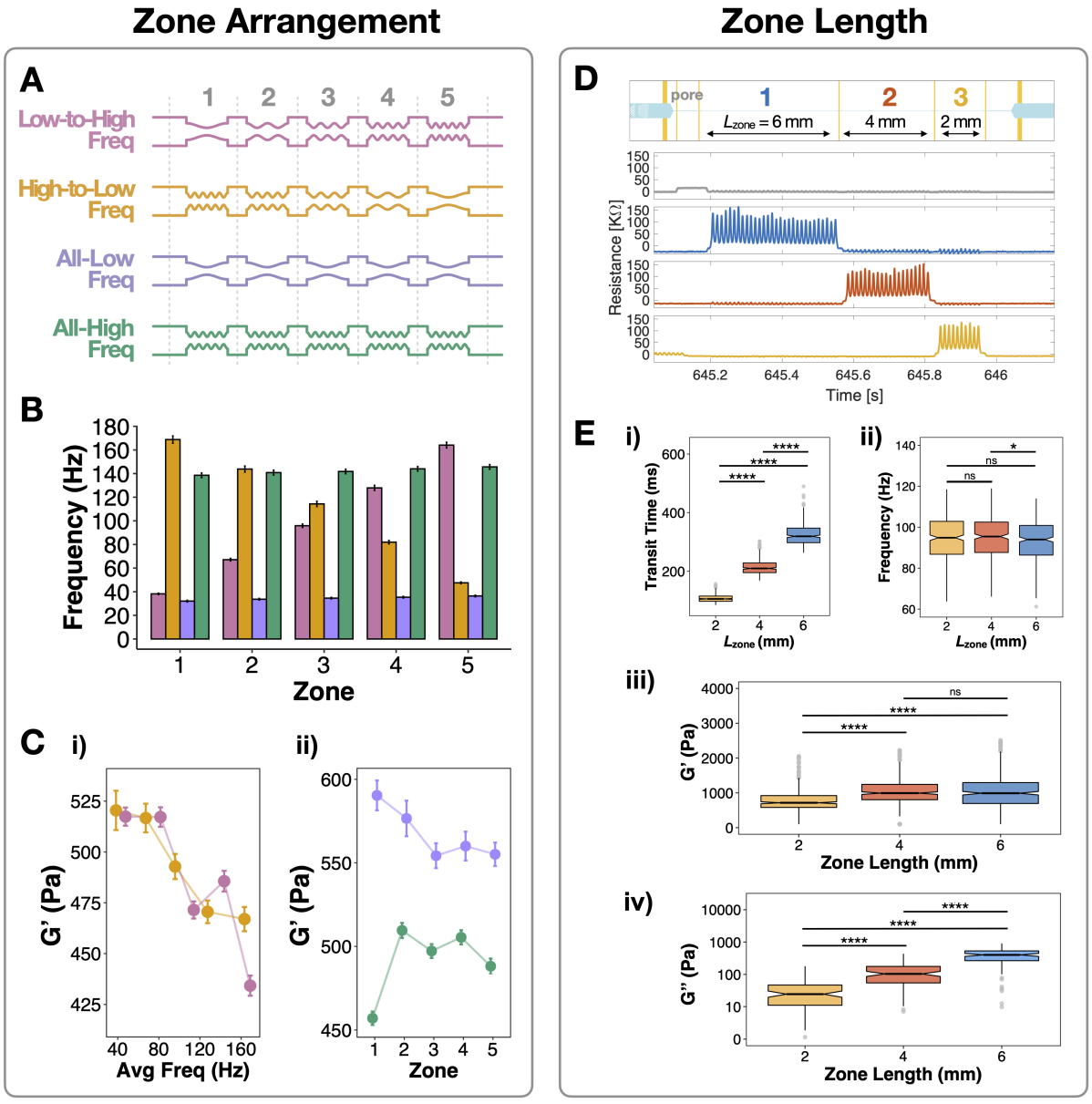


Figure 4.6: Effect of Channel Geometry on Measured Storage Modulus. (A) Four distinct channel geometries were used to test different frequency arrangements. A "Low-to-High" frequency device (pink) introduced cells to a low frequency zone first; applied frequency increases in the subsequent zones (from L_p = 500 µm to 125 µm). Vice versa, a "High-to-Low" frequency device (orange) introduced cells to a high frequency zone first; applied frequency decreases in the subsequent zones (from L_p = 125 µm to 500 µm). A third "All-Low" design had a constant low frequency across all zones (purple) (L_p = 500 µm), while a fourth "All-High" design had a constant high frequency across all the zones (green) (L_p = 500 µm). All zones had a constant zone length of L_{zone} = 2mm. (B) Measured applied strain frequency on MCF-7 cells for each of the four channel geometries used. (C) (i) Comparison of the elastic G'

Figure 4.6 (continued) modulus between the High-to-Low and Low-to-High frequency arrangement. Elastic G' modulus decrease with respect to increasing frequency. n = 118 MCF-7 cells for both the High-to-Low and Low-to-High frequency device measurements. (ii) Comparison of the elastic G' modulus between All-High and All-Low frequency arrangement. Elastic G' modulus is greater at the All-High frequency, than at the All-Low frequency. n = 136 MCF-7 cells for both All-Low and All-High frequency device measurements. (D) Schematic (top) of a 3-zone device used to evaluate the impact of zone length on rheological measurements, and a representative example of the signal pulses (bottom) acquired as a cell transits this device arrangement. The 3-zone device has a variable zone length (L_{zone}) of 2, 4, and 6 mm, where each zone has an equivalent period length of Lp = 200 µm. (E) Measured (i) transit time, (ii) applied frequency, (iii) storage modulus (G'), and (iv) loss modulus (G"), versus zone length. n = 361 MCF-7 cells were measured. Significant differences observed in the storage and loss moduli between the 2, 4 and 6 mm zones suggest that zone length is crucial to viscoelastic measurements taken with mz-visco-NPS.
Error bars in (B) and (C) correspond to standard error; some error bars are too small to be visible. ns, not significant, * $p \leq 0.05$, ** $p \leq 0.01$, *** $p \leq 0.001$, and **** $p \leq 0.0001$. Notches in the boxplots represent the 95% confidence interval of the median.

approximately 750 – 1250 ms to transit each zone, resulting in mean applied frequencies of 14, 30, 47, and 65 hz for zone 1, 2, 3, and 4, respectively, across the three cell lines **(Figure 4.7A ii)**.

All three cell lines showed broad heterogeneity. Non-malignant MCF-10As had the highest elastic G', and malignant MCF-7s had the lowest **(Figure 4.7B and Figure 4.8A)**. At the highest frequency (zone 4), MDA-MB-231's were more compliant than MCF-10A's, consistent with their invasive phenotype. These results mirror previously published studies [116, 159]. With regard to viscous G", we observed similar broad single-cell heterogeneity with a wide range of phenotypes **(Figure 4.7C and Figure 4.8B)**. Loss tangent (η) is defined as η = G"/G', where a greater η corresponds to a more viscous phenotype. The loss tangent for non-malignant MCF-10A cells ($\eta = 0.14$) was lower than that for MCF-7 cells ($\eta = 0.29$) in the highest frequency zone **(Figure 4.8C)**, indicating that the MCF-7's are more viscous. Finally, no significant frequency-dependent trends were observed: the elastic G' and viscous G" moduli for all cell types remained relatively constant in all zones. Taken together, mz-visco-NPS measures distinct single-cell elastic G' for MCF-10A's, MCF-7's, and MDA-MB-231's at frequencies from 10 – 70 hz, and distinct loss tangent (η) at the highest frequency zone (zone 4).

4.5.4 Uncovering Viscoelastic Differences Among Average and High Rick Human Mammary Epithelial Cells (HMEC)

HMECs were screened for differences in viscoelastic phenotype. Six primary HMEC strains were measured: three average-risk women, aged 33-40 years without any known breast

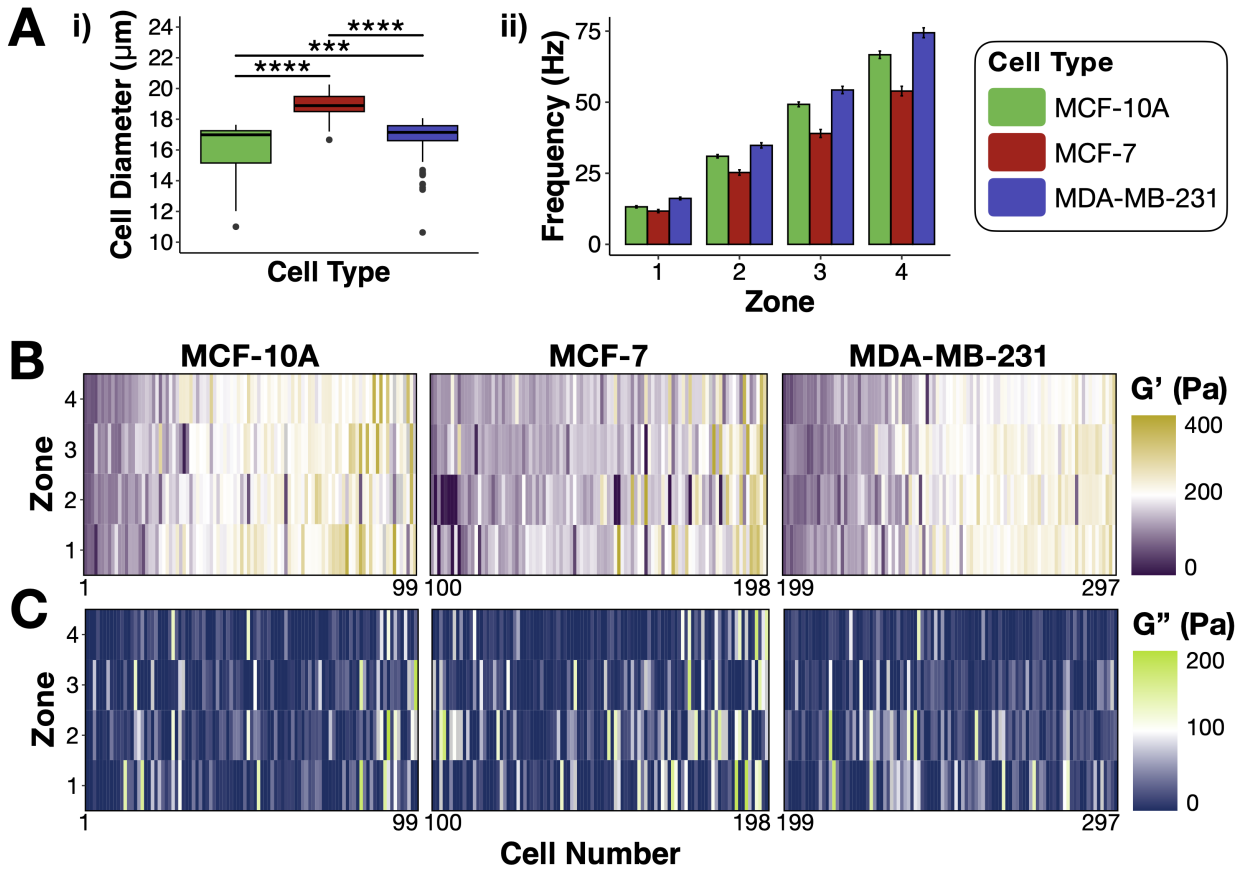


Figure 4.7: Comparison of Viscoelastic Properties Among Three Breast Epithelial Cell Lines. (A) The measured (i) cell diameter, and (ii) applied strain frequencies for MCF-10A (green), MCF-7 (red), and MDA-MB-231 (blue) cells in a 4-zone device, with Lzone = 6 mm, and Lp = 500 to 125 µm. (B) Heatmap of the measured storage modulus (G') for each single cell in each zone, grouped by cell type. Each column is a single cell. The three cell types have significantly different storage moduli, with differences most evident in zone 4. (C) Heatmap of the measured loss modulus (G") for each single cell in each zone, grouped by cell type. Each column is a single cell.
MCF-10A cells n = 99, MCF-7 cells n = 99, MDA-MB-231 cells n = 99. Error bars in (A, ii) correspond to standard error. ns, not significant, * $p \leq 0.05$, ** $p \leq 0.01$, *** $p \leq 0.001$, and **** $p \leq 0.0001$.

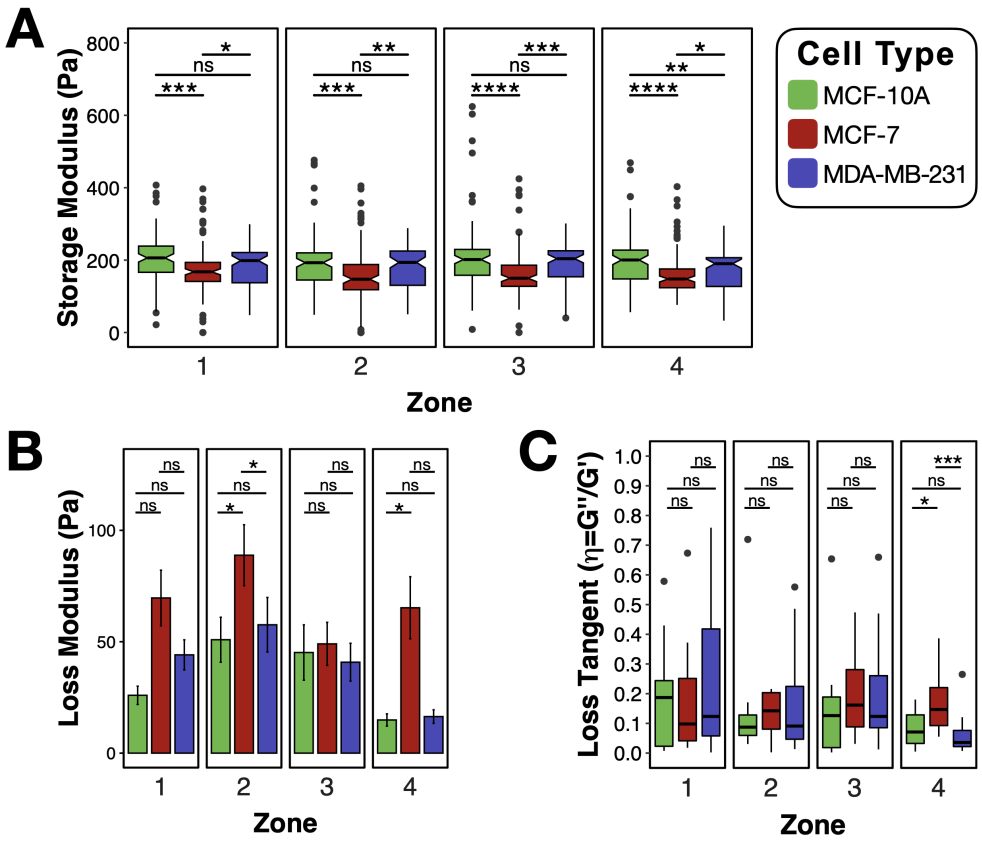


Figure 4.8: Supplemental Data on Population Averages of Viscoelastic Properties for 3 Breast Epithelial Cell Types. (A) The measured average storage modulus (G') and (B) average loss modulus (G") of MCF-10A, MCF-7, and MDA-MB-231 cells, measured in each zone with an average applied frequency detailed in Figure 4 (A ii). MCF-10A cells have a greater average storage modulus than MCF-7 cells, as expected. MDA-MB-231 cells have an average storage modulus between those of MCF-10A and MCF-7 cells, as expected. (C) The measured loss tangent, defined as η=G"/G', for MCF-10A, MCF-7, and MDA-MB-231 cells, measured in each zone. In the highest frequency zone (Zone 4, avg freq. = 65 hz), mz-visco-NPS measures a significantly different loss tangent between non-malignant MCF-10A cells and malignant MCF-7 epithelial cells.
MCF-10A cells n = 99, MCF-7 cells n = 99, MDA-MB-231 cells n = 99. Error bars in (B) correspond to standard error. ns, not significant, * $p \leq 0.05$, ** $p \leq 0.01$, *** $p \leq 0.001$, and **** $p \leq 0.0001$. Notches in the boxplots represent the 95% confidence interval of the median.

cancer-causing germline mutations, and three high-risk women, aged 24-35 years, with BRCA1 germline mutations (Table 4.3). These were normal, finite lifespan HMEC, not cancer cell lines or tumor cells. We, again, employed a 4-zone device with $L_{zone} = 6$ mm. Average-risk HMECs had larger single-cell diameters than those of high-risk HMECs, 16.3 $\pm$ 1.0 µm and 16.0 $\pm$ 0.9 µm, respectively **(Figure 4.9A i)**. All HMECs were perturbed at similar frequencies, ranging between 15 to 71 hz **(Figure 4.9A ii)**. We observed broad heterogeneity of the elastic G' moduli at the single cell level for both risk groups **(Figure 4.9B and Figure 4.10B)**. High-risk cells had a 10% lower elastic G' than that of the average-risk cells, indicating a more compliant phenotype **(Figure 4.10A)**. No similar single-cell and population-level differences were observed with the viscous G" measurements **(Figure 4.9B and Figure 4.10)**. To quantify heterogeneity, we examined the unit variance in storage and loss moduli, respectively, between the 4 measured frequency zones for each single cell **(Figure 4.9B and C)**. We did not observe more within-cell viscoelastic heterogeneity between the high risk and average risk cells.

4.5.5 Discussion

We report an all-electronics-based, microfluidic platform—multi-zone visco-NPS (mz-visco-NPS)—that enables true single-cell viscoelastic measurements. mz-visco-NPS uniquely employs multiple sinusoidal contraction zones, each with a periodically changing width and frequency, to measure the frequency-dependent elastic G' and viscous G" response of single cells. Compared to the gold standard AFM [116, 174], and newer methods such as hydrodynamic stretching [128], mz-visco-NPS has a moderate-throughput rate of up to 600 cells/hr, obviates the need to consider substrate stiffness by measuring cells in suspension, and uses simple data acquisition hardware that does not require high-speed imaging.

The implementation presented here identifies storage and loss modulus differences among immortalized and primary cells. The storage modulus is a measurement of elasticity, while the loss modulus is a measurement of viscosity. Together, they present a physical fingerprint of the cell. A balance between cellular elasticity and viscosity is required for the healthy functioning of a cell, especially in mechanical-heavy tasks such as migration42. This physical fingerprint can inform on higher order functions, such as invasion or differentiation, and can be useful in identifying cellular states, potentially such as cell-cycle phase or tumor malignancy. With mz-visco-NPS, we characterized this physical fingerprint amongst immortalized mammary epithelial cell lines and primary human mammary epithelial cells.

We validated our mz-visco-NPS platform by demonstrating that it could measure viscoelastic changes of MCF-7 cells when their cytoskeleton was disrupted with Lat-A treatment. Unlike current rheological measurements, mz-visco-NPS allowed us to measure the high level of heterogeneity in viscoelasticity among single cells in a population. Intriguingly, we observed that a significant fraction of single cells had an elastic G' that mirrored the average G' of untreated cells, possibly indicating that these cells recovered more quickly from actin de-

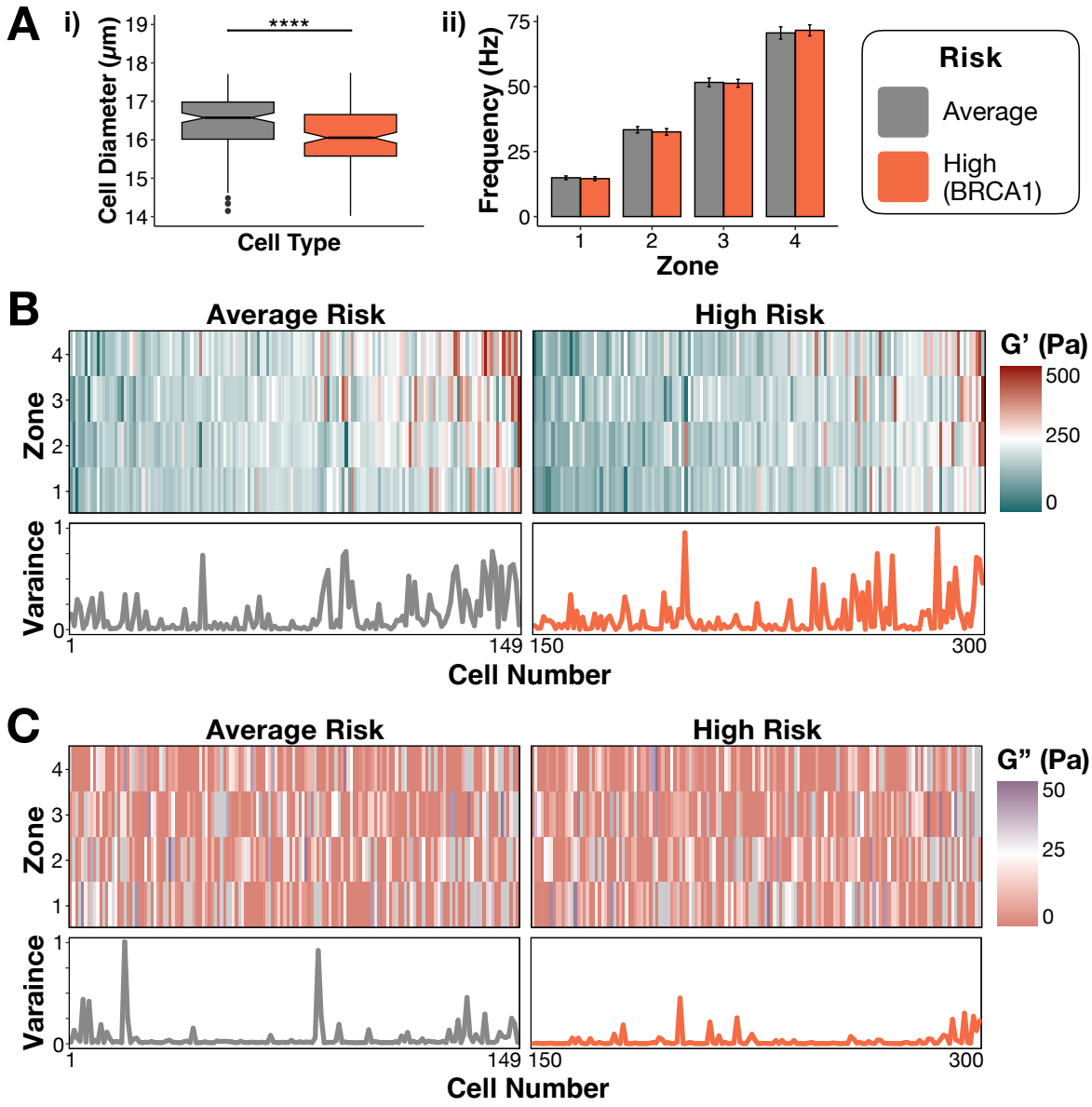


Figure 4.9: Viscoelastic Properties of Primary Human Mammary Epithelial Cells (HMECs) with the BRCA1 Mutation Have Greater Single-Cell Heterogeneity than HMECs without the Mutation. (A) The measured (i) cell diameter, and (ii) applied strain frequencies for Average-Risk (no BRCA1 mutation) HMECs (grey), and High-Risk (has BRCA1 mutation) HMECs (orange) in a 4-zone device, with Lzone = 6 mm, and Lp = 500 to 125 μm. (B) Heatmap of the measured storage modulus (G') for each single cell in each zone, grouped by risk. (C) Heatmap of the measured loss modulus (G") for each single cell in each zone, grouped by risk. The line plots below each heatmap in (B) and (C) show the unit variance of G' and G", respectively, across the 4 zones measured for each single-cell.
Average Risk HMECs n = 150, High Risk HMECs n = 150. Error bars in (A, ii) correspond to standard error. ns, not significant, * $p \leq 0.05$, ** $p \leq 0.01$, *** $p \leq 0.001$, and **** $p \leq 0.0001$. Notches in the boxplots (A, i) represent the 95% confidence interval of the median.

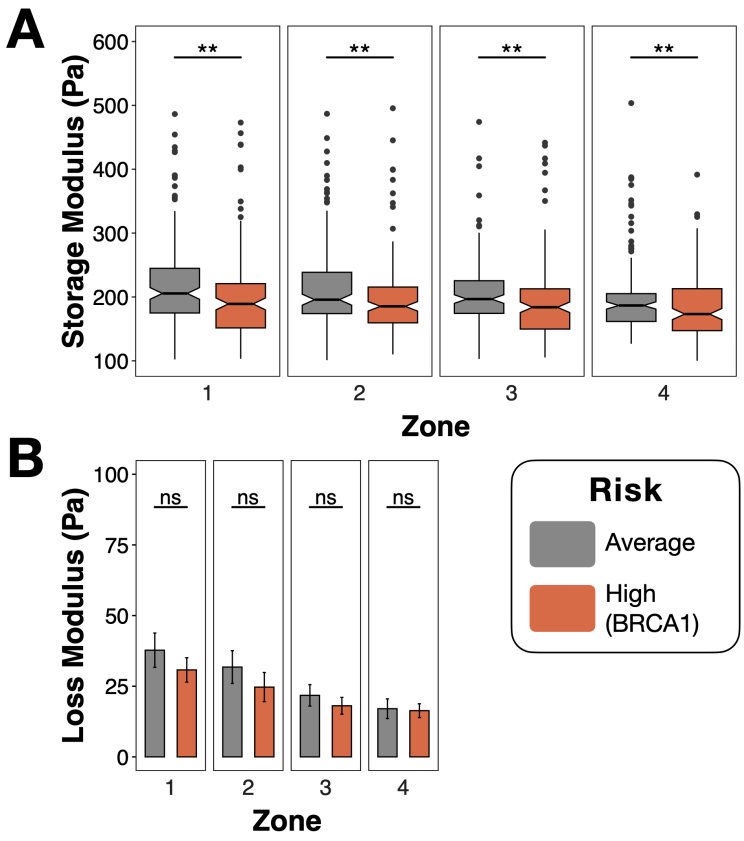


Figure 4.10: Supplemental Data on Population Averages of Viscoelastic Properties for Primary Human Mammary Epithelial Cell (HMEC) Strains. (A) The measured average storage modulus (G') and (B) average loss modulus (G") of average risk and high risk cells, measured in each zone with an average applied frequency detailed in Figure 5 (A ii). Average Risk HMECs n = 150, High Risk HMECs n = 150. Error bars in (B) correspond to standard error. ns, not significant, * $p \leq 0.05$, ** $p \leq 0.01$, *** $p \leq 0.001$, and **** $p \leq 0.0001$. Notches in the boxplots represent the 95% confidence interval of the median.

polymerization. Further studies are needed to thoroughly investigate this result. Ultimately, mz-visco-NPS's single-cell capability is advantageous in revealing heterogenous viscoelastic properties typically masked by ensemble average measurements performed by other rheological platforms.

Using mz-visco-NPS, we examined the viscoelastic properties of human mammary epithelial cells that represented the entire continuum of epithelial transformation states: from average-risk and BRCA1 mutant high-risk primary epithelial cells (not cancer), to immortal non-malignant, malignant, and metastatic cell lines. We measured differences in elastic G' among immortal non-malignant MCF-10A, malignant MCF-7, and metastatic MDA-MB-231 cell lines and differences in the loss tangent (G"/G') between MCF-10A's and MCF-7's,

particularly at the highest frequency zone, which were consistent to previous viscoelastic measurements of these cell lines at the population level [116]. Just as in our validation experiments, we identified a high level of heterogeneity within each cell line at the single cell level. When measuring the viscoelasticity measurements of average-risk and high-risk HMECs, we again observed significant heterogeneity at the single cell level. Despite this, we could determine that high-risk HMECs were more compliant than average-risk cells on the whole. While the high-risk HMECs we measured bore BRCA1 mutations, we note that Shalabi et al. [207] and Miyano et al. [208] showed that HMECs with monogenic risk factors such as mutations in BRCA1, BRCA2, or PALB2 all share a common high-risk phenotype. We thus hypothesize that so too HMECs with BRCA2 or PALB2 or even HMECs from women who are high risk but have no identifiable germline mutation may also have similar viscoelasticity as the BRCA1+ cells we measured here. Future experiments could focus on this intriguing hypothesis. The greater physical compliance of BRCA1 HMECs (as compared to average-risk HMECs) is congruent with the expected phenotype of a malignant cell. This might suggest that BRCA1 cells share underlying biomechanical properties consistent with changes that are present in cancer cells. As one example, BRCA1 deficiency has been linked to alterations in biomechanical functions such as cell division46. Future studies can further explore how viscoelastic differences manifest in high-risk cells that possess other risk factors, such as family history and age.

Limitations to mz-visco-NPS include the limited frequency range at which single cells could be measured and the duration of the applied strain in the contraction zones. These constraints were determined by the physical length of the glass substrates that we employed. Employing a serpentine channel that wraps around the entire area of the glass substrates could overcome these limitations, enabling access to a greater range of frequencies and increasing the duration of applied strain. This could potentially aid in identifying differential phenotypes in the viscous G", as higher frequencies better capture viscous behavior [209]. Furthermore, while we achieve moderate throughput of up to 600 cells/hr, sample rates can easily be further improved. Because we employ an electronic method to measure the viscoelasticity of single cells, we could readily increase throughput by having multiple devices operating in parallel with advanced signal processing to decouple simultaneous readouts [210, 211].

Overall, mz-visco-NPS is a new, electronic-based approach to single-cell viscoelastic phenotyping. Cytoskeletal reorganizations [212], disruptions in nuclear morphology [213], and even macromolecular behavior in the cytosol [214] are all reflected by a cell's viscoelasticity. Because of its versatility, throughput, and ease by which it can be employed, mz-visco-NPS could enable a broader adoption of viscoelasticity as a biomarker of a cell's state and function in health and disease.

4.6 Conclusion

In this chapter, I introduced Multi-Zone Visco-NPS (mz-visco-NPS), a microfluidic platform for multi-frequency viscoelastic phenotyping. As discussed in Chapter 1, this platform contributes to the broader objective of developing and introducing unique tools for the multimodal measurement of single-cell biophysical properties. Mz-visco-NPS measures the storage and loss moduli of cells, in addition to cell diameter, for a moderate throughput evaluation of single-cell multi-frequency rheology. Using the platform, we evaluated human breast epithelial cells, characterizing viscoelastic differences among average versus high-risk and non-malignant versus malignant cells. Beyond the results, I also thoroughly delved into the background, theory, and methodologies behind the platform. Overall, mz-visco-NPS is a valuable tool not only for single-cell viscoelastic measurements, but for the broader field of microfluidic mechanophenotyping.

Chapter 5

Combo Node-Pore Sensing (Combo-NPS): Integrated Surface Marker Screening and Mechanophenotyping

This chapter is adapted from a pre-print manuscript:
A. Lai, K. L. Cotner, M. A. LaBarge, and L. L. Sohn, "Combo-NPS: Microfluidic Platform for Multi-Modal Biophysical Phenotyping of Single Cells", In Preparation, 2024.

I introduce Combo-NPS, an analytical platform for integrated single-cell phenotyping of multiple biophysical attributes: cell diameter, whole-cell deformability, viscous recovery, and surface marker expression. Combo-NPS incorporates two unique technologies within a single microfluidic channel: DNA-directed patterning [215, 216] and NPS [1, 132, 151, 158, 159]. DNA-directed patterning enables a simple, one-step process for surface functionalization with immobilized antibodies. Likewise, NPS enables an optics-free, all-electronic measurement of the transiting cells. The platform analyzes transient antibody-antigen interactions as the cells flow over the immobilized antibodies, while a downstream mechano-NPS [132] segment measures the cell's deformability and viscous recovery. Together, surface marker and biomechanical readouts are measured, enabling a truly unique analysis on single-cells. In this chapter, I describe in further detail the approach taken, including channel design, protein labeling, surface patterning of antibodies, and experimental execution. I then review our results from measuring immortalized breast epithelial cells and primary HMEC's, showing that combo-NPS can use the paired data to assess potential correlation between cellular biomechanics and surface marker expression. Overall, Combo-NPS is a powerful microfluidic platform that sets a new standard for multimodal single-cell biophysical phenotyping.

5.1 Prior Work and Motivation

Advances in sequencing have enabled "multi-omic" techniques, which refer to the integrated analysis of the genome, proteome, transcriptome, etc [101]. In a similar manner, Combo-NPS enables an entirely new paradigm I term "multi-phenome", in which multiple biophysical traits can be measured simultaneously. Combo-NPS is an analytical platform that enables a single-cell multi-phenome measurement by integrating the interrogation of multiple biophysical attributes into a single microfluidic chip in a label-free, optics-free, moderate-throughput approach [210]. While section 2.3 reviewed the importance of single-cell biomechanical phenotyping, here I describe the relevance and significance of surface marker screening. Additionally, I highlight previous approaches that integrated transient surface marker screening using NPS.

5.1.1 Significance of Surface Markers

Cell surface markers are special proteins expressed on the surface of cells. The most common cell surface markers are clusters of differentiation (CD) antigens. CD antigens serve as molecular fingerprints, aiding in the identification and classification of cells. CD proteins also serve as receptors or ligands for tasks such as cell signaling or cell adhesion [217–219]. An example of the significance of cell surface markers for cell classification is with T cells. T cells are lymphocytes subdivided into 2 distinct types, each with vastly different functions: helper T cells and killer T cells. These subtypes are identified using CD antigens, namely CD4 for helper T cells and CD8 for killer T cells **(Figure 5.1A)**. Overall, surface membrane proteins are straightforward signatures for identifying not only T cells, but any complex cell population or sub-population [220–222].

Surface markers also play a critical role in how cells sense and respond to their surroundings. Cell adhesion molecules (CAMs) such as integrins and cadherins in particular are critical structures that play a crucial role in transmitting mechanical forces between the cellular cytoskeleton and the extracellular matrix **(Figure 5.1B)** [223]. Integrins in particular are heterodimeric transmembrane receptors that help in the formation of focal adhesions. They facilitate how epithelial cells sense and respond to the environment and external stimuli, and mediate cell-cell and cell-ECM interactions. Furthermore, they facilitate the transduction of forces across the cell membrane, and coordinate the development of the adhesome, an internal network of structural and signaling proteins that broadly influence cell behavior [224, 225]. Theses adhesomes between cells and the extracellular matrix impact cellular mechanobiology and ultimately cellular behavior [226], including processes from embryonic development to inflammation [227, 228]. The relationship between surface adhesion proteins and cellular mechanobiology has been well documented [229–233]. In contrast, there is an absence of studies that focus on how protein surface expression can affect whole-cell biomechanics. Combo-NPS is a tool that can directly address this application, creating a new avenue of exploration that correlates the surface proteome with mechanobiology and biomechanics.

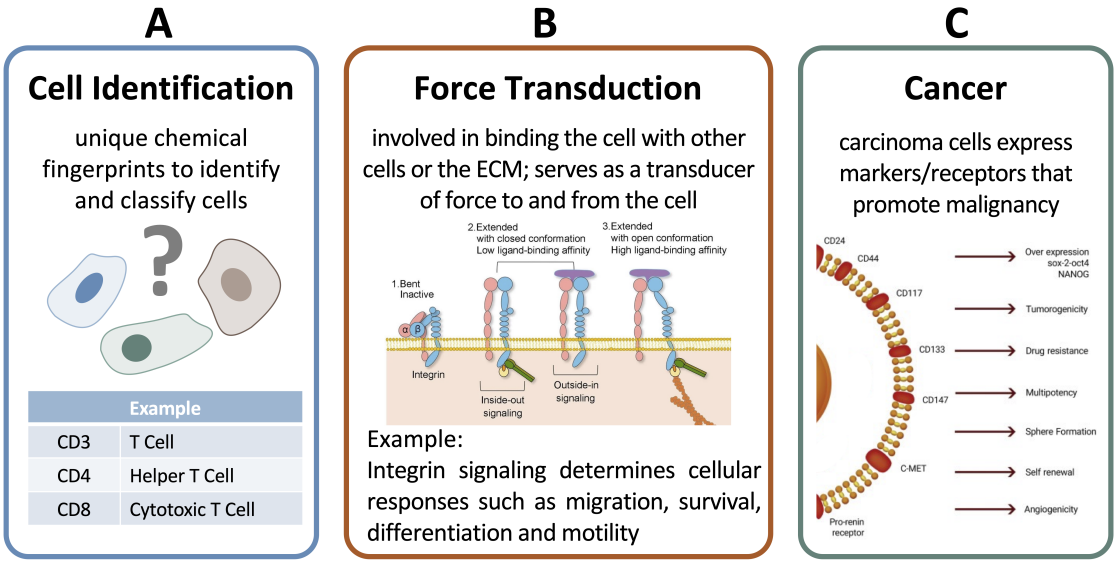


Figure 5.1: Examples of the Significance of Surface Markers. Cell surface markers are any set of proteins expressed at the cell membrane. These markers are useful in both research and medicine. (A) Cell surface markers are commonly used for cell identification. For example, CD3, CD4, and CD8 are common markers used to diffentiate T-cells. (B) Surface proteins play a critical role in how cells sense and respond to force. Integrin signaling ties directly into the cellular cytoskeleton, impacting migration, survival, differentiation, and motility. (C) Surface markers play a role in both health and disease: carcinoma cells can up-regulate or down-regulate expression of surface proteins to promote malignancy. Images adapted from [223] and [236].

Finally, surface markers hold immense potential in drug discovery and medicine. From a clinical perspective, immunophenotyping of cells can aid in both diagnostics and treatment. In cancer, the progression towards malignancy often results in numerous hallmark changes, including a shift in the surface proteome **(Figure 5.1C)**. Multiple surface antigens, ranging from CD34 to CD44, have been identified as cancer-associated stem cell markers [234], creating new research and therapeutic targeting opportunities. Some additional examples: in the clinic today, CD33 is used to assess acute myleoid leukemia (AML), CD117 is used to diagnose cancers such as gastrointestinal tumors or mucosal melanoma, and estrogen and progesterone receptors are used to determine breast cancer treatment [235]. This is just a handful of the current surface markers used to diagnose, assess, and treat patients. Overall, surface markers are an essential part of the cell, and serve as an increasingly important aspect in both biomedical research and clinical assays. Combo-NPS furthers the applications of surface markers by being the first microfluidic device capable of measuring surface marker and mechanophenotype simultaneously.

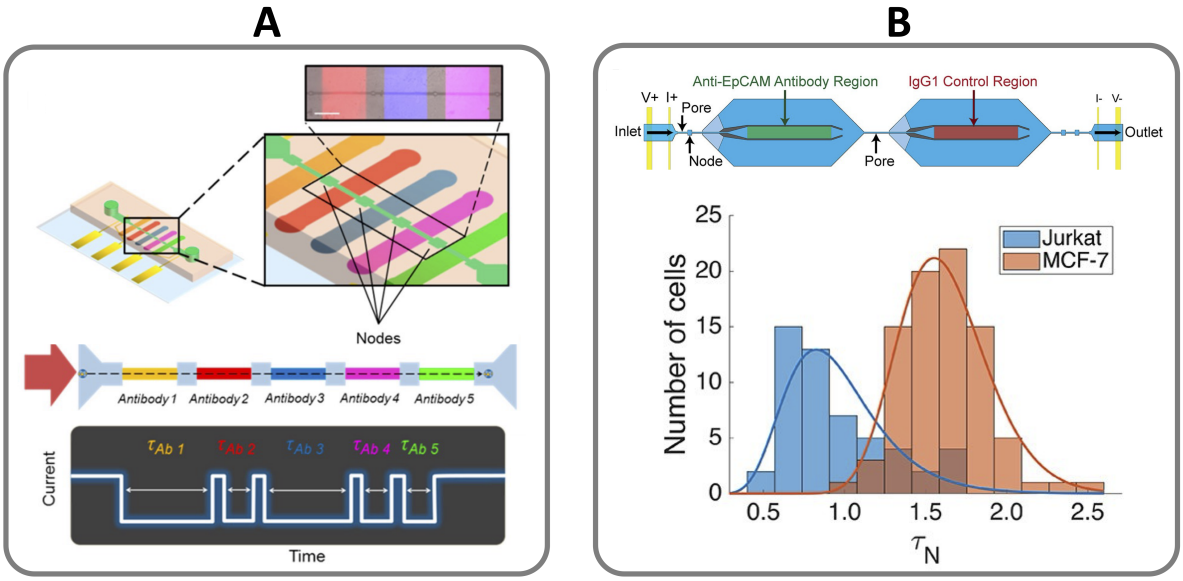


Figure 5.2: Examples of Previous Approaches Using NPS to Screen Surface Markers. Previous work have utilized the NPS architecture to screen for cellular surface markers. Like Combo-NPS, these devices used surface-immobilized antibodies to measure transient antibody-anitgen interaction during flow. (A) Balakrishnan et. al. used an NPS device to screen acute promyelocytic leukemia cells (NB4 and AP-1060) for myeloid antigens, CD13, CD14, CD15, and CD33. In this approach, temporary channels perpendicular to the main fluidic channel are used to spatially pattern antibodies [158]. (B) Kosminsky et. al used an NPS device to screen MCF-7 and Jurkat cells for EpCAM surface-marker expression. In this approach, DNA-directed patterning was used to spatially pattern antibodies. Additionally, a multi-height channel geometry was employed to better modulate flow rates [216]. This figure is adapted from [158] and [216].

5.1.2 NPS with Surface Immobilized Antibodies

Using NPS for surface-marker screening enables a unique methodology of analyzing cells in a label-free manner, without complex imaging set-ups used in a typical fluorescent immunophenotyping assay. Here, I highlight two previously published approaches.

Balakrishnan et. al. used a simple NPS device to measure human APL cells, NB4 and AP-1060 [158]. They also used the approach to distinguish between a heterogeneous mixture containing AP-1060 and NALM-1 cells. Different antibodies were patterned along a channel segmented by nodes, including myeloid antigens CD13, CD14, CD15, CD33, and control IgG **(Figure 5.2A)**. To perform the patterning, temporary channels perpendicular to the main channel were used to incubate an antibody solution containing including APTES and sulfo-EGS, immobilizing the antibodies onto the glass surface. The temporary channels were then removed and cells were flowed through the main channel, temporarily interacting with

the surface antibodies. Transit time measurements were used to characterize surface marker expression, with slower cells positively expressing the target antigen. The following Section 5.2 further elaborates on this approach.

In a more recent iteration, Kozminsky et. al. measured human MCF-7 and Jurkat cells based on EpCAM surface-marker expression [216]. Additionally, MCF10A and Hs 578T cells were screened based on epithelial-to-mesenchymal transition (EMT) surface markers: E-cadherin, N-cadherin, and β-integrin. In this implementation, the antibodies were spatially immobilized using DNA-directed patterning [215], an approach that uses oligo-labeled antibodies directed toward a complimentary strand pre-patterned on the glass surface. This vastly simplifies surface functionalization, negating the need for any auxiliary flow schemes like temporary channels. Furthermore, in this design, the antibody region is enclosed by a two-height flow expansion region, allowing the transiting cells too have an increased interaction time with the surface antibodies, improving measurement quality. As in the approach by Balakrishnan et. al. [158], the transit time of passing cells were used to characterize their surface marker expression.

Combo-NPS builds upon this previous work by incorporating a mechano-NPS [132] (see section 3.2.1 segment down-stream of the antibody screening region. Similar to Kozminsky et. al. [216], DNA-directed patterning [215] is used to functionalize the surface, while a series of multi-zone electrodes measured the cell transit behavior. The following section further details this new approach and how it works.

5.2 Approach and How It Works

Combo-NPS consists of a single microfluidic channel, subdivided into 5 regions of interest, and further segmented by 6 electrode measurement zones. **Figure 5.3A** is a schematic of the channel design, with the gold perpendicular segments representing electrodes. Pressure-driven flow moves a cell from the inlet (left) toward the outlet (right). The device itself consists of a PDMS microfluidic channel bonded to a glass slide with Ti/Pt/Au electrodes and pre-patterned DNA oligos **(Figure 5.3B)** (see Section 5.5 for fabrication methods).

As a cell transits the channel, it first passes through two expansion regions containing surface-immobilized antibodies. The antibodies are spatially positioned within the microfluidic channel using DNA-directed patterning prior to the introduction of cells (see Section 5.5). Cells expressing the antigen of interest transiently interact with the surface-immobilized antibodies, moderating the cell's transit velocity [158, 216]. The incorporation of two antibody regions enables the readout of two antigens of interest, with one region serving as a negative control. In this manner, antigen surface-marker expression is measured as a relative quantity of a cell's transit time in one region versus that in the second region. Cell transit time is determined with three electrode measurement zones flanking each antibody region. A pulse in Zone 1 signifies the entrance of a cell into antibody region 1; a pulse in Zone 2 signifies

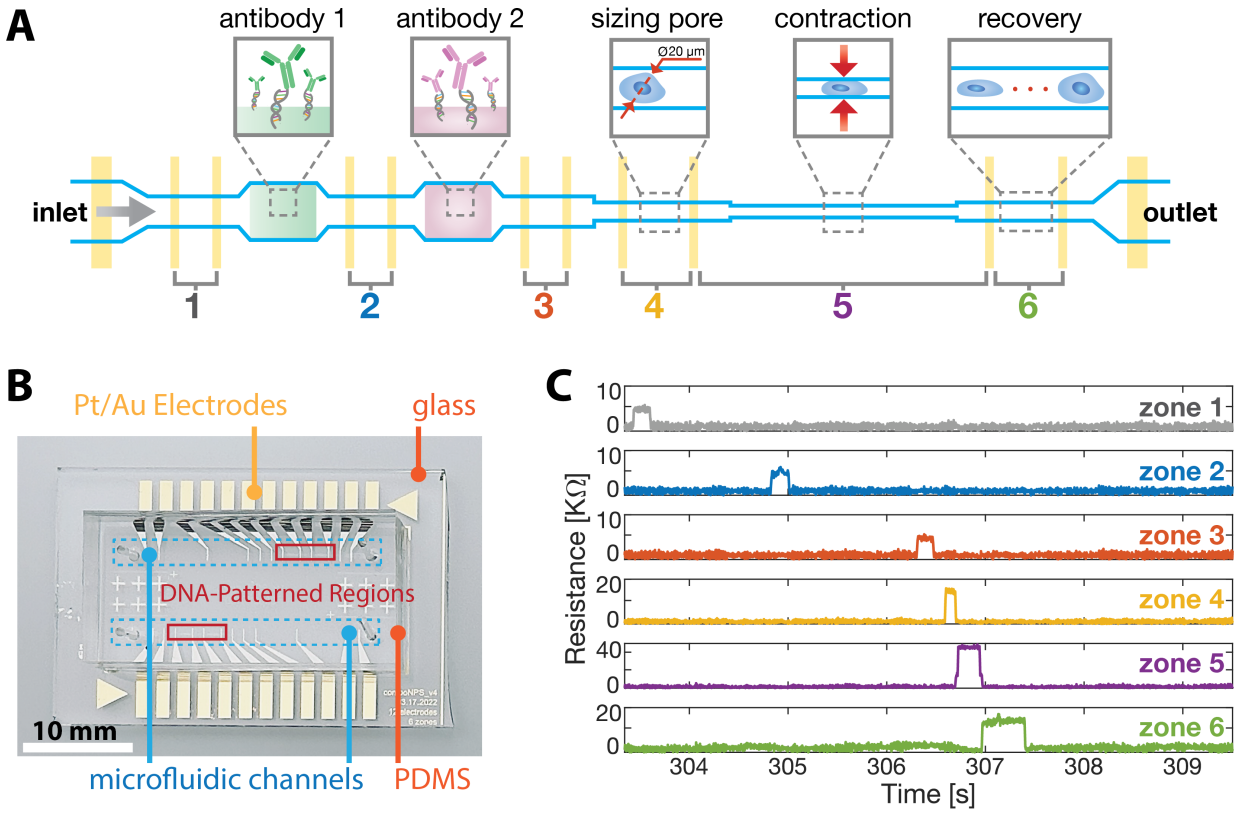


Figure 5.3: Combo-NPS Platform Overview. (A) Schematic of the Combo-NPS microfluidic channel geometry, with 5 distinct regions: 2 surface-immobilized antibody expansion regions for surface marker screening, followed by three mechanophenotping regions–a sizing pore, contraction channel, and recovery channel. Two outer electrodes apply a constant DC voltage across the channel. Among the 5 distinct regions are 6 electrode pair measurement zones that independently measure differential voltage. (B) Image of a Combo-NPS device. The device consists of a PDMS channel bonded to a glass substrate with Ti/Pt/Au electrodes and pre-patterned DNA oligos. (C) Representative resistance pulses during a cell transit event across all 6 measurement zones. The signals are aligned in time; resistive pulses cascade (starting from zone 1, to zone 2, zone 3 etc.) as the cell transits the microfluidic channel. The pulses are used to evaluate cellular biophysical properties, including surface-marker expression and whole-cell deformability.

the exit of a cell from antibody region 1, and it's entrance into antibody region 2; finally, a pulse in Zone 3 signifies the exit of a cell from antibody region 2 **(Figure 5.3C)**.

Downstream of the antibody regions are three additional regions for single-cell mechanophenotyping. The cell enters a sizing pore (Zone 4), where the channel diameter is larger than the cell diameter (see Section 3.1.1 and Equation 3.2). In this zone, the resistance-pulse magnitude is used to calculate cell diameter. Following this, the cell enters a contraction channel (Zone 5), where 45-50% strain is applied on the cell. The transit time of the cell in the contraction channel is used to measured its relative deformability, or wCDI (see Section 3.2.1 and Equation 3.3). Finally, the cell enters a recovery segment, equal in width to the sizing pore. Here, the cell's recovery from deformation is reflected by the recovery in resistance pulse magnitude.

The total length of the Combo-NPS microfluidic channel is 18 mm. Cells transit this length in approximately 3 to 5 seconds **(Figure 5.3C)**. For each cell, the measurement readout includes: normalized transit time (transit time in antibody region 1 divided by transit time in antibody region 2), cell diameter, wCDI and recovery time. Overall, Combo-NPS is a moderate-throughput platform, capable of measuring multiple biophysical properties at up to 1-10 cells/min.

5.3 Theory and Modeling

Critical to the the functionality of Combo-NPS is the interaction time between cellular surface antigens and surface-immobilized antibodies. Antibody binding kinetics can be affected by factors including temperature, concentration, and interaction time [237, 238].

At higher temperatures, more energy is present in the system, accelerating interactions between ligands and targets. Encarnação et. al investigated the equilibrium time between pertuzumab and it's specific receptor, human epidermal growth factor receptor 2 (HER2), in human SKOV3 ovarian cancer cell line [238]. They found that, between 37°C and 15 °C, differences in association/dissociation equilibrium was approximately 2 hours [238]. However, binding kinetics at room temperature versus that at physiological temperatures of 37°C remained less than an order of magnitude different. Since keeping the microfluidic chip at 37°C would be impractical , Combo-NPS experimental runs were executed at room temperature (21°C) in order to balance antibody-antigen interaction kinetics with hardware complexity.

Surface-antibody concentration also affects antibody-antigen interactions. A significant advantage of using DNA-directed patterning is the tunability of surface oligo concentration. Scheideler et. al. characterized the saturation point of drop-cased surface oligos [215]. For Combo-NPS, a fully saturated surface oligo concentration of 20 μM was used [215]. This maximizes the concentration of surface oligos, thereby maximizing the surface concentration of immobilize antibodies.

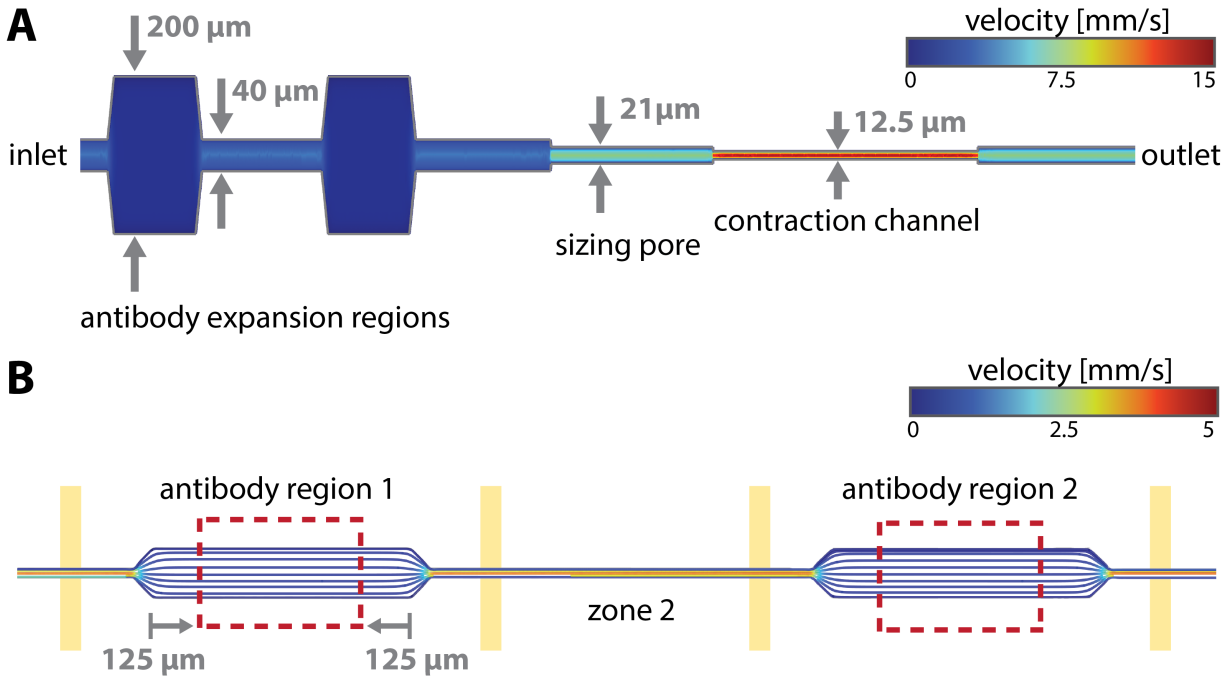


Figure 5.4: Computational Fluid Dynamics (CFD) Simulation of Combo-NPS Fluidic Geometry. (A) Fluidic velocities across a full-length Combo-NPS channel at 100 mBar of pressure-driven flow. Not to scale, the vertical axis has been anisotropically elongated for visualization purposes. The narrow contraction channel serves as a fluidic resistor, allowing the flow in the antibody expansion regions to slow. (B) Laminar flow streamlines in antibody expansion regions at 100 mBar of pressure-driven flow. The streamline colors indicate velocity. Also indicated here is the spatial positioning of the surface-immobilized antibody functionalization (dotted-red line). The surface-immobilized antibodies are inset from the expansion region inlet and outlet, allowing the fluid streamlines to parallelize and reach equilibrium fluid velocity. Simulations were performed by COMSOL Multiphysics® software [17].

The final tunable parameter critical for antibody-antigen binding kinetics is interaction time. Because combo-NPS measures transient interactions between immobilized antibody cell surface antigens, the time cells spend across a patterned antibody region can potentially influence measurement sensitivity. To ascertain the time cells will spend in the antibody regions, computational fluid dynamic (CFD) simulations were used to calculate fluid velocities across the combo-NPS region.

First, the antibody regions are expanded laterally to form wider regions of slow laminar flow. Under constant, pressure-drive flow, fluid velocity is proportional to the channel's hydrodynamic resistance (see Equation 2.3). In general, regions with a larger cross-sectional area will have a slower fluid velocity than regions with smaller cross-sectional areas. In Combo-NPS, the expansion regions are 5 times wider than the surrounding zones, rising to a final width of 200 μm from a width of 40 μm in zones 1,2 and 3. This approximately

translates into a 5 times decrease in fluid velocity along the center streamline **(Figure 5.4A)**.

Furthermore, the narrow, downstream contraction channel used for mechanophenotyping measurements serve as a built-in fluidic resistor, further slowing up-stream flow rates. The fluidic resistance of the contraction channel is almost 100 times larger than that of the antibody expansion regions, 7×10^{17} and 8×10^{15} $(Pa \times s/m^3)$, respectively **(Figure 5.4A)**. Together, the larger cross-sectional area of the antibody expansion region and the increased fluidic resistance at the downstream contraction channel allow cells to maintain an interaction time of 1.4 seconds in each antibody expansion region, given an inlet pressure of 100 mBar.

Another critical aspect of antibody interaction is streamline path lengths. Under laminar flow conditions, the fluidic streamlines are distinct and predictable. Using the same CFD model, the streamlines across the antibody expansion regions and the surrounding zones were calculated **(Figure 5.4B)**. From the entrance to the exit of the expansion region, fluid streamlines at the outer edge (along the channel geometry boundary) are 5.6% longer than the center streamline. Therefore, cells traveling along the edge will traverse a longer path. This creates an antibody-antigen interaction bias for cells traveling along different streamlines. Therefore, the antibody functionalized region is inset 125 μm, where the streamlines parallelize. In this center section, streamline lengths and fluid velocities are equivalent **(Figure 5.4B)**.

Overall, computation fluid dynamic simulations help optimize and validate the combo-NPS fluidic geometries. The channel geometry takes advantage of laminar flow streamlines and increased fluidic resistances in the contraction region for cell-antibody interaction times of up to 1.4 seconds at 100 mBar of inlet pressure.

5.4 Antibody Labeling and Surface Functionalization

As previously discussed in Section 5.2, Combo-NPS uses DNA-directed patterning [215, 216] to functionalize the glass surface of the microfluidic channel with immobilized antibodies. Critically, by using DNA-directed patterning, multiple antibodies can be spatially patterned along the channel surface in a single flow ste [216]. Unlike other approaches that use temporary flow channels [158] or auxiliary flow schemes [239], Combo-NPS uses a singular main channel for both surface functionalization and cell measurement, vastly reducing platform complexity. In DNA-directed patterning, oligos are spatially pre-patterned on the glass surface within each microfluidic antibody expansion region. Antibodies, labeled with complimentary oligo strands, are subsequently flowed through the channels. The oligos bound to the antibodies hybridize to patterned complementary oligo, completing the surface functionalization with immobilized antibodies. The following subsections further detail the specific methods behind this approach.

5.4.1 Protein Labeling Approaches

Antibodies used for Combo-NPS need to be crosslinked with DNA oligos. Table 5.1 lists the specific oligo sequences used, along with 5' and 3' end modifications. The 5' ends are modified with an Azide (N_3) group, to enable copper-free click-chemistry reactions between the oligo and respective crosslinker [215]. The 3' ends are modified with fluorescent moieties, to enable post-patterning visualization and confirmation of successful antibody immobilization in the microfluidic channel.

Table 5.1: DNA Oligo Sequences For Antibody Labeling.

Name	Full Sequence (5'→3') with End Modifications
A'	/5AzideN/CAG TCA GTC AGT CAG TCA GT/3Cy5Sp/
G'	/5AzideN/CTC TCT CTC TCT CTC TGG CT/3Cy3Sp/

Three crosslinker biochemistries were considered. The first approach, used by Kozminsky et. al. in [216], utilized a $DBCO - PEG_5 - NHS$ crosslinker **(Figure 5.5A)**. The NHS (N-hydroxysuccinimide) reacts with free amine groups along the antibody, thereby adding a functional DBCO (dibenzocyclooctyne) group to the antibody. The DBCO group is then reacted with a 20-bp oligonucleotide in a strain-promoted alkyne-azide cycloaddition copper-free click-chemistry step. This approach is a simple, 2-step reaction, using inexpensive crosslinkers and standard, unmodified antibodies. However, the chemistry is not site-specific. The crosslinker and DNA oligo are able to bind non-specifically at any free and accessible amino site within the antibody. This results in 1) the potential blocking of the antigen binding site (FAB region) by the oligo, 2) heterogeneous labeling of the antibodies, and 3) the possibility for improperly oriented antibodies when immobilized along the channel surface.

An alternative conjugation chemistry was considered using avidin-biotin interaction [210]. The same $DBCO - PEG_5 - NHS$ crosslinker as in the previously described approach is used **(Figure 5.5B)**. In this case, the NHS ester on the crosslinker targets free amine groups along an intermediary neutravidin protein. The oligo-neutravidin conjugate is then allowed to react with biotinylated antibodies, completing the oligo-antibody conjugation. In this approach, site specificity is accomplished by using commercially available biotinylated Abs that place the biotin group far from the antigen-binding domain. However, this approach increases complexity, requiring three reaction steps instead of two, and requiring the use of more expensive biotinylated antibodies.

The final conjugation chemistry considered uses a site-specific crosslinker, produced commercially as oYo-Link by AlphaThera **(Figure 5.5C)**. oYo-Link uses a proprietary light activated adapter protein that can covalently and site-specifically label the Fc region of nearly any antibody [240, 241]. Using this approach, oYo-link can serve as a site-specific crosslinker, enabling a simple, two-step, oligo-antibody labeling process. Furthermore, unlike

the avidin-biotin approach, this process maintains specificity without the need for specially modified antibodies, and without the need for additional reaction steps.

The third approach using a proprietary oYo-Link crosslinker was selected for Combo-NPS, enabling simple, site-specific conjugations. Table 5.2 details the specific antibodies, oYo-Link crosslinker variant, and oligo strands used.

Table 5.2: Combo-NPS Specific Antibody-Crosslinker-Oligo Conjugations.

Antibody	oYo-Link Crosslinker Variant	Oligo Strand
Mouse IgG1 Isotype Control	mIgG1	G'
Human EpCAM (CD326)	mIgG1	A'
Human E-Cadherin	Regular	A'
Human Mucin1	mIgG1	G'
Human CD133	Regular	G'
Human CD271	mIgG1	A'

The experimental process is as follows: The dried oYo-Link is centrifuged and reconstituted in 100 μL of molecular grade biology water (mg Water). Following reconstitution, the DBCO group loses reactivity over time due to oxidation; thus, it is stored at -20°C for immediate use (¡ 1-2 days) and 80°C for longer timespans. Freeze-thaw cycles are limited to less than 5. The reconstituted oYo-Link crosslinker is vortexed and mixed with azide-terminated oligo at a 1:1.1 molar ratio. The DBCO-azide click-chemistry reaction is allowed to go towards completion by incubating at 4°C for 48 to 72 hours. The reaction volume is wrapped in foil to protect the fluorescent moieties from photobleaching. After, a 1:1 mass:volume ratio of antibody:crosslinker is incubated together; i.e. 100 µg of antibody is mixed with 100 µL of the oYo-Link DBCO + oligo conjugate. The mixture is immediately placed on ice and positioned under a 365 nm ultraviolet (UV) light source and UV illuminated for 2 hours. The UV light source is approximately 3-5 cm from the sample, and the sample is held within a transparent microcentrifuge tube. The fully conjugated oligo-antibody sample is foil wrapped and stored 4°C. The next subsection details filtering approaches for purifying the final oligo-antibody conjugate.

5.4.2 Protein Purification Approaches

Protein purification is critical for the efficiency of antibody immobilization in the Combo-NPS microfluidic channel. Excess, unconjugated oligo and excess oYo-Link + oligo can out-compete fully conjugated oligo-antibody for complementary oligo binding spots on the glass surface. Thus, the final fully conjugated oligo-antibody product needs to be purified from the excess reactants. Three protein purification approaches were evaluated.

First, a centrifugal filter uses a regenerated cellulose membrane for filtering based on precise molecular weight (MW) cut-offs **(Figure 5.6A)**. Using centrifugal force, low MW com-

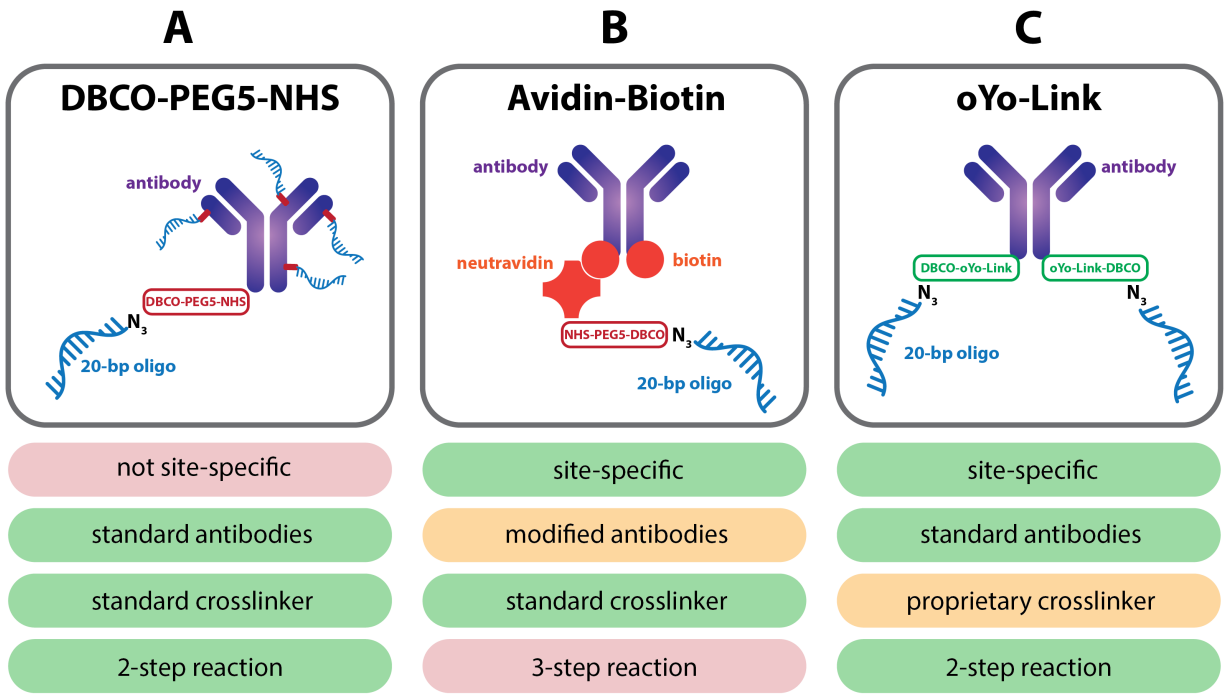


Figure 5.5: Comparison of Protein Labeling Approaches Using Three Different Crosslinkers. Three protein labeling approaches were considered for conjugating 20-bp oligos to antibodies. (A) Generic $DBCO - PEG_5 - NHS$ Crosslinker: A copper free-click chemistry reaction covalently binds a azide-terminated oligo to a DBCO on the moeity on the crosslinker. Then, the NHS ester on the same crosslinker is allowed to covalently binds to free amino groups anywhere on the antibody protein. (B) Avidin-Biotin Chemistry: A biotinylated antibody is used, enabling a site-specific conjugation. Oligos are bound to a neutravidin protein using the same $DBCO - PEG_5 - NHS$ crosslinker described in (A). The oligo-neutravidin conjugate is then bound to a commercially available biotinylated antibody. (C) oYo-Link Crosslinker: a site-specific crosslinker, produced commercially as oYo-Link by AlphaThera, can also be used for site-specific antibody labeling. In this approach, a proprietary light activated crosslinker is used to bind an oligo to the Fc region of any antibody.

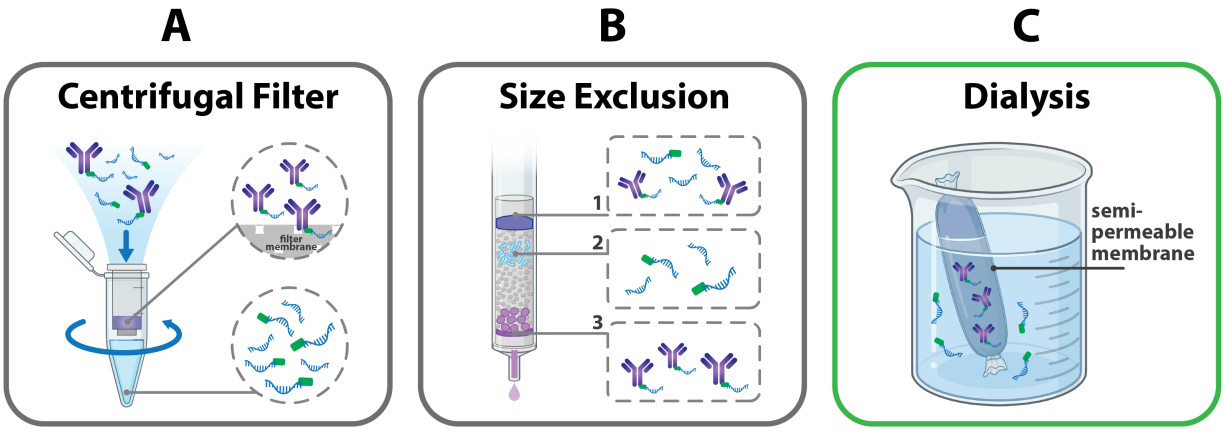


Figure 5.6: Protein Filtering Approaches. Three protein filtering approaches were evaluated for purifying the final oligo-antibody product from excess reactants. (A) Ultra-centrifugal filter: a regenerated cellulose membrane filters based on molecular weight (MW) cut-offs. Low MW compounds, such as excess oligos, are driven through the filer, leaving behind the concentrated high MW oligo-antibody product. (B) Size exclusion chromatography: a gel consisting of packed spherical beads with pores of a specific size distribution filter proteins based on MW. The high MW oligo-antibody product will pass though the gel, while excess oligos remain trapped within the interstitial pores. (C) Dialysis: A semi-permeable membrane filters out small molecules based on selective passive diffusion.

pounds, such as excess oligos, are driven through the filer, leaving the high MW oligo-antibody product trapped within and above the filter membrane. The product is recovered from the filter by inverting the filter above a collection tube and performing an additional centrifugal step. Next, size exclusion chromatography uses a filter gel consisting of re-hydrated packed spherical beads **(Figure 5.6B)**. The beads are crosslinked hydrogel polymers with a fixed matrix exclusion pores size. Consequently, proteins and molecules will pass through the gel at varying rates depending on MW. High MW oligo-antibody product will pass though the gel, while excess oligos remain trapped within the interstitial pores. Finally, dialysis filtering uses a high-purity, semi-permeable cellulose ester (CE) membrane filter to allow the selective diffusion of molecules based on a specific MW cut-offs **(Figure 5.6C)**. This approach is similar to a centrifugal filter; however, the driving force behind protein/molecule separation is passive diffusion, rather than centrifugal force.

The protein purification methods detailed in **Figure 5.6** are evaluated using SDS-PAGE (sodium dodecyl sulfate–polyacrylamide gel electrophoresis). SDS-PAGE is an electrophoretic separation technique that uses a polyacrylamide gel and a constant electric field to separate proteins in a sample by molecular weight. The sample used to compare purification approaches is a Mouse IgG1 isotype control antibody (ThermoFisher, host: mouse IgG1, clone: P3.6.2.8.1) conjugated to A' oligo (see Table 5.1) using an oYo-Link crosslinker (see method

detailed in Section 5.4.1).

For ultra-centrifugal filtering, Amicon (Millipore Sigma, 100 kDa MWCO, 0.5 mL) ultra-centrifugal filters are used. The filter is hydrated with 250 mL of 0.2M sodium bicarbonate ($NaHCO_3$) buffer for 5 min. 200 μL of sample is added to the filter. The filter is placed within a waste tube and together, centrifuged at 14000 RCF (relative centrifugal force), 4°C for 10 min. To collect the purified oligo-antibody product, the filter is inverted within a separate collection tube, and again centrifuged at 14000 RCF (relative centrifugal force), 4°C for 10 min.

For size exclusion chromatography, a Centri-Spin 40 Spin Column (Princeton Separations) is used. The beads within the column are settled by gently tapping the column against a flat surface. Next, the column is hydrated by adding 650 mL of 0.2M sodium bicarbonate ($NaHCO_3$), vortexing, and incubating for 2 hours. Trapped bubbles within the column after vortexing are released by agitating and tapping the column tube. After re-hydration, the interstitial fluid is removed by centrifuging at 1000 RCF, 4°C for 10 min. The column is placed within a collection tube, and 50 μL of sample is added to the column. Together, the column and collection tube is centrifuged at 1000 RCF, 4°C for 10 min.

For dialysis filtering, a SpectraPor Micro Float-A-Lyzer Dialysis Filter (Repligen, 100 kDa, 100-200 μL) is used. To clean the membrane, 200 μL of 15% reagent alcohol is added to the dialysis device. The dialysis device is submerged in beaker containing 200 mL of 15% reagent alcohol, with a stir bar, for 15 min. The dialysis membrane is then rinsed with mg water 3 times, and submerged in beaker containing 200 mL of mg water, with a stir bar, for 30 min. To add the sample, all fluid is removed from the membrane. The membrane is rinsed with PBS, and then 200 μL of sample is loaded into the membrane. The dialysis device is submerged in beaker containing 200 mL of PBS, with a stir bar, for 24 to 36 hours. The PBS buffer is exchanged periodically, to maximize diffusive filtering. The sample is recovered from the dialysis device, and stored at 4°C.

SDS-PAGE was used to evaluate each protein purification approach. Protein bands for oYo-Link+A' crosslinker-oligo conjugate only (without antibody) is shown in **Figure 5.7A**. The final, unpurified antibody-oligo conjugate, human EpCAM-A'-Cy5, is shown in **Figure5.7B**. Note the presence of low MW excess reactants, including unreacted oligo and unreacted oYo-Link+A' crosslinker-oligo conjugate. These low MW bands match with the bands shown in **Figure 5.7A**. The Amicon ultra-centrifugal filter and Centri-Spin size exclusion column approaches both show significant amounts of low MW compounds, indicating poor purification **(Figure 5.7C and D)**. Fluorescent high MW bands at approximately 75 kDa indicate successful oligo-antibody conjugation, because the fluorescent fluorophore is only present on the oligo. The bands present at 10 kDa are indicative of excess unconjugated oligo, while bands between 15-30 kDa are most likely excess oYo-Link + oligo compounds and oligo dimers. In contrast, the dialysis approach shows minimal bands at low MW while retaining the high MW bands at 75 kDa, indicating successful purification of the oligo-antibody target **(Figure**

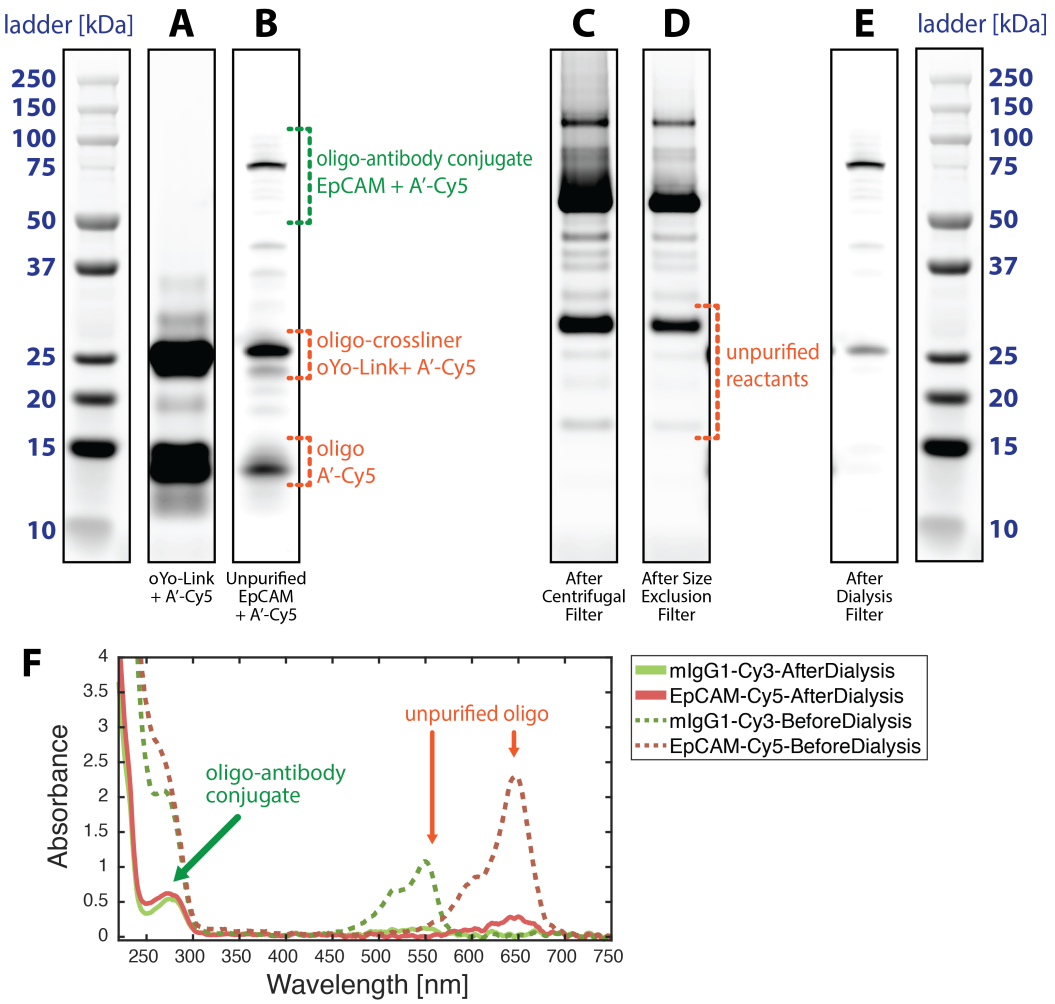


Figure 5.7: Evaluation of Protein Filtering Approaches Using Gel Electrophoresis and Microvolume Spectroscopy. The efficacy of different protein purification methods were tested with human EpCAM + A' oligo-antibody conjugate using SDS-PAGE. Protein bands are shown under reducing conditions in a SDS-PAGE gel, imaging for fluorescent Cy5. Protein ladder bands shown range from 10-250 kDa.(A) Protein bands of only oYo-Link-DBCO crosslinker conjugated to A'-Cy5 oligo. (B) Unfiltered Human EpCAM + A' oligo-antibody conjugate. From high MW to low MW, the bands indicate the final conjugation product, excess oYo-Link+A', and excess A' oligo. (C) Human EpCAM + A' conjugate purified using an Amicon ultra-centrifugal filter. (D) Human EpCAM + A' conjugate purified using an Centri-Spin 40 size exclusion chromatography column. (E) Human EpCAM + A' conjugate purified using a Repligen dialysis membrane. In (C), (D), and (E), all three show the presence of the target Human EpCAM + A' conjugate at approximately 75 kDa. In (C) and (D), excess low MW compounds (below 40 kDa) indicate poor purification by ultra-centrifugal and size-exclusion filtering. In (E), reduced low MW bands (below 40 kDa) indicate successful purification by dialysis. (F) The UV-Visible absorbance curve of purified (via dialysis) and unpurified oligo-antibody conjugates.

5.7E). Microvolume spectroscopy using a Nanodrop instrument (Thermo Fisher Scientific) further confirms successful purification via dialysis. The UV-Visible absorbance curve of purified and unpurified labeled protein is shown in **Figure 5.7F** . The peaks at 280 nm indicate the presence of oligo-antibody conjugates. Further peaks at the excitation/emission wavelengths of Cy3 and Cy5 in the unpurified samples indicate excess oligo. Meanwhile, diminished peaks at the excitation/emission wavelengths of Cy3 and Cy5 in the purified samples indicate successful dialysis filtering.

5.5 Fabrication and Experimental Methods

The following subsections detail the specific design geometries used for Combo-NPS, additional experimental methods, including DNA-directed patterning of antibodies, and data analysis processes used for extracting relevant signal features.

5.5.1 Channel Design and Fabrication

For all devices, the antibody expansion regions used the same channel dimensions. However, two channel dimensions were employed such that cell types with different mean diameters would be strained equivalently in the contraction region. Table 5.3 details the specific geometries used for each cell type measured.

Table 5.3: Combo-NPS Microfluidic Channel Dimensions Used For Each Cell Type.

Cell Type	**Avg** D_{cell} (μm)	W_p (μm)	$W_{contraction}$ (μm)	**Height** (μm)	**Strain** (ϵ)
MCF-7	18.26	21.00	12.50	21.52	46%
MDA-MB-231	15.29				46%
MCF10A	15.37	19.00	10.50	20.91	46%
HMEC (240L)	15.63				49%

To fabricate Combo-NPS devices, the standard soft-lithography approach was used, as detailed in Section 3.3. However, important additional steps were used to spatially pre-pattern DNA oligonucleotides onto the glass surface. Subsequent modifications to the methods described in Section 3.3.3 were also undertaken to preserve the oligo patterning during plasma bonding.

Photo-lithography is used to pattern the glass surface with 20-bp oligos, complementary to the strands listed in Table 5.1. This process is described in-detail in [215]. Briefly, aldehyde functionalized glass slides are patterned with Ti/Pt/Au electrodes as described in Section 3.3.2. After electrode patterning, positive photoresist S1813 is spin-coated, baked, exposed, and developed on the glass slide **(Figure 5.8A)**. Oligos are drop-casted onto the exposed areas of interest; the photoresist acts as a physical barrier, similar to the lift-off process

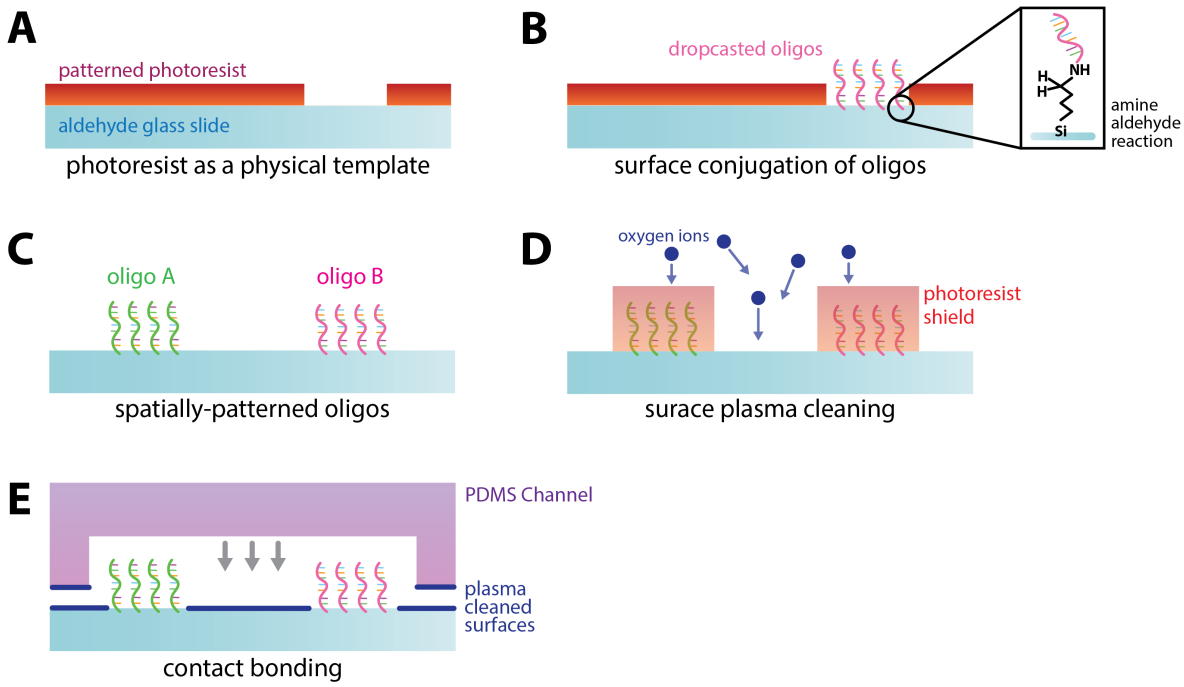


Figure 5.8: Combo-NPS Fabrication: DNA Patterning and Plasma Shield Incorporation. The fabrication steps for Combo-NPS modify the generalized procedure detailed in Section 3.3. To pre-pattern DNA oligos on the glass slide, (A) photoresist is patterned on an aldehyde glass slide and (B) amine-terminated oligos are drop-casted and allowed to covalently bond to the aldehyde surface via reductive amination. (C) Steps (A) and (B) are repeated to allow for a multi-component DNA-patterned surface. (D) Prior to plasma exposure, the oligos are masked and protected by a layer of photoresist. (E) The photoresist is removed, and the molded PDMS is allowed to bond to the glass surface, enclosing the pre-patterned DNA oligos within a microfluidic channel.

in electrode patterning. The oligos are terminated with an amine group (NH_2) that react directly with the aldehyde group on the glass surface. The slide is baked in an oven at 80°C for 30 min. The dehydrated slide is then place in 0.25% sodium borohydride in 1X PBS for 15 min. This initiates a reductive amination chemistry that creates irreversible C-N bonds between the oligo and glass slide **(Figure 5.8B)**. The remaining resist is then removed by rinsing the slide with water and acetone. These steps are then repeated for the second oligo strand to be pattern **(Figure 5.8C)**.

The process of plasma bonding bombards the glass surface with high energy oxygen ions. Doing so would damage the pre-patterned oligos; thus, an additional step is taken to preserve the surface oligos. Photoresist is patterned over the oligo regions before exposure to oxygen plasma, serving as a physical barrier against the high-energy ions **(Figure 5.8D)**. After oxygen plasma, the photoresist is rinsed off with acetone, and the bonding can proceed as normal **(Figure 5.8E)**, as described in Section 3.3.3.

5.5.2 Cell Culture and Preparation

Cells were cultured and prepared according to the same protocols as described in section 4.4.2. However, because Combo-NPS probes cellular surface markers, three modifications were made to improve surface marker preservation. First, adherent cells were released using TrypLE, a synthetic version of trypsin. TrypLE is gentler on cells, reducing the damage that can typically occur due to harsh cleavage enzymes found in trypsin. Trypsin itself is known to strip cell surface proteins [242]. In contrast, TrypLE has been shown to better preserve surface marker viability [243, 244]. Second, cells are re-suspended in PBS containing 2% (v/v) FBS and 0.1% (w/v) sodium azide. The presence of sodium azide limits metabolic activity, preventing the capping and internalization of surface antigens [245]. This again helps preserve surface marker expression during Combo-NPS experimental runs. Time between cell preparation and on-chip experimental processing can range between 15 to 90 min; thus, any step to help preserve surface marker expression can be critical. Finally, prepared cell samples are kept at room temperature (21°C), rather than on ice (4°C). As discussed in Section 5.3, temperature play an important role in antibody-antigen binding kinetics. By keeping the cells at room temperature, the interaction kinetics are improved [238], maximizing Combo-NPS measurement sensitivity. Experimental time frames range from 1 to 3 hours; cells have been shown to be viable at room temperature for up to 24 hours [246, 247].

5.5.3 Experimental Methods

First, the antibody expansion regions in the channel, pre-patterned with DNA oligos (see Section 5.5.1) **(Figure 5.9A)**, are prepared for DNA-directed patterning of surface-immobilized antibodies by flowing a solution of 2% BSA in PBA (w/v) at 60 mBar for 15 min. The solution is incubated in the channel for 30 min to passivate the PDMS channel walls, reducing non-specific adhesion of downstream biological compounds, such as antibodies and cells. After, the channel is flushed with PBS at 60 mBar for 15 min. A mixture of 2 oligo-antibody conjugates, each with a distinct oligo label, is prepared at a 1:1 ratio to a final concentration of 0.4 μM. The oligo-antibody conjugates mixture is flowed through the channel at 60 mBar for 15 min, and allowed to further incubate for 30 min **(Figure 5.9B)**. Unbound excess oligo-antibody conjugates are then flushed out with PBS at 60 mBar for 15 min. Only the surface-immobilized antibodies in each region remain **(Figure 5.9C)**.

To begin an experimental run, cells are suspended at a concentration of $1.5 - 2.5 \times 10^5$ cells/mL (see Section 4.4.2 and 5.5.2) and introduced into the Combo-NPS microfluidic channel at a pressure of 50-150 mBar. The device is connected to the Multi-Zone hardware (see Section 3.4), and data acquisition of the resistance pulses is run for 5 to 10 min, yielding 50 to 100 single cell measurements. The tubing can be re-loaded with additional cells and a new data acquisition run commenced.

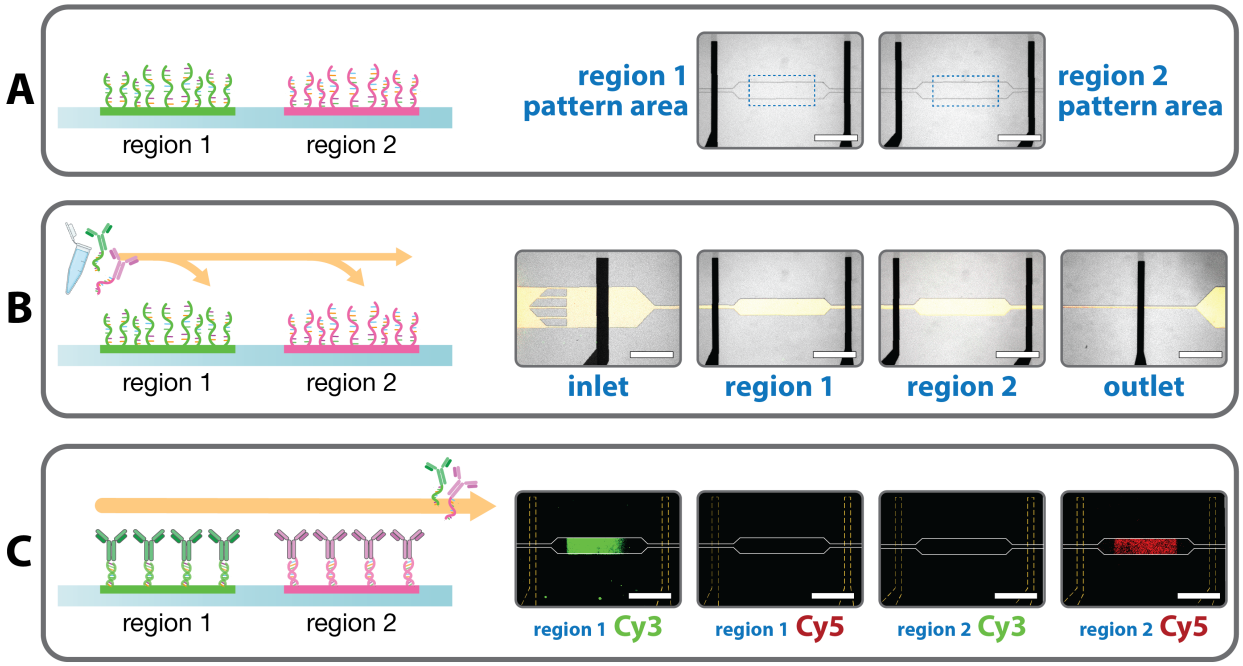


Figure 5.9: On-Chip DNA Patterning of Antibodies. Mouse IgG1-A'-Cy3 and Human EpCAM-G'-Cy5 oligo-antibody conjugates were simultaneously surface-immobilized in a Combo-NPS microfluidic channel. (A) The microfluidic channel contains two regions with pre-patterned surface oligos. (B) Mouse IgG1-A'-Cy3 and Human EpCAM-G'-Cy5 are flowed into the channel. The entire channel is saturated with both protein conjugates. Images shown combine brightfield (BF), Cy3, and Cy5 channels. (C) Excess oligo-antibody conjugates are flushed out, leaving only the surface immobilized antibodies. Images shown are of region 1 and region 2, respectively, with separate Cy3 and Cy5 channels. The fluorescent signal confirms the successful patterning of Mouse IgG1-A'-Cy3 in region 1, and Human EpCAM-G'-Cy5 in region 2. Scale bars = 250 µm.

5.5.4 Signal Processing and Analysis

Measured resistance signals were processed and analyzed using custom MATLAB code, available in an online repository at: https://github.com/sohnlab. Signal processing, event identification, pulse cascade parsing, and signal feature extraction is described in section 3.5. Unique to the processing of Combo-NPS signals are 2 considerations: coincident and incomplete event cases and surface marker expression gating.

Non-ideal cell transit events, such as coincident, incomplete, or ambiguous cell events, are not included in the final Combo-NPS dataset. Coincident events occur when a cell enters the first measurement zone before the previous cell has exited the final measurement zone **(Figure 5.10A)**. Coincident events are flagged in the signal analysis, because they can potentially impact and confound cell transit times. A cell in the contraction channel, for

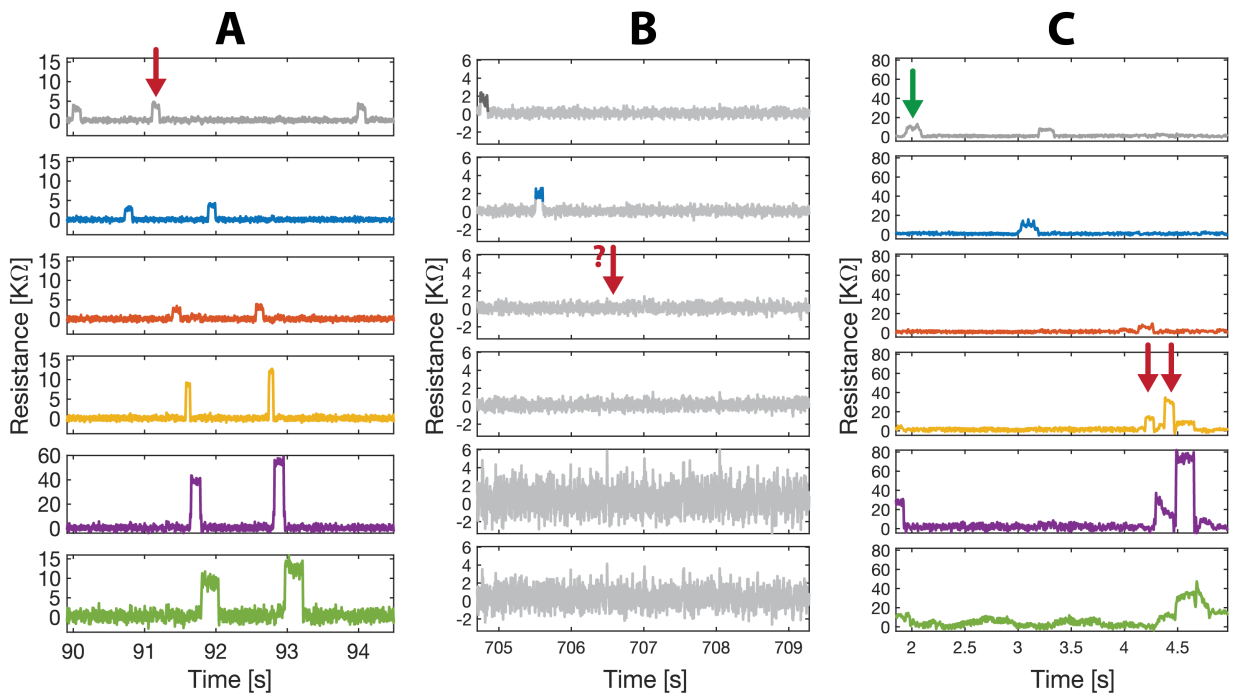


Figure 5.10: Combo-NPS Non-Ideal Event Cases. The resistance pulse cascade can result in multiple, non-ideal event cases, depending on the cell transit behavior. (A) A cell enters zone 1 (red arrow) before the previous cell has left the final measurement zone. This scenario is known as a coincident event. (B) A cell can enters the first antibody region and then the second antibody region, as indicated by a zone 1 and 2 pulse, but does not leave the second antibody region, as indicated by the lack of a zone 3 pulse (red arrow). This scenario is known as a cell idling event. (C) What appears to be a single cell entering the zone (green arrow) is actually a doublet, as indicated by a separation in the signal pulses in down-stream zones (red arrows).

example, would hinder fluidic velocities upstream, such as in the antibody expansion regions, resulting in a biased measurement. In another non-ideal transit event, cells can idle in the antibody expansion region, resulting in an incomplete resistance signal pulse cascade **(Figure 5.10B)**. Such events are flagged and removed in the signal analysis pipeline. Finally, cells can enter the measurement zones together, but gradually separate while transiting, leaving the final measurement zone separately. This is known as a doublet event, and is useful in flagging events that are not single cell **(Figure 5.10C)**.

Normalized transit time is defined as the transit time in region 2 divided by transit time in region 1. This metric is used to screen for positive surface marker expression. However, cells will transit each antibody region with a natural variance, based upon a normal distribution, regardless of their antigen-antibody interaction. To measure this variance, human MCF7 and MCF10A cells were measured as they flowed through their respective channel geometries,

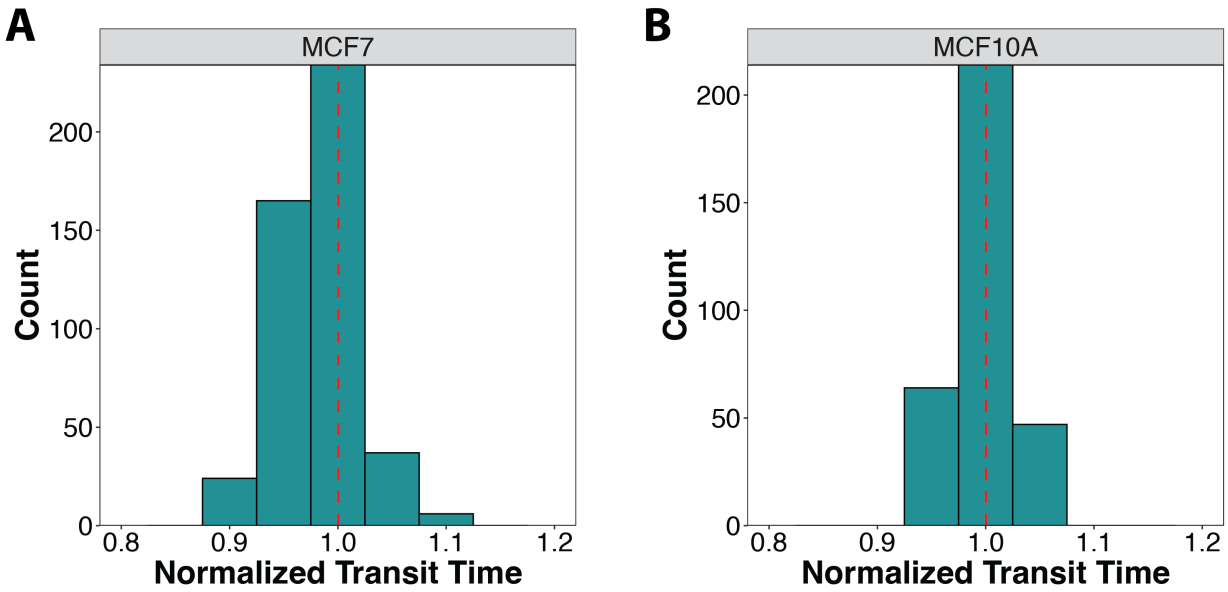


Figure 5.11: Combo-NPS Surface Marker Expression Gating. Normalized transit time is used to screen for positive surface marker expression; however, cells will transit each region with a natural variance, depending on non-specific interactions. Shown here is the distribution of the normalized transit time of (A) MCF-7 cells in W12.5 microfluidic channel, and (B) MCF-10A cells in W12.5 microfluidic channel. In each channel, both antibody expansion regions were patterned with mouse IgG1 isotype control antibody. This distribution is used to define positive surface marker expression in subsequent experiments. Histogram bin widths are equal to 0.5. Sample size: n=466 MCF-7; n=325 MCF-10A.

W12.5 and W10.5 (see Table 5.3). The antibody expansion regions were functionalized with mouse IgG1 isotype control; thus, the normalized transit time should approach unity because the cells have no reason to transit one region faster than the other. In **Figure 5.11A and B**, we see a normal distribution of normalized transit time for each cell type in each channel geometry. The MCF-7's have a greater variance than the MCF-10's, likely due to the slower flow rates in the wider W12.5 channel geometry used by the MCF-7's. Overall, both distributions have an average near one, indicating that neither antibody region has an unwarranted bias in non-specific binding. These distributions are used to ascertain the standard deviation of the normalized transit time as the cells flow over isotype control regions ($\sigma_{isotype}$). Positive surface marker expression is then conservatively gated as a normalized transit time that is two standard deviations above unity ($1 + 2\sigma_{isotype}$).

5.6 Results and Discussion

Immortalized breast epithelial cells and primary human mammary epithelial cells (HMECs) were measured using Combo-NPS to investigate surface marker and mechanophenotype dif-

ferences among non-malignant, malignant, and highly-invasive breast cancer cells. Additionally, characterizations on the inlet operating pressure were performed to better optimize Combo-NPS measurements. Overall, these results demonstrate the potential of Combo-NPS as an integrated platform for advanced multimodal single-cell biophysical phenotyping.

5.6.1 Inlet Pressure Characterizations

A critical parameter when conducting Combo-NPS experiments is the inlet pressure. As discussed in section 5.3, the fluid velocity dictates cell transit velocity, and thereby the interaction time between a cell and the surface-immobilized antibodies. We examined the relation between inlet pressure and: measurement throughput, cell coincident events, and incomplete cell transit events. To do so, MCF-7 cells were flowed through a Combo-NPS microfluidic channel, with mIgG1-G'-Cy3 antibody-oligo conjugate patterned in antibody region 1, and EpCAM-A'-Cy5 antibody-oligo conjugate patterned in antibody region 2. A parametric sweep of the inlet pressure was performed, from 50 mBar to 150 mBar. Cell suspension concentration was constant at 1.5×10^5 cells/mL for each discrete pressure tested.

Unsurprisingly, increasing inlet pressure improves measurement throughput. Examining the number of cell transit event within the first 3 min of starting inlet pressure, there is almost a 3-fold increase in throughput, from 10 cells/min at 50 mBar to 27 cell/min at 150 mBar. Also unsurprisingly, there is a strong correlation between inlet pressure and throughput, with a coefficient of determination (R^2) of 0.89 when performing a linear regression **(Figure 5.12A)**. In short, increasing inlet pressure increases measurement throughput.

The relation between inlet pressure versus coincident cell transit events were also examined. As described in Section 5.5.4 and **Figure 5.10A**, a cell transit event is considered coincident if a cell has entered the first measurement zone before the previous cell has fully exited the last measurement zone. Limiting the number of coincident cell transit events is critical, because coincident events bias cell transit timing, and need to be discarded. With a constant cell suspension concentration, coincident cell events were evaluated as a percentage of the total number of cell transit events identified for any given pressure. We found that increasing the inlet pressure increases the percent of coincident cell events **(Figure 5.12B)**. This is congruent with our previous observation that increased pressure increases cell throughput because greater cell throughput increases the probability that a cell will enter the channel before the previous cell has left.

Inlet pressure also correlates with the percent of incomplete transit event. Again, as described in Section 5.5.4 and **Figure 5.10B**, a cell transit event is considered "incomplete" if the resistance pulse cascade is not present in all six measurement zones. The most likely reason for incomplete cell transit events is the idling of cells in either antibody expansion region due to interactions (both specific and non-specific) with the channel walls and surface antibodies. Increasing inlet pressure reduces the percentage of cell events classified as

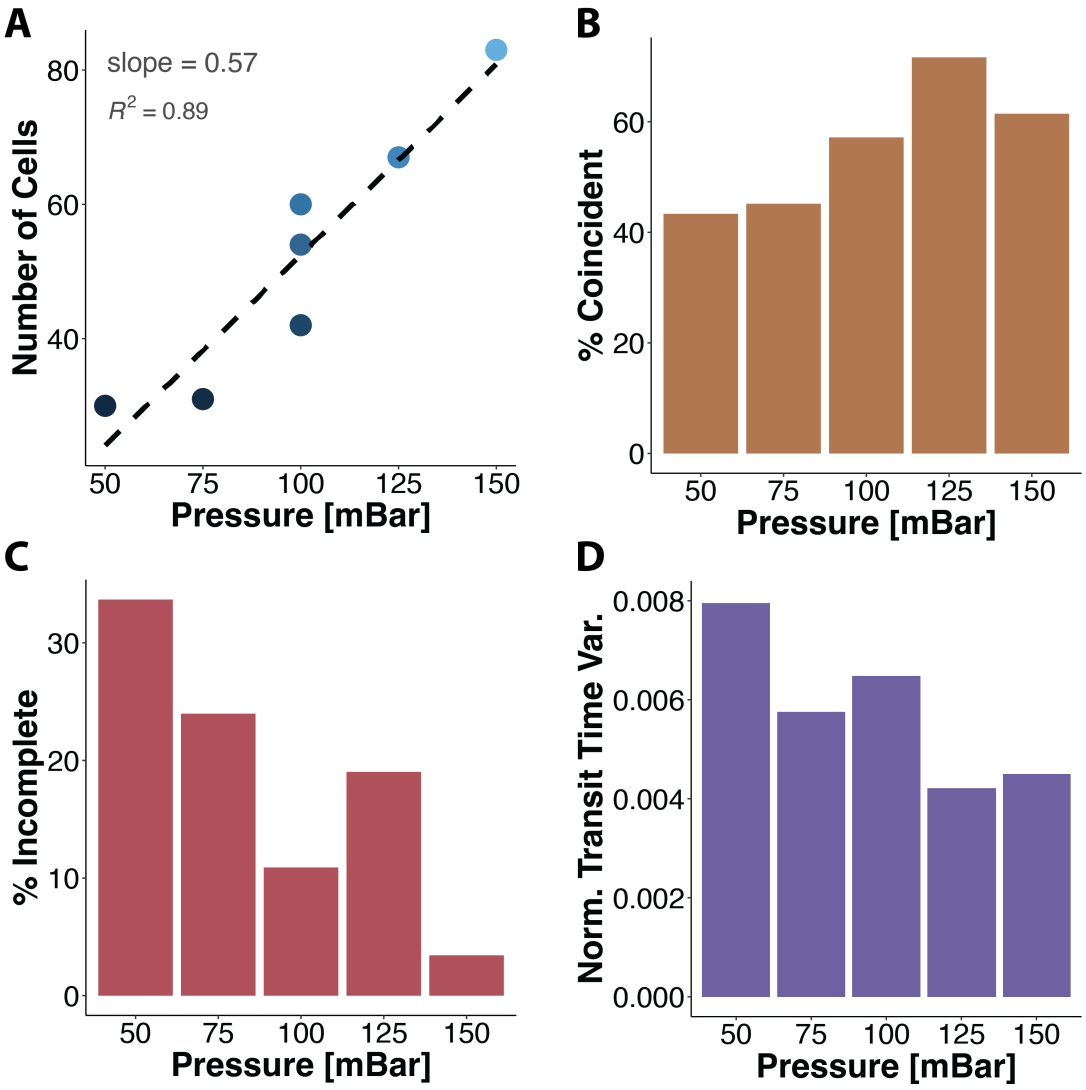


Figure 5.12: Combo-NPS Inlet Pressure Characterization. MCF-7 cells were flowed though a W12.5 Combo-NPS microfluidic channel at pressures from 50 to 150 mBar. For (A, B, C), Antibody region 1 was patterned with mIgG1-G'-Cy3 antibody-oligo conjugate; antibody region 2 was patterned with human EpCAM-A'-Cy5 antibody-oligo conjugate. For (D) Antibody region 1 and 2 were both patterned with mIgG1-G'-Cy3 antibody-oligo conjugate. For (A, B, C), sample sizes are: n=65 at 50 mBar; n=117 at 75mBar, n=288 at 100 mbar, n=139 at 125 mBar, n=169 at 150 mBar. For (D), sample sizes are: n=36 at 50 mBar; n=89 at 75mBar, n=179 at 100 mbar, n=95 at 125 mBar, n=67 at 150 mBar. (A) The number of identified cell transit events versus inlet pressure during the first 3 min after the start of pressure. (B) The percent of cell transit events classified as "coincident" versus inlet pressure during a 10 min experimental run. (C) The percent of cell transit events classified as "incomplete" versus inlet pressure during a 10 min experimental run. (D) The normalized transit time variance versus inlet pressure.

incomplete **(Figure 5.12C)**. This is presumably because at higher pressures, the flow velocities are higher, limiting the interaction time between the cell and channel surfaces, thereby reducing the chances of cell idling.

Finally, the variance in normalized transit time (time in antibody region 2 divided by time in antibody region 1) was characterized in a device where mIgG1-G'-Cy3 antibody-oligo conjugate is patterned in both antibody regions. MCF-7s were flowed through the device with the same pressure sweep of 50 mBar to 150 mBar. As described in Section 5.5.4 and **Figure 5.11**, a natural variance in normalized transit time is expected, as cells may non-specifically interact with the surface-immobilized antibodies. Limiting or reducing this variance can improve the gating of surface marker positive expression, and thus improve surface marker screening. We found that increasing inlet pressure reduces the normalized transit time variance **(Figure 5.12D)**. Once more, this presumably because at higher pressures, the greater flow velocities limit non-specific interactions.

Inlet flow characterizations inform the operating parameters of Combo-NPS experiments. Higher pressures increase measurement throughput and reduce the percentage of incomplete cell transit events. In contrast, lower pressures reduce the percentage of coincident cell events, and increase cell-antibody interaction times. For subsequent experiments detailed, an inlet pressure of 75 mBar was applied, trading off lower-throughputs for a reduction in coincident cell events and increase cell-antibody integration times.

5.6.2 Malignant MCF-7 Versus Non-Malignant MCF-10A

We screened non-maligant MCF-10A and malignant MCF-7 cells for expression of human epithelial cell adhesion molecule (EpCAM) (CD326), in addition to elastic deformability (wCDI) and viscous recovery. EpCAM is a multifaceted protein that plays crucial roles in physiological processes and cancer development. Structurally, it is a type I transmembrane glycoprotein primarily involved in cell adhesion [248]. However, EpCAM's functions have been shown to extend beyond that, playing critical roles in cancer. Specifically, in malignant cells with an epithelial phenotype, EpCAM promotes growth and invasion and serves as a biomarker for cancer stem cells (CSCs) and circulating tumor cells (CTCs) [249–251]. EpCAM's intricate functions make it a fascinating molecule with promising translational applications in breast cancer research. Likewise, cancer cell malignancy has been shown to correlate with cellular biomechanics (see Section 2.3). Simultaneously probing cellular EpCAM expression and mechanophenotype engages a new approach on two previously distinct cancer traits.

A Combo-NPS channel was functionalized with mIgG1-G'-Cy3 antibody-oligo conjugate in antibody region 1 and human EpCAM-A'-Cy5 antibody-oligo conjugate in antibody region 2. MCF-10A and MCF-7 cells were screened separately, at 75 mBar. MCF-7's have a larger

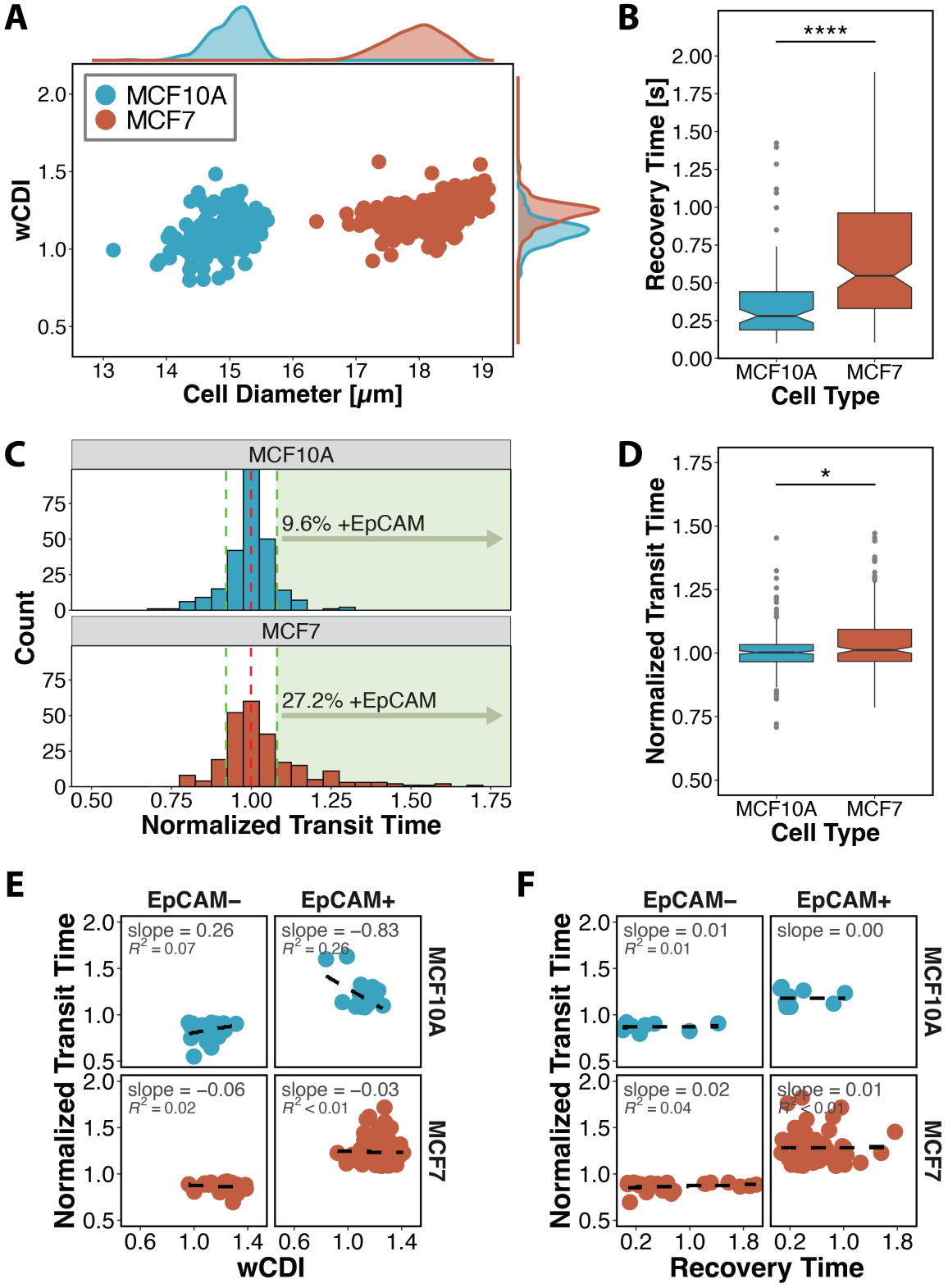

A
MCF10A
MCF7
wCDI
Cell Diameter [μm]
B
****
Recovery Time [s]
MCF10A
MCF7
Cell Type
C
MCF10A
9.6% +EpCAM
MCF7
27.2% +EpCAM
Count
Normalized Transit Time
D
*
Normalized Transit Time
MCF10A
MCF7
Cell Type
E
EpCAM–
EpCAM+
slope = 0.26
R^2 = 0.07
slope = –0.83
R^2 = 0.26
slope = –0.06
R^2 = 0.02
slope = –0.03
R^2 < 0.01
MCF10A
MCF7
Normalized Transit Time
wCDI
F
EpCAM–
EpCAM+
slope = 0.01
R^2 = 0.01
slope = 0.00
slope = 0.02
R^2 = 0.04
slope = 0.01
R^2 < 0.01
MCF10A
MCF7
Normalized Transit Time
Recovery Time

Figure 5.13: Mechanophenotype and EpCAM Expression of MCF-7 and MCF-10A Cells. Non-malignant MCF10A and malignant MCF-7 cells were screened for human EpCAM expression and simultaneously mechanophenotyped with Combo-NPS. Cells were flowed though a W10.5 or W12.5 Combo-NPS microfluidic channel with pressure-driven flow at 75 mBar. Prior to the measurement, antibody region 1 was patterned with mIgG1-G'-Cy3 antibody-oligo conjugate; antibody region 2 was patterned with human EpCAM-A'-Cy5 antibody-oligo conjugate. Sample size: n=320 MCF-10A, n=320 MCF-7. (A) Scatter plot of the measured wCDI versus cell diameter; the margins show each variable's respective distribution with a smoothed density plot. MCF-10A's have a smaller diameter distribution than MCF-7's. MCF-10A's also have a lower deformability than MCF-7's. (B) Boxplot of the viscous recovery times of MCF-10A and MCF-7 cells; MCF-7's have a more viscous phenotype. (C) Histogram of normalized transit time across both antibody regions for MCF-10A and MCF-7 cells. Positive EpCAM expression gating ($1 + 2\sigma_{isotype}$) is indicated with a dotted green line, with the percentage of positive cells shaded in green. (D) Boxplot of the normalized transit time for MCF-10A and MCF-7 population; MCF-7 cells have a statistically greater normalized transit time than MCF-10A cells. (E) Positive and negative EpCAM correlation with wCDI, for each cell type. (F) Positive and negative EpCAM correlation with recovery time, for each cell type. Correlations in (D) and (F) were calculated using ordinary least squares (OLS) regression. Slope and R^2 values are reported for each plot.

size distribution and are consistently more deformable than MCF-10A cells **(Figure 5.13A)**. MCF-7 cells have a measured wCDI 10-15% greater than that for MCF-10A's. Likewise, MCF-10A cells are also less viscous than MCF-7 cells, having an average recovery time that is 2x faster than MCF-7's **(Figure 5.13B)**.

Of the single cell populations screened, 27% of EpCAM cells have positive EpCAM expression, compared to just 9% of MCF-10A cells **(Figure 5.13C)**. Overall, MCF-7 cells have a normalized transit time that is approximately 400 ms slower than MCF-10A cells **(Figure 5.13D)**. As expected, this indicates that a greater proportion of the MCF-7 population were EpCAM+ versus the MCF-10A population screened.

Finally, we examined specific correlations between mechanophenotype and EpCAM expression using ordinary least squares regression **(Figure 5.13 E and F)**. Strong correlations were not identified; however, we found that among EpCAM positive MCF-10A cells, some variation in deformability is associated with surface marker expression. We show a slight inverse relation to deformability: greater EpCAM expression (higher normalized transit time) in MCF-10As show a stiffer phenotype (lower wCDI), with a marginal R^2 of 0.26.

5.6.3 Screening of Heterogeneous Cell Mixtures

By integrating immunophenotyping upstream of mechanophenotyping, heterogeneous cell populations or cell subpopulations can be identified and measured without the need for pre-

sorting. A 1:1 mixture of MCF-10A and MDA-MB-231 cells were measured and screened for E-Cadherin (E-Cad) and Mucin1 (Muc1) expression. These targets were chosen because they are expected to be differentially expressed between the 2 cell types: MCF-10A's are E-Cad positive and Muc1 negative; vice versa, MDA-MB-231's are E-Cad negative and Muc-1 positive [252, 253]. A Combo-NPS channel was functionalized with Muc1 in antibody expansion region 1, and E-Cad in antibody expansion region 2. Cells with positive surface marker expression (E-Cad+ = normalized transit time $> 1 + 2\sigma_{isotype}$, Muc1+ = normalized transit time $< 1 + 2\sigma_{isotype}$) were plotted against wCDI **(Figure 5.14A)** and recovery time **(Figure 5.14B)**. E-Cad+ cells were statistically less deformable (lower wCDI) than Muc1+ cells. This is as expected; the proportion of E-Cad+ cells are expected to be MCF-10A cells, while the proportion of Muc1+ cells are expected to be MDA-MB-231 cells. MCF-10A are known to be stiffer than their invasive counterpart, MDA-MB-231 [116]. No differences were seen in the recovery time distribution.

Similarly, primary human mammary epithelial cells (HMEC) were screened for myoepithelial (MEp) and luminal epithelial (LEp) subpopulations, distinct lineages in which the former is considered a tumor-suppressive cell-type, while the latter is considered a carcinogenic target-cell-type [254, 255]. MEp's are CD271+/CD133-, while LEp's are CD271-/CD133+ [256]. A Combo-NPS channel was functionalized with CD133 in antibody expansion region 1, and CD271 in antibody expansion region 2. Once more, cells with positive surface marker expression (CD271+ = normalized transit time1 $> 1 + 2\sigma_{isotype}$, CD133+ = normalized transit time $< 1 + 2\sigma_{isotype}$) were plotted against wCDI **(Figure 5.14C)** and recovery time **(Figure 5.14D)**. CD271+ (MEp) cells had a marginally lower wCDI distribution than CD133+ (LEp) cells, though population means were not statistically different. Nonetheless, the bimodal wCDI distribution is consistent with previous studies [132], indicating that MEp's tend to be stiffer than LEp's. As with the MCF-10A/MDA-MB-231 measurements, no differences were seen in the recovery time distribution between the MEp and LEp HMEC subpopulations.

5.6.4 Discussion

In screening MCF-10A cells and MCF-7 cells, we demonstrate that MCF-7's are more deformable, more viscous, and have greater expression of the EpCAM antigen. These traits are all consistent with the physical changes attributed to malignant cells, when compared to their non-malignant counterparts.

MCF-7 cells typically express EpCAM highly, though specific rates can vary depending on any given population [257]. The lower expression values reported here can be attributed to many measurement factors, such as non-specific binding and cell-surface interactions. It is expected that a proportion of the cells flow at streamlines along the top of the microfluidic channel, away from the surface-immobilized antibodies. The height is designed to be 3-5 μm larger than the mean cell diameter, constraining cell movement and encouraging cell-

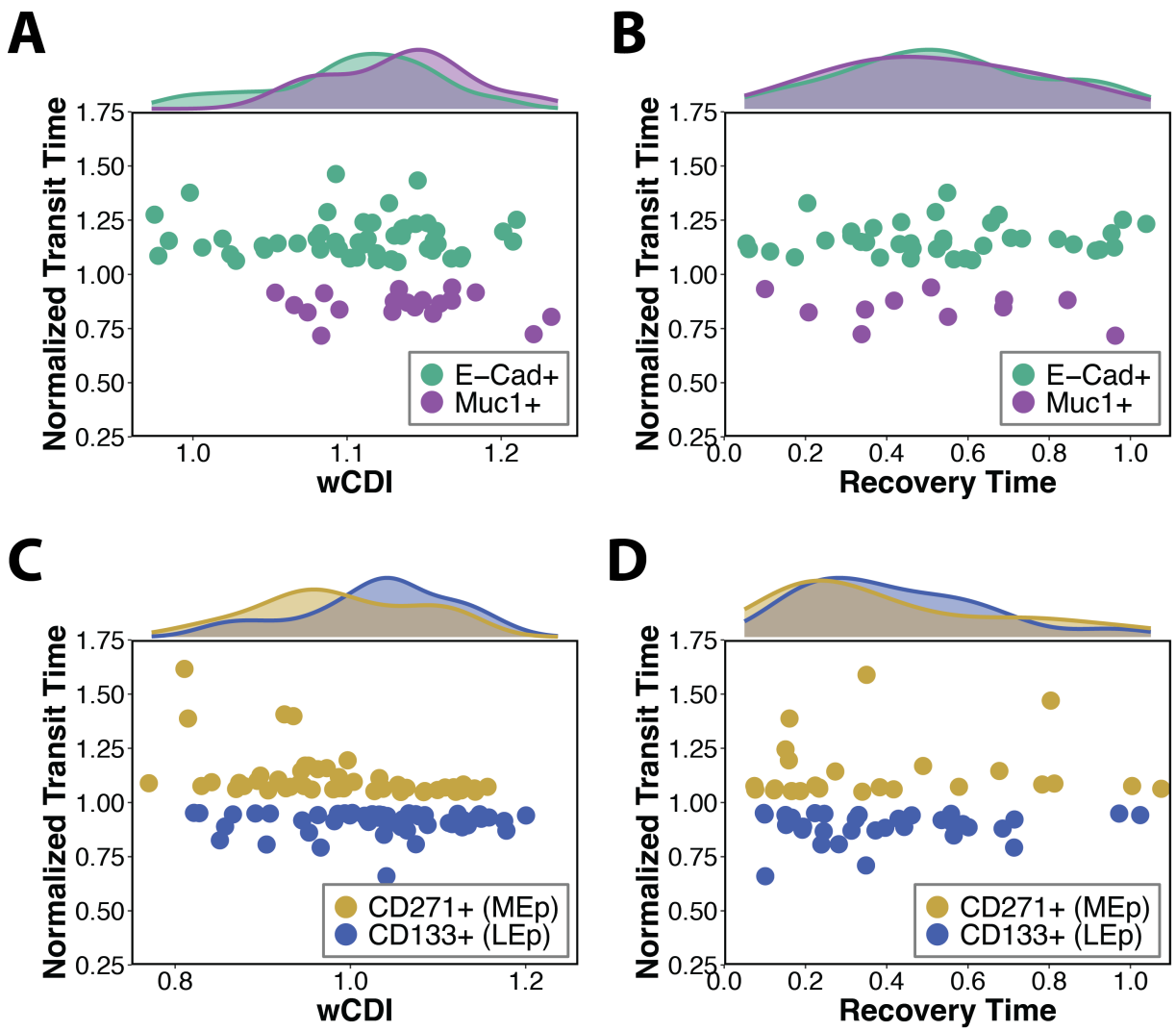


Figure 5.14: Simultaneous Mechano- & Immuno- Phenotype of Heterogenous Cell Populations. (A,B) A 1:1 heterogenous mixture of MCF-10A and MDA-MB-231 cells were screened against E-cadherin (E-Cad) and Mucin1 (Muc1) surface markers. MCF-10A's are expected to be E-Cad+/Muc1- (green), while MDA-MB-231 are expected to be E-Cad-/Muc1+ (purple). Shown are scatter plots of normalized transit time versus (A) wCDI or (B) recovery time. Only cells with surface marker expression gated as either E-Cad+ or Muc1+ are shown. The margins show the respective mechanophenotype distribution with a smoothed density plot. Sample size: n=58 are E-Cad+, and n=22 are Muc1+. (C,D) HMEC's (240L) screened against CD271 and CD133 surface markers. HMEC MEp subpopulations are expected to be CD271+/CD133- (gold), while the LEp subpopulations are expected to be CD271-/CD133+ (blue). Shown are scatter plots of normalized transit time versus (C) wCDI or (D) recovery time. Only cells with surface marker expression gated as either CD271+ or CD133+ are shown. The margins show the respective mechanophenotype distribution with a smoothed density plot. Sample size: n=71 are CD271+, and n=85 are CD133+.

antibody interactions. However, reducing the channel height further to improve interaction probability would adversely strain passing cells. It is also important to note that Combo-NPS screens for relative expression; in this case, against a control mIgG1 antibody. Cells interacting non-specifically with mIgG1 at rates similar to their interaction with EpCAM will result in a normalized transit time measurement that does not indicate positive EpCAM expression. In this scenario, the cell does express EpCAM, but it's EpCAM interaction did not out-weight non-specific interactions. Again, this measurement scenario can result in a lower proportion of cells gated as EpCAM+.

We also examined correlations between EpCAM expression and mechanophenotype. Compared to MCF-7's, MCF-10A's are not expected to overexpress EpCAM [252]. Positive EpCAM MCF-10A cells are thus less common. For the most part, the linear regression between +/-EpCAM, wCDI, and recovery time were largely negligible, with $R^2 < 0.1$. However, in one comparison, the correlation between +EpCAM MCF10A cells and wCDI had a $R^2 = 0.26$. While marginal, the higher determination of coefficient was distinctive amongst the other comparisons examined. Further studies probing the relation between increased EpCAM expression and a decrease in deformability would be needed to validate this result. One hypothesis is that increased EpCAM expression help stabilize the cellular cytoskeleton, as EpCAM has been shown to directly interact with the actin cytoskeleton [258]. This would explain why greater EpCAM expression might correlate with a mechanically stiffer cell.

A significant advantage of simultaneous immuno- and mechano- phenotyping is the capability of measuring heterogeneous populations or subpopulations without the need for pre-sorting the sample. We demonstrated this approach with an artificial heterogeneous population of MCF-10A and MDA-MB-231 cells, as well as with subpopulation screening of HMEC's. In both experiments, the wCDI characteristics of the positively gated cells corresponded with the expected phenotype: E-Cad+ cells, a phenotype consistent with MCF-10A's, were stiffer than Muc1+ cells, a phenotype consistent with MDA-MB-231's. Likewise, CD271+ cells, a marker of the MEp subpopulation lineage, had a lower wCDI distribution than CD133+ cells, a marker of the LEp subpopulation. In either case, the more "invasive" cell type (MDA-MB-231 or LEp) was softer or more deformable than their "non-malignant" counterpart (MCF-10A or MEp, respectively). Once more, this is consistent with numerous studies that have shown tumor, or invasive cells, to be softer, more deformable, and more compliant than their health counterparts [106].

The proportion of positively gated cells were limited in all experiments. For example, in the HMEC subpopulation experiment, a total of n=651 cells were measured, with only 10-15% gated as positive for either CD271 or CD133. As mentioned earlier, this can be due to interaction characteristics, such as non-specific binding or cell positioning away from the channel surface. Furthermore, defining positive expression as greater or less than $1+2\sigma_{isotype}$ is a conservative metric that further limits the proportion of positive expression cells. Future designs could focus on improving transient antibody-antigen interaction measurements.

For example, incorporating a longer antibody expansion region could potentially improve measurement sensitivity. Likewise, the addition of a third antibody expansion region can mitigate issues with a relative measurement against a single control and help create a more robust surface marker expression profile for each cell.

Overall, we present a microfluidic platform for a multi-phenome measurement of single cells. The paired readouts of immuno- and mechano- phenotypes enables unique analyses in single-cell characteristics among non-malignant and malignant breast epithelial cells.

5.7 Conclusion

In this chapter, I introduced Combo-NPS, an innovative microfluidic platform designed for integrated single-cell phenotyping of multiple biophysical attributes. By combining DNA-directed patterning and NPS technology within a single microfluidic channel, Combo-NPS enables simultaneous measurements of surface markers, cell diameter, elastic deformability, and viscous recovery. Specifically, DNA-directed allows for one-step surface functionalization with immobilized antibodies for surface marker screening. Meanwhile, NPS enables an optics-free, all-electronic measurement that can assess passing cells at moderate throughputs. I delved into the technical details behind the platform, covering aspects such as channel design, protein labeling, antibody surface patterning, and experimental execution. The results, based on measurements of immortalized breast epithelial cells and primary HMECs, demonstrate unique paired analyses between surface marker expression and mechanophenotype. Overall, Combo-NPS sets a new standard for multimodal single-cell biophysical phenotyping.

Chapter 6

Conclusions and Future Directions

In this dissertation, I discuss the development and experimental execution of novel microfluidic platforms for single-cell multimodal biophysical phenotyping. Broadly speaking, these microfluidic platforms serve to complement and enhance biological inquiries by providing innovative tools and approaches to address previously unexplored questions. Here, I summarize the background discussed in Chapter 2 and 3, and the primary results from the Multi-Zone Visco NPS and Combo-NPS platforms in Chapter 4 and 5. I also discuss future directions relevant to the continued development of these platforms, and conclude with final thoughts.

6.1 Summary

The primary scientific contribution presented in this dissertation is the development of Multi-Zone Visco-NPS and Combo-NPS, two unique microfluidic platforms for multi-modal single-cell biophysical phenotyping.

As discussed in Chapter 2, microfluidics refers to the manipulation of fluids at the micro-scale, especially useful when studying and perturbing biological species such as single-cells [259]. Here, I describe microfluidic devices for measuring the biophysical properties of single cells. In particular, "single-cell biophysical properties" is defined as the mechano- and immuno- phenotype of a cell. The former refers to the mechanical attributes of the cell, i.e. elasticity and viscocity, while the latter refers to the surface proteome of the cell, i.e. surface antigens, ligands, etc. The mechanophenotype of a cell is dictated by sub-cellular components including the cytoskeleton, membrane, and nucleus [140, 141], and is a reflection of the cell's state [113]. Specifically, it is known that a progression towards malignancy results in mechanical changes, often towards a softer, more deformable cell [106]. By developing microfluidic tools for the mechano- and immuno- phenotyping of single-cells, I contribute to broader research questions that aim to understand the biophysical aspects of cells in both health and disease.

The methodologies employed in Multi-Zone Visco-NPS and Combo-NPS utilize two core technologies, node-pore sensing (NPS) [1] and DNA-directed patterning [215]. These approaches are further discussed in Chapter 3. Node-pore sensing (NPS) [1] is a technique used to rapidly and electronically measure cells as they transit a microfluidic channel. Briefly, in NPS, the electrical resistance across the microfluidic channel is recorded as pressure-driven flow moves a cell through the channel. The channel itself is modulated with a series of node and pores, in addition to a narrow contraction channel. The magnitude of the resistance pulses measured is proportional to cell's diameter, while the timing of the pulse itself gives information about the cell's spatial position and transit time. This information is used to calculate the cell's biophysical properties, such as the whole-cell deformability index (wCDI) [132]. In Combo-NPS [215], this all-electronic NPS approach is further supplemented by DNA-directed patterning. In this process, antibodies labeled with oligos are functionalized along the channel surface using pre-patterned complementary oligos. By incorporating surface-immobilized antibodies, the immunophenotype of cells can be measured in addition to their mechanophenotype.

In Chapter 4, I describe Multi-Zone Visco-NPS, a microfluidic platform for measuring the dynamic rheological properties of cells. The channel design is divided into multiple zones, each consisting of a sinusoidal contraction channel, that are aligned in series to perturb passing cells at increasing frequencies. The measured resistance pulses are used to model the stress on each passing cell, which can then be used to calculate the cell's frequency-dependent storage (G') and loss (G") modulus. Compared to previously published methods [116, 159, 186, 187, 204], this approach is uniquely capable of measuring single-cell viscoelastic properties at multiple distinct frequencies in moderate-throughputs of up to 10 cells/min. I report measurements on MCF-7 breast epithelial cells before and after actin cytoskeletal perturbation. I also report results on the viscoelastic properties of human mammary epithelial cells (HMEC) that represented the entire continuum of epithelial transformation states: from normal average risk and BRCA1 mutant high-risk primary epithelial cells, to immortal non-malignant, malignant, and metastatic cell lines.

In Chapter 5, I describe Combo-NPS, a microfluidic platform for the paired measurement of surface marker expression and mechanophenotype. In this platform, the channel design consists of antibody expansion regions used to measure surface antigen expression, in addition to a downstream contraction and recovery segment used to measure cellular elasticity and recovery time. This approach enables the first moderate-throughput approach for a paired mechano- and immuno- phenotype analysis. I thoroughly describe the implementation, design, and validation of the platform, including the effect of inlet pressure on cell behavior. Next, I report unique results on immortalized breast epithelial cells, identifying correlations between surface marker expression and mechanophenotype. Finally, I demonstrate how the pair datasets can be used to screen heterogeneous cell populations, such as the luminal and myoepithelial sub-populations in HMEC's.

6.2 Future Directions

Multi-zone visco-NPS and Combo-NPS are both flexible microfluidic platforms with potential for continued developments that improve their operation and capabilities. From an experimental perspective, the most common device failure mode is fluidic occlusion of the narrow contraction segments. The likely culprit is PDMS debris that is dislodged from the inlet hole during intubation. I hypothesize that when the holes are initially punched, small ridges form, resulting in an uneven surface at the microscopic scale. The imperfections on the inlet hole surface are then scrapped off during intubation. Further logistical improvements can be made to reduce this failure mode. Punches need to be extremely sharp in order to avoid this issue, and the punching technique needs to be extremely uniform. Specialized equipment can help achieve both requirements, such as the Accu-Punch Manual Hole Punch (Syneo). Alternative fabrication approaches can also be considered, such as 3D-printing. 3D printing has the capability to form the entire channel structure in a single process, negating the need to punch holes and adding the ability to incorporate multi-layered, vertical and horizontal channel geometries [166]. 3D printing techniques also eliminate the need for printed photo-masks, accelerating prototype iteration, at the trade-off of scalability and fabrication throughput.

When examining Multi-Zone Visco-NPS, additional characterizations, designs, and experiments could be evaluated. The primary stress model, described in Section 4.3.2, can be further refined. The current model assumes a constant pressure driving force based on COMSOL® simulations, and a cylindrical deformation. Future models can incorporate fluidic drag as the driving force, and a "sliced-sphere" pancake deformation to better model real-world conditions. Furthermore, the incorporation of advanced fluid-structure interaction simulations [260] would enable digital model tuning and validation, and could potentially provide an alternative way to quantify stress on a cell. Next, when examining resistance pulses, there is often cross-talk between the zones, i.e. artifacts of a resistance pulse in one zone is visible in another zones (see Figure 4.6D). Further studies examining this specific effect should be explored, addressing: when does this effect occur, is it voltage or zone dependent, and does it bias the zone measurements in a predictable manner. Advanced simulations of the electric field during a cell transit event can also be used to examine this cross-talk effect. From a geometric perspective, future device designs can incorporate a larger magnitude change between the frequencies applied in each zone. The current designs probe at low frequencies over a single order of magnitude (about 1 to 100 hz). At these low frequencies, elastic behavior dominates. However, at high frequencies, the viscous behavior dominates. Probing cells at these frequencies could reveal more information about how the cell behaves during rapid processes. Increasing the strain frequency in each zone would require longer zone lengths. However, the 6mm zone designs tested and described in Section 4.5 already reach the maximum extents of the glass substrate. A serpentine design could be evaluated to allow for longer zones, or the use of a larger glass substrate. Finally, improvements could be made to the data analysis approach. Machine learning (ML) models could be trained

on the sinusoidal signals, improving signal parsing and allowing for signal features to be directly learned [261]. This would negate the need for a complex theoretical stress model, and instead focus on classification based on hidden signal features [262].

Likewise, the Combo-NPS approach described in this dissertation represents just the beginning of a unique multi-modal platform. Immediate next steps include the incorporation of more than two antibody expansion regions. A third antibody expansion region could greatly improve antigen screening by enabling an additional pairwise comparison on surface marker expression. Furthermore, longer antibody expansion regions could be explored. This would improve measurement sensitivity by increasing the transient interaction time each cell has with the surface antibodies. Finally, the immobilization of antibodies not just on the glass surface, but also on the PDMS walls could be explored. Again, this would improve measurement sensitivity by increasing the probability of interaction between immobilized antibodies and a transiting cells. Using commercially available crosslinkers, such as PAcrAm (SuSoS AG) [263], the PDMS surface could be fictionalized with oligos, enabling a similar DNA-directed patterning approach of surface antibody immobilization.

Lastly, a broad future direction to consider is the further miniaturization and integration of the fluidic channel with the electronic hardware. The multi-zone hardware (see section 3.4) led in this direction by integrating bench-top amplifiers and power supplies directly into the PCB architecture, vastly reducing the hardware footprint when compared to previous NPS set-ups [132, 159, 173, 264]. The footprint can be further be reduced using custom integrated-circuit (IC) components that interface directly with the microfluidic channel, creating an all-in-one chip [265] that requires only a single external pump for pressure-drive flow. Reducing hardware complexity can improve device accessibility, improving adoption in labs with limited microfluidic infrastructure and knowledge. Furthermore, the use of IC chips have the added benefit of improving SNR [266], as the components can be tailored for an NPS application. Beyond hardware improvements, more user-friendly software can also be used for data acquisition and real-time processing. The current command-line based scripts [173, 267] can again hinder accessibility. Intuitive graphical interfaces can be implemented to further reduce adoption barriers.

6.3 Concluding Remarks

This dissertation describes two unique microfluidic tools for biomedical research. As described in Chapter 1, the development of new tools form the bedrock of scientific research advancement. Here, I described Multi-Zone Visco-NPS, a tool that enables the viscoelastic measurement of single-cells in an approach that is faster than conventional methods. I use it to probe the viscoelastic properties of breast epithelial cells, uncovering the mechanical differences between cells ranging from non-malignant to high-risk. Furthermore, I also described Combo-NPS, a first-of-its-kind tool for ascertaining both the mechano- and immunophenotyping of a cell in a single, simultaneous measurement. This platform enables a paired

analysis of surface marker expression and biomechanical properties, opening up new applications in cell screening, subpopulation identification, and correlation studies between surface marker expression and mechanophenotype. The tools presented and described in this dissertation contribute to, and advance the, single-cell measurement capabilities present in the biomedical research field. Multi-Zone Visco-NPS and Combo-NPS set a new baseline for the development of future NPS technologies.

References

[1] Karthik R Balakrishnan et al. "Node-pore sensing: A robust, high-dynamic range method for detecting biological species". In: *Lab on a Chip* 13.7 (2013), pp. 1302–1307. ISSN: 14730189. DOI: 10.1039/c3lc41286e. URL: www.rsc.org/loc (visited on 07/14/2020).

[2] Albert Folch i Folch. *Hidden in plain sight: the history, science, and engineering of microfluidic technology*. eng. Cambridge, Massachusetts: The MIT press, 2022. ISBN: 978-0-262-04689-3.

[3] Katarzyna M. Koczula and Andrea Gallotta. "Lateral flow assays". In: *Essays in Biochemistry* 60.1 (June 2016). Ed. by Pedro Estrela, pp. 111–120. ISSN: 0071-1365. DOI: 10.1042/EBC20150012. URL: https://doi.org/10.1042/EBC20150012 (visited on 05/02/2024).

[4] Jobie Budd et al. "Lateral flow test engineering and lessons learned from COVID-19". en. In: *Nature Reviews Bioengineering* 1.1 (Jan. 2023). Publisher: Nature Publishing Group, pp. 13–31. ISSN: 2731-6092. DOI: 10.1038/s44222-022-00007-3. URL: https://www.nature.com/articles/s44222-022-00007-3 (visited on 05/02/2024).

[5] Xin Han et al. "Microfluidic design in single-cell sequencing and application to cancer precision medicine". In: *Cell Reports Methods* 3.9 (Sept. 2023), p. 100591. ISSN: 2667-2375. DOI: 10.1016/j.crmeth.2023.100591. URL: https://www.sciencedirect.com/science/article/pii/S2667237523002436 (visited on 05/02/2024).

[6] Shih-Mo Yang et al. "Microfluidic Point-of-Care (POC) Devices in Early Diagnosis: A Review of Opportunities and Challenges". en. In: *Sensors* 22.4 (Jan. 2022). Number: 4 Publisher: Multidisciplinary Digital Publishing Institute, p. 1620. ISSN: 1424-8220. DOI: 10.3390/s22041620. URL: https://www.mdpi.com/1424-8220/22/4/1620 (visited on 05/02/2024).

[7] Shivangi Sachdeva, Ronald W. Davis, and Amit K. Saha. "Microfluidic Point-of-Care Testing: Commercial Landscape and Future Directions". English. In: *Frontiers in Bioengineering and Biotechnology* 8 (Jan. 2021). Publisher: Frontiers. ISSN: 2296-4185. DOI: 10.3389/fbioe.2020.602659. URL: https://www.frontiersin.org/articles/10.3389/fbioe.2020.602659 (visited on 05/02/2024).

[8] Samaneh Mashaghi et al. "Droplet microfluidics: A tool for biology, chemistry and nanotechnology". In: *TrAC Trends in Analytical Chemistry* 82 (Sept. 2016), pp. 118–125. ISSN: 0165-9936. DOI: 10.1016/j.trac.2016.05.019. URL: https://www.sciencedirect.com/science/article/pii/S0165993616300061 (visited on 03/26/2024).

[9] Stefania Torino et al. "Microfluidic technology for cell hydrodynamic manipulation". en. In: *AIMS Biophysics* 4.2 (2017). Cc_license_type: cc_by Primary_atype: AIMS Biophysics Subject_term: Review Subject_term_id: Review, pp. 178–191. ISSN: 2377-9098. DOI: 10.3934/biophy.2017.2.178. URL: http://www.aimspress.com/rticle/doi/10.3934/biophy.2017.2.178 (visited on 03/26/2024).

[10] Sangeeta N. Bhatia and Donald E. Ingber. "Microfluidic organs-on-chips". en. In: *Nature Biotechnology* 32.8 (Aug. 2014). Publisher: Nature Publishing Group, pp. 760–772. ISSN: 1546-1696. DOI: 10.1038/nbt.2989. URL: https://www.nature.com/articles/nbt.2989 (visited on 03/26/2024).

[11] Henrik Bruus. "Governing Equations in Microfluidics". en. In: *Microscale Acoustofluidics*. Ed. by Thomas Laurell and Andreas Lenshof. The Royal Society of Chemistry, Dec. 2014, pp. 1–28. ISBN: 978-1-84973-671-8 978-1-78262-351-9 978-1-84973-706-7. DOI: 10.1039/9781849737067-00001. URL: https://books.rsc.org/books/book/1076/chapter/901085/Governing-Equations-in-Microfluidics (visited on 03/27/2024).

[12] Mohamed Gad-el-Hak. "Liquids: The holy grail of microfluidic modeling". In: *Physics of Fluids* 17.10 (Oct. 2005), p. 100612. ISSN: 1070-6631. DOI: 10.1063/1.1897009. URL: https://doi.org/10.1063/1.1897009 (visited on 05/02/2024).

[13] Patrick Tabeling. "Hydrodynamics of microfluidics 1: channels". In: *Introduction to Microfluidics*. Ed. by Patrick Tabeling. Oxford University Press, July 2023, p. 0. ISBN: 978-0-19-284530-6. DOI: 10.1093/oso/9780192845306.003.0003. URL: https://doi.org/10.1093/oso/9780192845306.003.0003 (visited on 05/02/2024).

[14] Ellis Meng. *Biomedical microsystems*. eng. Boca Raton, Fla. London: CRC Press, 2011. ISBN: 978-1-4200-5122-3.

[15] Albert Folch. *Introduction to bioMEMS*. Boca Raton: CRC Press, 2013. ISBN: 978-1-4398-1839-8.

[16] U.S. Department of Energy. "Laminar and Turbulent Flow". In: *DOE Fundamentals Handbook: Thermodynamics, Heat Transfer, and Fluid Flow*. DOE-HDBK-1012/3-92. June 1992. URL: https://engineeringlibrary.org/reference/laminar-and-turbulent-fluid-flow-doe-handbook (visited on 05/04/2024).

[17] *COMSOL Multiphysics®*. URL: www.comsol.com.

[18] B. E. Launder and D. B. Spalding. "The numerical computation of turbulent flows". In: *Computer Methods in Applied Mechanics and Engineering* 3.2 (Mar. 1974), pp. 269–289. ISSN: 0045-7825. DOI: 10.1016/0045-7825(74)90029-2. URL: https://www.sciencedirect.com/science/article/pii/0045782574900292 (visited on 05/02/2024).

[19] Jing Fan et al. "Chapter 3 - Diffusion and mixing in microfluidic devices". In: *Microfluidics for Pharmaceutical Applications*. Ed. by Hélder A. Santos, Dongfei Liu, and Hongbo Zhang. Micro and Nano Technologies. William Andrew Publishing, Jan. 2019, pp. 79–100. ISBN: 978-0-12-812659-2. DOI: 10.1016/B978-0-12-812659-2.00003-X. URL: https://www.sciencedirect.com/science/article/pii/B978012812659200003X (visited on 03/27/2024).

[20] Andreas Baer et al. "The Stokes–Einstein–Sutherland Equation at the Nanoscale Revisited". en. In: *Small* 20.6 (2024), p. 2304670. ISSN: 1613-6829. DOI: 10.1002/smll.202304670. URL: https://onlinelibrary.wiley.com/doi/abs/10.1002/smll.202304670 (visited on 05/02/2024).

[21] Wilfred D. Stein. *Channels, Carriers, and Pumps: An Introduction to Membrane Transport*. en. Google-Books-ID: 1PWnuvCQza4C. Elsevier, Dec. 2012. ISBN: 978-0-323-13815-4.

[22] Patrice Bacchin, Jacques Leng, and Jean-Baptiste Salmon. "Microfluidic Evaporation, Pervaporation, and Osmosis: From Passive Pumping to Solute Concentration". In: *Chemical Reviews* 122.7 (Apr. 2022). Publisher: American Chemical Society, pp. 6938–6985. ISSN: 0009-2665. DOI: 10.1021/acs.chemrev.1c00459. URL: https://doi.org/10.1021/acs.chemrev.1c00459 (visited on 03/27/2024).

[23] Ayokunle Olanrewaju et al. "Capillary microfluidics in microchannels: from microfluidic networks to capillaric circuits". en. In: *Lab on a Chip* 18.16 (2018). Publisher: Royal Society of Chemistry, pp. 2323–2347. DOI: 10.1039/C8LC00458G. URL: https://pubs.rsc.org/en/content/articlelanding/2018/lc/c8lc00458g (visited on 03/27/2024).

[24] Dongqing Li. *Electrokinetics in microfluidics*. eng. Interface science and technology series 2. Amsterdam Boston Heidelberg: Elsevier-Academic Press, 2004. ISBN: 978-0-12-088444-5.

[25] Charles N. Baroud. "Thermocapillarity". en. In: *Encyclopedia of Microfluidics and Nanofluidics*. Ed. by Dongqing Li. Boston, MA: Springer US, 2013, pp. 1–7. ISBN: 978-3-642-27758-0. DOI: 10.1007/978-3-642-27758-0_1567-4. URL: https://doi.org/10.1007/978-3-642-27758-0_1567-4 (visited on 03/27/2024).

[26] Michael V. D'Ambrosio et al. "Point-of-care quantification of blood-borne filarial parasites with a mobile phone microscope". In: *Science Translational Medicine* 7.286 (May 2015). Publisher: American Association for the Advancement of Science, 286re4–

286re4. DOI: 10.1126/scitranslmed.aaa3480. URL: https://www.science.org/doi/10.1126/scitranslmed.aaa3480 (visited on 05/02/2024).

[27] Sammer-ul Hassan et al. "Capillary-Driven Flow Microfluidics Combined with Smartphone Detection: An Emerging Tool for Point-of-Care Diagnostics". en. In: *Diagnostics* 10.8 (Aug. 2020). Number: 8 Publisher: Multidisciplinary Digital Publishing Institute, p. 509. ISSN: 2075-4418. DOI: 10.3390/diagnostics10080509. URL: https://www.mdpi.com/2075-4418/10/8/509 (visited on 05/02/2024).

[28] Shiquan Lin, Xiangyu Chen, and Zhong Lin Wang. "Electron transfer in liquid–solid contact electrification and double-layer formation". In: *Encyclopedia of Solid-Liquid Interfaces (First Edition)*. Ed. by Klaus Wandelt and Gianlorenzo Bussetti. Oxford: Elsevier, Jan. 2024, pp. 576–599. ISBN: 978-0-323-85670-6. DOI: 10.1016/B978-0-323-85669-0.00142-2. URL: https://www.sciencedirect.com/science/article/pii/B9780323856690001422 (visited on 05/02/2024).

[29] Xiaowen Ou et al. "Microfluidic chip electrophoresis for biochemical analysis". eng. In: *Journal of Separation Science* 43.1 (Jan. 2020), pp. 258–270. ISSN: 1615-9314. DOI: 10.1002/jssc.201900758.

[30] Graham Kemp. "Capillary Electrophoresis". en. In: *Biotechnology and Applied Biochemistry* 27.1 (1998). _eprint: https://onlinelibrary.wiley.com/doi/pdf/10.1111/j.1470-8744.1998.tb01369.x, pp. 9–17. ISSN: 1470-8744. DOI: 10.1111/j.1470-8744.1998.tb01369.x. URL: https://onlinelibrary.wiley.com/doi/abs/10.1111/j.1470-8744.1998.tb01369.x (visited on 03/28/2024).

[31] Jitendra N. Mehrishi and Johann Bauer. "Electrophoresis of cells and the biological relevance of surface charge". en. In: *ELECTROPHORESIS* 23.13 (2002), pp. 1984–1994. ISSN: 1522-2683. DOI: 10.1002/1522-2683(200207)23:13<1984::AID-ELPS1984>3.0.CO;2-U. URL: https://onlinelibrary.wiley.com/doi/abs/10.1002/1522-2683%28200207%2923%3A13%3C1984%3A%3AAID-ELPS1984%3E3.0.CO%3B2-U (visited on 03/28/2024).

[32] Richard B. M. Schasfoort et al. "Field-Effect Flow Control for Microfabricated Fluidic Networks". In: *Science* 286.5441 (Oct. 1999). Publisher: American Association for the Advancement of Science, pp. 942–945. DOI: 10.1126/science.286.5441.942. URL: https://www.science.org/doi/10.1126/science.286.5441.942 (visited on 03/28/2024).

[33] Anton Enders, Alexander Grünberger, and Janina Bahnemann. "Towards Small Scale: Overview and Applications of Microfluidics in Biotechnology". en. In: *Molecular Biotechnology* (Dec. 2022). ISSN: 1559-0305. DOI: 10.1007/s12033-022-00626-6. URL: https://doi.org/10.1007/s12033-022-00626-6 (visited on 01/19/2024).

[34] Neil Convery and Nikolaj Gadegaard. "30 Years of Microfluidics". In: *Micro and Nano Engineering* 2.January (2019), pp. 76–91. ISSN: 25900072. DOI: 10.1016/j.mne.2019.01.003.

[35] Aaron M Streets and Yanyi Huang. "Chip in a lab: Microfluidics for next generation life science research". In: *Biomicrofluidics Journal of Rheology Journal of Vacuum Science & Technology A: Vacuum, Surfaces, and Films* 7.10 (2013). DOI: 10.1122/1.549513doi.org/10.1063/1.4789751. URL: https://doi.org/10.1063/1.4789751 (visited on 01/31/2018).

[36] Skarphedinn Halldorsson et al. "Advantages and challenges of microfluidic cell culture in polydimethylsiloxane devices". In: *Biosensors and Bioelectronics* 63 (Jan. 2015), pp. 218–231. ISSN: 0956-5663. DOI: 10.1016/j.bios.2014.07.029. URL: https://www.sciencedirect.com/science/article/pii/S0956566314005302 (visited on 05/02/2024).

[37] M A Unger et al. "Monolithic microfabricated valves and pumps by multilayer soft lithography." In: *Science (New York, N.Y.)* 288.5463 (Apr. 2000). Publisher: American Association for the Advancement of Science, pp. 113–116. ISSN: 0036-8075. DOI: 10.1126/SCIENCE.288.5463.113. URL: http://www.ncbi.nlm.nih.gov/pubmed/10753110 (visited on 01/31/2018).

[38] Paola De Stefano, Elena Bianchi, and Gabriele Dubini. "The impact of microfluidics in high-throughput drug-screening applications". In: *Biomicrofluidics* 16.3 (May 2022), p. 031501. ISSN: 1932-1058. DOI: 10.1063/5.0087294. URL: https://doi.org/10.1063/5.0087294 (visited on 05/02/2024).

[39] Mushtaq Ali, Woohyuk Kim, and Jinsoo Park. "Droplet microfluidic technologies for next-generation high-throughput screening". English. In: *Frontiers in Lab on a Chip Technologies* 2 (July 2023). Publisher: Frontiers. ISSN: 2813-3862. DOI: 10.3389/frlct.2023.1230791. URL: https://www.frontiersin.org/articles/10.3389/frlct.2023.1230791 (visited on 05/02/2024).

[40] Katharina F. Sonnen and Christoph A. Merten. "Microfluidics as an Emerging Precision Tool in Developmental Biology". In: *Developmental Cell* 48.3 (Feb. 2019), pp. 293–311. ISSN: 1534-5807. DOI: 10.1016/j.devcel.2019.01.015. URL: https://www.sciencedirect.com/science/article/pii/S1534580719300152 (visited on 05/02/2024).

[41] Jessica Melin and Stephen R. Quake. "Microfluidic large-scale integration: the evolution of design rules for biological automation". eng. In: *Annual Review of Biophysics and Biomolecular Structure* 36 (2007), pp. 213–231. ISSN: 1056-8700. DOI: 10.1146/annurev.biophys.36.040306.132646.

[42] Wen-min Zhou et al. "Microfluidics applications for high-throughput single cell sequencing". In: *Journal of Nanobiotechnology* 19.1 (Oct. 2021), p. 312. ISSN: 1477-3155. DOI: 10.1186/s12951-021-01045-6. URL: https://doi.org/10.1186/s12951-021-01045-6 (visited on 04/02/2024).

[43] Aaron M. Streets et al. "Microfluidic single-cell whole-transcriptome sequencing". In: *Proceedings of the National Academy of Sciences* 111.19 (May 2014). arXiv: 1408.1149 Publisher: National Academy of Sciences ISBN: 0027-8424, pp. 7048–7053. ISSN: 0027-8424. DOI: 10.1073/pnas.1402030111. URL: http://www.ncbi.nlm.nih.gov/pubmed/24782542 (visited on 08/20/2018).

[44] Adam K White et al. "High-throughput microfluidic single-cell RT-qPCR". In: *Proceedings of the National Academy of Sciences* 108.34 (Aug. 2011). Publisher: National Academy of Sciences ISBN: 1091-6490 (Electronic)\r0027-8424 (Linking), pp. 13999–14004. ISSN: 0027-8424. DOI: 10.1073/pnas.1019446108. URL: http://www.ncbi.nlm.nih.gov/pubmed/21808033 (visited on 08/20/2018).

[45] Umut A. Gurkan et al. "Next generation microfluidics: fulfilling the promise of lab-on-a-chip technologies". en. In: *Lab on a Chip* 24.7 (2024). Publisher: Royal Society of Chemistry, pp. 1867–1874. DOI: 10.1039/D3LC00796K. URL: https://pubs.rsc.org/en/content/articlelanding/2024/lc/d3lc00796k (visited on 05/02/2024).

[46] Hoang-Tuan Nguyen et al. "Low-Cost, Accessible Fabrication Methods for Microfluidics Research in Low-Resource Settings". en. In: *Micromachines* 9.9 (Sept. 2018). Number: 9 Publisher: Multidisciplinary Digital Publishing Institute, p. 461. ISSN: 2072-666X. DOI: 10.3390/mi9090461. URL: https://www.mdpi.com/2072-666X/9/9/461 (visited on 05/02/2024).

[47] Brian D. Iverson and Suresh V. Garimella. "Recent advances in microscale pumping technologies: a review and evaluation". en. In: *Microfluidics and Nanofluidics* 5.2 (Aug. 2008), pp. 145–174. ISSN: 1613-4990. DOI: 10.1007/s10404-008-0266-8. URL: https://doi.org/10.1007/s10404-008-0266-8 (visited on 05/02/2024).

[48] Valerio Francesco Annese and Chunxiao Hu. "Integrating Microfluidics and Electronics in Point-of-Care Diagnostics: Current and Future Challenges". en. In: *Micromachines* 13.11 (Nov. 2022). Number: 11 Publisher: Multidisciplinary Digital Publishing Institute, p. 1923. ISSN: 2072-666X. DOI: 10.3390/mi13111923. URL: https://www.mdpi.com/2072-666X/13/11/1923 (visited on 05/02/2024).

[49] Kathleen E. Bates and Hang Lu. "Optics-Integrated Microfluidic Platforms for Biomolecular Analyses". In: *Biophysical Journal* 110.8 (Apr. 2016), pp. 1684–1697. ISSN: 0006-3495. DOI: 10.1016/j.bpj.2016.03.018. URL: https://www.sciencedirect.com/science/article/pii/S0006349516300698 (visited on 05/02/2024).

[50] Marc A Buttkewitz, Christopher Heuer, and Janina Bahnemann. "Sensor integration into microfluidic systems: trends and challenges". In: *Current Opinion in Biotechnology* 83 (Oct. 2023), p. 102978. ISSN: 0958-1669. DOI: 10.1016/j.copbio.2023.102978.

[51] Adam Sciambi and Adam R. Abate. "Accurate microfluidic sorting of droplets at 30 kHz". en. In: *Lab on a Chip* 15.1 (Dec. 2014). Publisher: The Royal Society of Chemistry, pp. 47–51. ISSN: 1473-0189. DOI: 10.1039/C4LC01194E. URL: https://pubs.rsc.org/en/content/articlelanding/2015/lc/c4lc01194e (visited on 04/02/2024).

[52] William E. Arter et al. "Microfluidic approaches for the analysis of protein–protein interactions in solution". en. In: *Biophysical Reviews* 12.2 (Apr. 2020), pp. 575–585. ISSN: 1867-2469. DOI: 10.1007/s12551-020-00679-4. URL: https://doi.org/10.1007/s12551-020-00679-4 (visited on 04/02/2024).

[53] Hamed Amini, Wonhee Lee, and Dino Di Carlo. "Inertial microfluidic physics". In: *Lab on a Chip* 14.15 (2014), pp. 2739–2761. ISSN: 14730189. DOI: 10.1039/c4lc00128a.

[54] Ga Yeong Kim, Jong In Han, and Je Kyun Park. "Inertial Microfluidics-Based Cell Sorting". In: *Biochip Journal* 12.4 (2018), pp. 257–267. ISSN: 20927843. DOI: 10.1007/s13206-018-2401-2.

[55] Maximilian Grösche et al. "Microfluidic Chips for Life Sciences-A Comparison of Low Entry Manufacturing Technologies". eng. In: *Small (Weinheim an Der Bergstrasse, Germany)* 15.35 (Aug. 2019), e1901956. ISSN: 1613-6829. DOI: 10.1002/smll.201901956.

[56] Mazher Iqbal Mohammed, Steven Haswell, and Ian Gibson. "Lab-on-a-chip or Chip-in-a-lab: Challenges of Commercialization Lost in Translation". In: *Procedia Technology*. Proceedings of The 1st International Design Technology Conference 20 (Jan. 2015), pp. 54–59. ISSN: 2212-0173. DOI: 10.1016/j.protcy.2015.07.010. URL: https://www.sciencedirect.com/science/article/pii/S2212017315001875 (visited on 05/02/2024).

[57] Jonathan M. Cooper. "Challenges in lab-on-a-chip technology". English. In: *Frontiers in Lab on a Chip Technologies* 1 (Sept. 2022). Publisher: Frontiers. ISSN: 2813-3862. DOI: 10.3389/frlct.2022.979398. URL: https://www.frontiersin.org/articles/10.3389/frlct.2022.979398 (visited on 05/02/2024).

[58] Sarah Battat, David A. Weitz, and George M. Whitesides. "An outlook on microfluidics: the promise and the challenge". en. In: *Lab on a Chip* 22.3 (Feb. 2022). Publisher: The Royal Society of Chemistry, pp. 530–536. ISSN: 1473-0189. DOI: 10.1039/D1LC00731A. URL: https://pubs.rsc.org/en/content/articlelanding/2022/lc/d1lc00731a (visited on 05/02/2024).

[59] Nathan K. Khosla et al. "Simplifying the complex: accessible microfluidic solutions for contemporary processes within in vitro diagnostics". en. In: *Lab on a Chip* 22.18 (Sept. 2022). Publisher: The Royal Society of Chemistry, pp. 3340–3360. ISSN: 1473-0189. DOI: 10.1039/D2LC00609J. URL: https://pubs.rsc.org/en/content/articlelanding/2022/lc/d2lc00609j (visited on 05/02/2024).

[60] Thomas Moragues et al. "Droplet-based microfluidics". en. In: *Nature Reviews Methods Primers* 3.1 (Apr. 2023). Publisher: Nature Publishing Group, pp. 1–22. ISSN: 2662-8449. DOI: 10.1038/s43586-023-00212-3. URL: https://www.nature.com/articles/s43586-023-00212-3 (visited on 05/04/2024).

[61] Luoran Shang, Yao Cheng, and Yuanjin Zhao. "Emerging Droplet Microfluidics". In: *Chemical Reviews* 117.12 (June 2017). Publisher: American Chemical Society, pp. 7964–8040. ISSN: 0009-2665. DOI: 10.1021/acs.chemrev.6b00848. URL: https://doi.org/10.1021/acs.chemrev.6b00848 (visited on 05/04/2024).

[62] Shia-Yen Teh et al. "Droplet microfluidics". en. In: *Lab on a Chip* 8.2 (Jan. 2008). Publisher: The Royal Society of Chemistry, pp. 198–220. ISSN: 1473-0189. DOI: 10.1039/B715524G. URL: https://pubs.rsc.org/en/content/articlelanding/2008/lc/b715524g (visited on 05/04/2024).

[63] Mira T. Guo et al. "Droplet microfluidics for high-throughput biological assays". en. In: *Lab on a Chip* 12.12 (May 2012). Publisher: The Royal Society of Chemistry, pp. 2146–2155. ISSN: 1473-0189. DOI: 10.1039/C2LC21147E. URL: https://pubs.rsc.org/en/content/articlelanding/2012/lc/c2lc21147e (visited on 05/02/2024).

[64] Rapolas Zilionis et al. "Single-cell barcoding and sequencing using droplet microfluidics". en. In: *Nature Protocols* 12.1 (Jan. 2017). Publisher: Nature Publishing Group, pp. 44–73. ISSN: 1750-2799. DOI: 10.1038/nprot.2016.154. URL: https://www.nature.com/articles/nprot.2016.154 (visited on 04/02/2024).

[65] Xiannian Zhang et al. "Comparative Analysis of Droplet-Based Ultra-High-Throughput Single-Cell RNA-Seq Systems". In: *Molecular Cell* 73.1 (Jan. 2019). Publisher: Cell Press, 130–142.e5. ISSN: 10974164. DOI: 10.1016/j.molcel.2018.10.020. URL: https://www.sciencedirect.com/science/article/pii/S1097276518308803#bib36 (visited on 05/07/2019).

[66] Evan Z. Macosko et al. "Highly Parallel Genome-wide Expression Profiling of Individual Cells Using Nanoliter Droplets". English. In: *Cell* 161.5 (May 2015). Publisher: Elsevier, pp. 1202–1214. ISSN: 0092-8674, 1097-4172. DOI: 10.1016/j.cell.2015.05.002. URL: https://www.cell.com/cell/abstract/S0092-8674(15)00549-8 (visited on 04/02/2024).

[67] Alec Richardson et al. "A microfluidic organotypic device for culture of mammalian intestines ex vivo". In: *Analytical Methods* (2020). Publisher: Royal Society of Chemistry, pp. 297–303. ISSN: 1759-9660. DOI: 10.1039/c9ay02038a.

[68] Tania Limongi et al. "Microfluidics for 3D Cell and Tissue Cultures: Microfabricative and Ethical Aspects Updates". en. In: *Cells* 11.10 (Jan. 2022). Number: 10 Publisher: Multidisciplinary Digital Publishing Institute, p. 1699. ISSN: 2073-4409. DOI: 10.3390/cells11101699. URL: https://www.mdpi.com/2073-4409/11/10/1699 (visited on 05/04/2024).

[69] Masoomeh Tehranirokh et al. "Microfluidic devices for cell cultivation and proliferation". In: *Biomicrofluidics* 7.5 (Oct. 2013), p. 051502. ISSN: 1932-1058. DOI: 10.1063/1.4826935. URL: https://doi.org/10.1063/1.4826935 (visited on 05/04/2024).

[70] Giovanni Marco Nocera et al. "The VersaLive platform enables microfluidic mammalian cell culture for versatile applications". en. In: *Communications Biology* 5.1 (Sept. 2022). Publisher: Nature Publishing Group, pp. 1–9. ISSN: 2399-3642. DOI: 10.1038/s42003-022-03976-8. URL: https://www.nature.com/articles/s42003-022-03976-8 (visited on 05/04/2024).

[71] Peter Loskill et al. "Organo: A Lego®-Like Plug & Play System for Modular Multi-Organ-Chips". en. In: *PLOS ONE* 10.10 (Oct. 2015). Publisher: Public Library of Science, e0139587. ISSN: 1932-6203. DOI: 10.1371/journal.pone.0139587. URL: https://journals.plos.org/plosone/article?id=10.1371/journal.pone.0139587 (visited on 04/02/2024).

[72] Chak Ming Leung et al. "A guide to the organ-on-a-chip". en. In: *Nature Reviews Methods Primers* 2.1 (May 2022). Publisher: Nature Publishing Group, pp. 1–29. ISSN: 2662-8449. DOI: 10.1038/s43586-022-00118-6. URL: https://www.nature.com/articles/s43586-022-00118-6 (visited on 04/02/2024).

[73] Elizabeth L. Doherty et al. "Microfluidic and Organ-on-a-Chip Approaches to Investigate Cellular and Microenvironmental Contributions to Cardiovascular Function and Pathology". English. In: *Frontiers in Bioengineering and Biotechnology* 9 (Feb. 2021). Publisher: Frontiers. ISSN: 2296-4185. DOI: 10.3389/fbioe.2021.624435. URL: https://www.frontiersin.org/articles/10.3389/fbioe.2021.624435 (visited on 05/04/2024).

[74] Amir Bein et al. "Microfluidic Organ-on-a-Chip Models of Human Intestine". In: *Cellular and Molecular Gastroenterology and Hepatology* 5.4 (Jan. 2018), pp. 659–668. ISSN: 2352-345X. DOI: 10.1016/j.jcmgh.2017.12.010. URL: https://www.sciencedirect.com/science/article/pii/S2352345X17301893 (visited on 05/04/2024).

[75] Johannes Dornhof et al. "Microfluidic organ-on-chip system for multi-analyte monitoring of metabolites in 3D cell cultures". en. In: *Lab on a Chip* 22.2 (Jan. 2022). Publisher: The Royal Society of Chemistry, pp. 225–239. ISSN: 1473-0189. DOI: 10.1039/D1LC00689D. URL: https://pubs.rsc.org/en/content/articlelanding/2022/lc/d1lc00689d (visited on 05/04/2024).

[76] Cody Carrell et al. "Beyond the lateral flow assay: A review of paper-based microfluidics". In: *Microelectronic Engineering* 206 (Feb. 2019), pp. 45–54. ISSN: 0167-9317. DOI: 10.1016/j.mee.2018.12.002. URL: https://www.sciencedirect.com/science/article/pii/S0167931718305069 (visited on 04/02/2024).

[77] Eka Noviana et al. "Microfluidic Paper-Based Analytical Devices: From Design to Applications". In: *Chemical Reviews* 121.19 (Oct. 2021). Publisher: American Chemical Society, pp. 11835–11885. ISSN: 0009-2665. DOI: 10.1021/acs.chemrev.0c01335. URL: https://doi.org/10.1021/acs.chemrev.0c01335 (visited on 05/04/2024).

[78] Piotr Lisowski and Paweł K. Zarzycki. "Microfluidic Paper-Based Analytical Devices (PADs) and Micro Total Analysis Systems (TAS): Development, Applications and Future Trends". en. In: *Chromatographia* 76.19 (Oct. 2013), pp. 1201–1214. ISSN: 1612-1112. DOI: 10.1007/s10337-013-2413-y. URL: https://doi.org/10.1007/s10337-013-2413-y (visited on 05/04/2024).

[79] Chao-Min Cheng et al. "Paper-Based ELISA". In: *Angewandte Chemie* 122.28 (2010). _eprint: https://onlinelibrary.wiley.com/doi/pdf/10.1002/ange.201001005, pp. 4881–4884. ISSN: 1521-3757. DOI: 10.1002/ange.201001005. URL: https://onlinelibrary.wiley.com/doi/abs/10.1002/ange.201001005 (visited on 04/02/2024).

[80] Mohit S. Verma et al. "Sliding-strip microfluidic device enables ELISA on paper". In: *Biosensors and Bioelectronics* 99 (Jan. 2018), pp. 77–84. ISSN: 0956-5663. DOI: 10.1016/j.bios.2017.07.034. URL: https://www.sciencedirect.com/science/article/pii/S0956566317304815 (visited on 05/04/2024).

[81] Gaolian Xu et al. "Paper-Origami-Based Multiplexed Malaria Diagnostics from Whole Blood". en. In: *Angewandte Chemie International Edition* 55.49 (2016), pp. 15250–15253. ISSN: 1521-3773. DOI: 10.1002/anie.201606060. URL: https://onlinelibrary.wiley.com/doi/abs/10.1002/anie.201606060 (visited on 04/02/2024).

[82] Iulia M. Lazar, Nicholas S. Gulakowski, and Alexandru C. Lazar. "Protein and Proteome Measurements with Microfluidic Chips". In: *Analytical Chemistry* 92.1 (Jan. 2020). Publisher: American Chemical Society, pp. 169–182. ISSN: 0003-2700. DOI: 10.1021/acs.analchem.9b04711. URL: https://doi.org/10.1021/acs.analchem.9b04711 (visited on 04/02/2024).

[83] Pan Zhou et al. "A Review of Optical Imaging Technologies for Microfluidics". en. In: *Micromachines* 13.2 (Feb. 2022). Number: 2 Publisher: Multidisciplinary Digital Publishing Institute, p. 274. ISSN: 2072-666X. DOI: 10.3390/mi13020274. URL: https://www.mdpi.com/2072-666X/13/2/274 (visited on 05/04/2024).

[84] Bader Al Alwan et al. "Single-molecule imaging and microfluidic platform reveal molecular mechanisms of leukemic cell rolling". en. In: *Communications Biology* 4.1 (July 2021). Publisher: Nature Publishing Group, pp. 1–14. ISSN: 2399-3642. DOI: 10.1038/s42003-021-02398-2. URL: https://www.nature.com/articles/s42003-021-02398-2 (visited on 05/04/2024).

[85] Marjorie R. Willner et al. "Surface-Enhanced Raman Scattering Based Microfluidics for Single-Cell Analysis". In: *Analytical Chemistry* 90.20 (Oct. 2018). Publisher: American Chemical Society, pp. 12004–12010. ISSN: 0003-2700. DOI: 10.1021/acs.

analchem.8b02636. URL: https://doi.org/10.1021/acs.analchem.8b02636 (visited on 05/04/2024).

[86] Philippe Abdel-Sayed et al. "Fabrication of an Open Microfluidic Device for Immunoblotting". In: *Analytical Chemistry* 89.18 (Sept. 2017). Publisher: American Chemical Society, pp. 9643–9648. ISSN: 0003-2700. DOI: 10.1021/acs.analchem.7b02406. URL: https://doi.org/10.1021/acs.analchem.7b02406 (visited on 04/02/2024).

[87] Dapeng Wu, Jianhua Qin, and Bingcheng Lin. "Electrophoretic separations on microfluidic chips". In: *Journal of Chromatography A*. 50 Years Journal of Chromatography 1184.1 (Mar. 2008), pp. 542–559. ISSN: 0021-9673. DOI: 10.1016/j.chroma.2007.11.119. URL: https://www.sciencedirect.com/science/article/pii/S0021967307021061 (visited on 05/04/2024).

[88] Yue Sun. "Chapter 4 - Microfluidic capillary electrophoresis chip techniques: theory and different separation modes". In: *Multidisciplinary Microfluidic and Nanofluidic Lab-on-a-chip*. Ed. by XiuJun (James) Li, Chaoyong Yang, and Paul C. H. Li. Amsterdam: Elsevier, Jan. 2022, pp. 99–142. ISBN: 978-0-444-59432-7. DOI: 10.1016/B978-0-444-59432-7.00002-9. URL: https://www.sciencedirect.com/science/article/pii/B9780444594327000029 (visited on 05/04/2024).

[89] Steven J. Altschuler and Lani F. Wu. "Cellular Heterogeneity: Do Differences Make a Difference?" In: *Cell* 141.4 (May 2010), pp. 559–563. ISSN: 0092-8674. DOI: 10.1016/j.cell.2010.04.033. URL: https://www.sciencedirect.com/science/article/pii/S0092867410004873 (visited on 04/02/2024).

[90] Harry Rubin. "The significance of biological heterogeneity". en. In: *Cancer and Metastasis Reviews* 9.1 (July 1990), pp. 1–20. ISSN: 1573-7233. DOI: 10.1007/BF00047585. URL: https://doi.org/10.1007/BF00047585 (visited on 05/04/2024).

[91] Albert Gough et al. "Biologically Relevant Heterogeneity: Metrics and Practical Insights". English. In: *SLAS Discovery* 22.3 (Mar. 2017). Publisher: Elsevier, pp. 213–237. ISSN: 2472-5552, 2472-5560. DOI: 10.1177/2472555216682725. URL: https://slas-discovery.org/article/S2472-5552(22)06959-3/fulltext (visited on 05/04/2024).

[92] Alexa A. Woodward et al. "Genetic heterogeneity: Challenges, impacts, and methods through an associative lens". en. In: *Genetic Epidemiology* 46.8 (2022). _eprint: https://onlinelibrary.wiley.com/doi/pdf/10.1002/gepi.22497, pp. 555–571. ISSN: 1098-2272. DOI: 10.1002/gepi.22497. URL: https://onlinelibrary.wiley.com/doi/abs/10.1002/gepi.22497 (visited on 05/04/2024).

[93] Devon A. Lawson et al. "Tumour heterogeneity and metastasis at single-cell resolution". en. In: *Nature Cell Biology* 20.12 (Dec. 2018). Publisher: Nature Publishing Group, pp. 1349–1360. ISSN: 1476-4679. DOI: 10.1038/s41556-018-0236-7. URL: https://www.nature.com/articles/s41556-018-0236-7 (visited on 05/04/2024).

[94] Niko Komin and Alexander Skupin. "How to address cellular heterogeneity by distribution biology". In: *Current Opinion in Systems Biology*. • Mathematical modelling • Mathematical modelling, Dynamics of brain activity at the systems level • Clinical and translational systems biology 3 (June 2017), pp. 154–160. ISSN: 2452-3100. DOI: 10.1016/j.coisb.2017.05.010. URL: https://www.sciencedirect.com/science/article/pii/S2452310016300427 (visited on 05/04/2024).

[95] Michael D. Slack et al. "Characterizing heterogeneous cellular responses to perturbations". In: *Proceedings of the National Academy of Sciences* 105.49 (Dec. 2008). Publisher: Proceedings of the National Academy of Sciences, pp. 19306–19311. DOI: 10.1073/pnas.0807038105. URL: https://www.pnas.org/doi/abs/10.1073/pnas.0807038105 (visited on 05/04/2024).

[96] James E. Ferrell and Eric M. Machleder. "The Biochemical Basis of an All-or-None Cell Fate Switch in Xenopus Oocytes". In: *Science* 280.5365 (May 1998). Publisher: American Association for the Advancement of Science, pp. 895–898. DOI: 10.1126/science.280.5365.895. URL: https://www-science-org.libproxy.berkeley.edu/doi/10.1126/science.280.5365.895 (visited on 05/02/2024).

[97] L. Dennis Smith, Weilong Xu, and Robert L. Varnold. "Chapter 4 Oogenesis and Oocyte Isolation". In: *Methods in Cell Biology*. Ed. by Brian K. Kay and H. Benjamin Peng. Vol. 36. Xenopus laevis: Practical Uses in Cell and Molecular Biology. Academic Press, Jan. 1991, pp. 45–60. DOI: 10.1016/S0091-679X(08)60272-1. URL: https://www.sciencedirect.com/science/article/pii/S0091679X08602721 (visited on 05/02/2024).

[98] Lit-Hsin Loo et al. "Heterogeneity in the physiological states and pharmacological responses of differentiating 3T3-L1 preadipocytes". In: *Journal of Cell Biology* 187.3 (Oct. 2009), pp. 375–384. ISSN: 0021-9525. DOI: 10.1083/jcb.200904140. URL: https://doi.org/10.1083/jcb.200904140 (visited on 05/02/2024).

[99] Alex K. Shalek et al. "Single-cell transcriptomics reveals bimodality in expression and splicing in immune cells". en. In: *Nature* 498.7453 (June 2013). Publisher: Nature Publishing Group, pp. 236–240. ISSN: 1476-4687. DOI: 10.1038/nature12172. URL: https://www.nature.com/articles/nature12172 (visited on 05/02/2024).

[100] Joachim Roth and Clark M. Blatteis. "Mechanisms of Fever Production and Lysis: Lessons from Experimental LPS Fever". en. In: *Comprehensive Physiology*. _eprint: https://onlinelibrary.wiley.com/doi/pdf/10.1002/cphy.c130033. John Wiley & Sons, Ltd, 2014, pp. 1563–1604. ISBN: 978-0-470-65071-4. DOI: 10.1002/cphy.c130033. URL: https://onlinelibrary.wiley.com/doi/abs/10.1002/cphy.c130033 (visited on 05/02/2024).

[101] Chenxu Zhu, Sebastian Preissl, and Bing Ren. "Single-cell multimodal omics: the power of many". en. In: *Nature Methods* 17.1 (Jan. 2020). Number: 1 Publisher: Nature Publishing Group, pp. 11–14. ISSN: 1548-7105. DOI: 10.1038/s41592-019-

0691-5. URL: https://www.nature.com/articles/s41592-019-0691-5 (visited on 01/15/2024).

[102] Nicolas Altemose et al. "uDamID: A microfluidic approach for imaging and sequencing protein-DNA interactions in single cells". In: *bioRxiv* (July 2019). Publisher: Cold Spring Harbor Laboratory, p. 706903. ISSN: 2692-8205. DOI: 10.1101/706903. (Visited on 10/06/2019).

[103] Manuel Doblaré and José Merodio. "AN INTRODUCTION TO BIOMECHANICS AND MECHANOBIOLOGY". en. In: ().

[104] Lina Alhalhooly et al. "Dynamic cellular biomechanics in responses to chemotherapeutic drug in hypoxia probed by atomic force spectroscopy". en. In: *Oncotarget* 12.12 (June 2021). Publisher: Impact Journals, pp. 1165–1177. ISSN: 1949-2553. DOI: 10.18632/oncotarget.27974. URL: https://www.oncotarget.com/article/27974/text/ (visited on 05/02/2024).

[105] Chiara Argentati et al. "Insight into mechanobiology: How stem cells feel mechanical forces and orchestrate biological functions". In: *International Journal of Molecular Sciences* 20.21 (Oct. 2019). Publisher: MDPI AG, p. 5337. ISSN: 14220067. DOI: 10.3390/ijms20215337. URL: https://www.mdpi.com/1422-0067/20/21/5337 (visited on 05/26/2020).

[106] Charlotte Alibert, Bruno Goud, and Jean Baptiste Manneville. "Are cancer cells really softer than normal cells?" In: *Biology of the Cell* 109.5 (2017), pp. 167–189. ISSN: 1768322X. DOI: 10.1111/boc.201600078.

[107] Subra Suresh. "Biomechanics and biophysics of cancer cells". In: *Acta Biomaterialia* 3.4 (2007), pp. 413–438. ISSN: 17427061. DOI: 10.1016/j.actbio.2007.04.002.

[108] Gaël Runel et al. "Biomechanical Properties of Cancer Cells". In: *Cells* 10.4 (2021), pp. 1–14. ISSN: 20734409. DOI: 10.3390/cells10040887.

[109] Hadi T. Nia, Lance L. Munn, and Rakesh K. Jain. "Physical traits of cancer". In: *Science* 370.6516 (2020). ISSN: 10959203. DOI: 10.1126/SCIENCE.AAZ0868.

[110] Sanjay Kumar and Valerie M. Weaver. "Mechanics, malignancy, and metastasis: The force journey of a tumor cell". In: *Cancer and Metastasis Reviews* 28.1-2 (2009), pp. 113–127. ISSN: 01677659. DOI: 10.1007/s10555-008-9173-4.

[111] Tony Fischer, Alexander Hayn, and Claudia Tanja Mierke. "Effect of Nuclear Stiffness on Cell Mechanics and Migration of Human Breast Cancer Cells". In: *Frontiers in Cell and Developmental Biology* 8.May (2020), pp. 1–18. ISSN: 2296634X. DOI: 10.3389/fcell.2020.00393.

[112] Josette M. Northcott et al. "Feeling stress: The mechanics of cancer progression and aggression". In: *Frontiers in Cell and Developmental Biology* 6.FEB (2018), pp. 1–12. ISSN: 2296634X. DOI: 10.3389/fcell.2018.00017.

[113] Cheng Zhu, Gang Bao, and Ning Wang. "Cell mechanics: Mechanical response, cell adhesion, and molecular deformation". In: *Annual Review of Biomedical Engineering* 2.2000 (2000), pp. 189–226. ISSN: 15239829. DOI: 10.1146/annurev.bioeng.2.1.189.

[114] Luke MacQueen, Yu Sun, and Craig A. Simmons. "Mesenchymal stem cell mechanobiology and emerging experimental platforms". In: *Journal of the Royal Society Interface* 10.84 (July 2013). Publisher: Royal Society. ISSN: 17425662. DOI: 10.1098/rsif.2013.0179. (Visited on 05/26/2020).

[115] Jochen Guck and Edwin R. Chilvers. "Mechanics meets medicine". In: *Science Translational Medicine* 5.212 (2013), pp. 3–6. ISSN: 19466234. DOI: 10.1126/scitranslmed.3007731.

[116] Jan Rother et al. "Atomic force microscopy-based microrheology reveals significant differences in the viscoelastic response between malign and benign cell lines". In: *Open Biology* 4.MAY (2014). ISSN: 20462441. DOI: 10.1098/rsob.140046.

[117] Blanca González-Bermúdez, Gustavo V. Guinea, and Gustavo R. Plaza. "Advances in Micropipette Aspiration: Applications in Cell Biomechanics, Models, and Extended Studies". In: *Biophysical Journal* 116.4 (2019), pp. 587–594. ISSN: 15420086. DOI: 10.1016/j.bpj.2019.01.004.

[118] Patricia M. Davidson et al. "High-throughput microfluidic micropipette aspiration device to probe time-scale dependent nuclear mechanics in intact cells". In: *Lab on a Chip* 19.21 (2019), pp. 3652–3663. ISSN: 14730189. DOI: 10.1039/c9lc00444k.

[119] Oleg Lunov, Svetlana Bespalova, and Vitalii Zablotskii. "A model for magnetic bead microrheometry". In: *Journal of Magnetism and Magnetic Materials*. Proceedings of the Sixth International Conference on the Scientific and Clinical Applications of Magnetic Carriers 311.1 (Apr. 2007), pp. 162–165. ISSN: 0304-8853. DOI: 10.1016/j.jmmm.2006.10.1172. URL: https://www.sciencedirect.com/science/article/pii/S0304885306025686 (visited on 05/02/2024).

[120] Eric M. Furst and Todd M. Squires. "Magnetic bead microrheology". In: *Microrheology*. Ed. by Eric M. Furst and Todd M. Squires. Oxford University Press, Oct. 2017, p. 0. ISBN: 978-0-19-965520-5. DOI: 10.1093/oso/9780199655205.003.0008. URL: https://doi.org/10.1093/oso/9780199655205.003.0008 (visited on 05/02/2024).

[121] Jochen Guck et al. "The optical stretcher: A novel laser tool to micromanipulate cells". In: *Biophysical Journal* 81.2 (2001). ISBN: 5124757647, pp. 767–784. ISSN: 00063495. DOI: 10.1016/S0006-3495(01)75740-2.

[122] Bryan Lincoln et al. "High-Throughput Rheological Measurements with an Optical Stretcher". In: *Methods in Cell Biology* 83.07 (2007). ISBN: 0123705002, pp. 397–423. ISSN: 0091679X. DOI: 10.1016/S0091-679X(07)83017-2.

[123] Tie Yang, Francesca Bragheri, and Paolo Minzioni. "A comprehensive review of optical stretcher for cell mechanical characterization at single-cell level". In: *Micromachines* 7.5 (2016), pp. 1–30. ISSN: 2072666X. DOI: 10.3390/mi7050090.

[124] Christian Ganser and Takayuki Uchihashi. "Measuring mechanical properties with high-speed atomic force microscopy". In: *Microscopy* 73.1 (Feb. 2024), pp. 14–21. ISSN: 2050-5701. DOI: 10.1093/jmicro/dfad051. URL: https://doi.org/10.1093/jmicro/dfad051 (visited on 05/02/2024).

[125] Molly Kozminsky and Lydia L. Sohn. "The promise of single-cell mechanophenotyping for clinical applications". In: *Biomicrofluidics* 14.3 (2020). Publisher: AIP Publishing LLC. ISSN: 19321058. DOI: 10.1063/5.0010800.

[126] Pei Hsun Wu et al. "A comparison of methods to assess cell mechanical properties". In: *Nature Methods* 15.7 (2018). Publisher: Springer US. ISSN: 15487105. DOI: 10.1038/s41592-018-0015-1. URL: http://dx.doi.org/10.1038/s41592-018-0015-1.

[127] Dino Di Carlo. "A mechanical biomarker of cell state in medicine". In: *Journal of Laboratory Automation* 17.1 (2012), pp. 32–42. ISSN: 22110682. DOI: 10.1177/2211068211431630.

[128] Daniel R. Gossett et al. "Hydrodynamic stretching of single cells for large population mechanical phenotyping". In: *Proceedings of the National Academy of Sciences of the United States of America* 109.20 (2012), pp. 7630–7635. ISSN: 00278424. DOI: 10.1073/pnas.1200107109.

[129] Josephine Shaw Bagnall et al. "Deformability of Tumor Cells versus Blood Cells". In: *Scientific Reports* 5.July (2015). Publisher: Nature Publishing Group, pp. 1–11. ISSN: 20452322. DOI: 10.1038/srep18542.

[130] Simone Braig et al. "Pharmacological targeting of membrane rigidity: implications on cancer cell migration and invasion". en. In: *New Journal of Physics* 17.8 (Aug. 2015). Publisher: IOP Publishing, p. 083007. ISSN: 1367-2630. DOI: 10.1088/1367-2630/17/8/083007. URL: https://dx.doi.org/10.1088/1367-2630/17/8/083007 (visited on 05/02/2024).

[131] Kristina Haase and Andrew E. Pelling. "Investigating cell mechanics with atomic force microscopy". In: *Journal of The Royal Society Interface* 12.104 (Mar. 2015). Publisher: Royal Society, p. 20140970. DOI: 10.1098/rsif.2014.0970. URL: https://royalsocietypublishing.org/doi/10.1098/rsif.2014.0970 (visited on 05/02/2024).

[132] Junghyun Kim et al. "Characterizing cellular mechanical phenotypes with mechano-node-pore sensing". In: *Microsystems & Nanoengineering* 4.1 (2018). ISSN: 2055-7434. DOI: 10.1038/micronano.2017.91. URL: www.nature.com/micronano (visited on 05/12/2020).

[133] Xiang Ren et al. "Single-Cell Mechanical Characteristics Analyzed by Multiconstriction Microfluidic Channels". In: *ACS Sensors* 2.2 (2017), pp. 290–299. ISSN: 23793694. DOI: 10.1021/acssensors.6b00823.

[134] Ahmad Altayyeb et al. "Characterization of Mechanical Signature of Eutopic Endometrial Stromal Cells of Endometriosis Patients". en. In: *Reproductive Sciences* 27.1 (Jan. 2020), pp. 364–374. ISSN: 1933-7205. DOI: 10.1007/s43032-019-00042-3. URL: https://doi.org/10.1007/s43032-019-00042-3 (visited on 04/02/2024).

[135] Oliver Otto et al. "Real-time deformability cytometry: On-the-fly cell mechanical phenotyping". In: *Nature Methods* 12.3 (Feb. 2015). Publisher: Nature Publishing Group, pp. 199–202. ISSN: 15487105. DOI: 10.1038/nmeth.3281. (Visited on 05/26/2020).

[136] Shamim M. Ahmmed et al. "Multi-sample deformability cytometry of cancer cells". In: *APL Bioengineering* 2.3 (2018), pp. 1–14. ISSN: 24732877. DOI: 10.1063/1.5020992. URL: http://dx.doi.org/10.1063/1.5020992.

[137] Kendra D. Nyberg et al. "Quantitative Deformability Cytometry: Rapid, Calibrated Measurements of Cell Mechanical Properties". In: *Biophysical Journal* 113.7 (2017). Publisher: Biophysical Society, pp. 1574–1584. ISSN: 15420086. DOI: 10.1016/j.bpj.2017.06.073. URL: https://doi.org/10.1016/j.bpj.2017.06.073.

[138] Richard Gerum et al. "Viscoelastic properties of suspended cells measured with shear flow deformation cytometry". In: *eLife* 11 (2022), pp. 1–26. ISSN: 2050084X. DOI: 10.7554/eLife.78823.

[139] S. M. Hurtley. "Cell biology of the cytoskeleton". In: *Science* 279.5350 (1998), p. 459. ISSN: 00368075. DOI: 10.1126/science.279.5350.459a.

[140] Daniel A. Fletcher and R. Dyche Mullins. "Cell mechanics and the cytoskeleton". In: *Nature* 463.7280 (2010), pp. 485–492. ISSN: 00280836. DOI: 10.1038/nature08908.

[141] Adrian F. Pegoraro, Paul Janmey, and David A. Weitz. "Mechanical properties of the cytoskeleton and cells". In: *Cold Spring Harbor Perspectives in Biology* 9.11 (2017). ISSN: 19430264. DOI: 10.1101/cshperspect.a022038.

[142] Mohammad R. K. Mofrad and Roger D. Kamm, eds. *Cytoskeletal Mechanics: Models and Measurements in Cell Mechanics*. Cambridge Texts in Biomedical Engineering. Cambridge: Cambridge University Press, 2006. ISBN: 978-0-521-84637-0. DOI: 10.1017/CBO9780511607318. URL: https://www.cambridge.org/core/books/cytoskeletal-mechanics/3A0CA11E0B43653B67AC40466A8407DD.

[143] Viola Introini et al. "Biophysical Tools and Concepts Enable Understanding of Asexual Blood Stage Malaria". In: *Frontiers in Cellular and Infection Microbiology* 12.May (2022). ISSN: 22352988. DOI: 10.3389/fcimb.2022.908241.

[144] Tom M.J. Evers et al. "Reciprocal regulation of cellular mechanics and metabolism". In: *Nature Metabolism* 3.4 (2021). Publisher: Springer US, pp. 456–468. ISSN: 25225812. DOI: 10.1038/s42255-021-00384-w. URL: http://dx.doi.org/10.1038/s42255-021-00384-w.

[145] Andrew Massey et al. "Mechanical properties of human tumour tissues and their implications for cancer development". en. In: *Nature Reviews Physics* 6.4 (Apr. 2024). Publisher: Nature Publishing Group, pp. 269–282. ISSN: 2522-5820. DOI: 10.1038/s42254-024-00707-2. URL: https://www.nature.com/articles/s42254-024-00707-2 (visited on 05/04/2024).

[146] Douglas Hanahan and Robert A. Weinberg. "The Hallmarks of Cancer Review". In: *Cell* 100 (2000), pp. 57–70. DOI: https://doi.org/10.1016/S0092-8674(00)81683-9.

[147] Denis Wirtz, Konstantinos Konstantopoulos, and Peter C. Searson. "The physics of cancer: The role of physical interactions and mechanical forces in metastasis". In: *Nature Reviews Cancer* 11.7 (2011). Publisher: Nature Publishing Group, pp. 512–522. ISSN: 1474175X. DOI: 10.1038/nrc3080.

[148] Henry T.K. Tse et al. "Quantitative diagnosis of malignant pleural effusions by single-cell mechanophenotyping". In: *Science Translational Medicine* 5.212 (2013). ISSN: 19466234. DOI: 10.1126/scitranslmed.3006559.

[149] Marios E. Froudarakis. "Diagnostic Work-Up of Pleural Effusions". In: *Respiration* 75.1 (Jan. 2008), pp. 4–13. ISSN: 0025-7931. DOI: 10.1159/000112221. URL: https://doi.org/10.1159/000112221 (visited on 04/03/2024).

[150] Fu-Shi Quan and Kyung Sook Kim. "Medical applications of the intrinsic mechanical properties of single cells". In: *Acta Biochim Biophys Sin* 48.10 (2016), pp. 865–871. DOI: 10.1093/abbs/gmw081. URL: https://academic.oup.com/abbs/article-abstract/48/10/865/2388990 (visited on 07/26/2020).

[151] Brian Li et al. "Mechanical phenotyping reveals unique biomechanical responses in retinoic acid-resistant acute promyelocytic leukemia". In: *iScience* 25.2 (2022). Publisher: The Author(s), p. 103772. ISSN: 25890042. DOI: 10.1016/j.isci.2022.103772. URL: https://doi.org/10.1016/j.isci.2022.103772.

[152] R. W. DeBlois and C. P. Bean. "Counting and sizing of submicron particles by the resistive pulse technique". In: *Review of Scientific Instruments* 41.7 (1970), pp. 909–916. ISSN: 00346748. DOI: 10.1063/1.1684724.

[153] O. A. Saleh and L. L. Sohn. "Quantitative sensing of nanoscale colloids using a microchip Coulter counter". In: *Review of Scientific Instruments* 72.12 (2001), pp. 4449–4451. ISSN: 00346748. DOI: 10.1063/1.1419224.

[154] Omar A. Saleh and Lydia L. Sohn. "Direct detection of antibody-antigen binding using an on-chip artificial pore". In: *Proceedings of the National Academy of Sciences of the United States of America* 100.3 (2003), pp. 820–824. ISSN: 00278424. DOI: 10.1073/pnas.0337563100.

[155] Omar A. Saleh and Lydia L. Sohn. "An artificial nanopore for molecular sensing". In: *Nano Letters* 3.1 (2003), pp. 37–38. ISSN: 15306984. DOI: 10.1021/nl0255202.

[156] A. Carbonaro and L. L. Sohn. "A resistive-pulse sensor chip for multianalyte immunoassays". In: *Lab on a Chip* 5.10 (2005), pp. 1155–1160. ISSN: 14730189. DOI: 10.1039/b504827c.

[157] Omar A. Saleh and Lydia L. Sohn. "Resistive-pulse Sensing and On-chip Artificial Pores for Biological Sensing". en. In: (Sept. 2008). DOI: 10.1039/9781847558558-00060. URL: https://books.rsc.org/books/edited-volume/152/chapter/82633/Resistive-pulse-Sensing-and-On-chip-Artificial.

[158] Karthik R. Balakrishnan et al. "Node-pore sensing enables label-free surface-marker profiling of single cells". In: *Analytical Chemistry* 87.5 (2015), pp. 2988–2995. ISSN: 15206882. DOI: 10.1021/ac504613b.

[159] Junghyun Kim et al. "Visco-Node-Pore Sensing: A Microfluidic Rheology Platform to Characterize Viscoelastic Properties of Epithelial Cells". In: *iScience* 13 (Mar. 2019). Publisher: Elsevier, pp. 214–228. ISSN: 25890042. DOI: 10.1016/j.isci.2019.02.021. URL: https://www.sciencedirect.com/science/article/pii/S2589004219300550?via%3Dihub (visited on 08/30/2019).

[160] Biao Xi et al. "The application of cell-based label-free technology in drug discovery". en. In: *Biotechnology Journal* 3.4 (2008), pp. 484–495. ISSN: 1860-7314. DOI: 10.1002/biot.200800020. URL: https://onlinelibrary.wiley.com/doi/abs/10.1002/biot.200800020 (visited on 02/13/2024).

[161] Thomas R. Carey et al. "Developments in label-free microfluidic methods for single-cell analysis and sorting". In: *Wiley Interdisciplinary Reviews: Nanomedicine and Nanobiotechnology* 11.1 (Jan. 2019). Publisher: Wiley-Blackwell, e1529. ISSN: 19390041. DOI: 10.1002/wnan.1529. URL: http://doi.wiley.com/10.1002/wnan.1529 (visited on 06/20/2020).

[162] Walter R. Hogg and Wallace H. Coulter. "Apparatus and method for measuring a dividing particle size of a particulate system". US3557352A. Jan. 1971. URL: https://patents.google.com/patent/US3557352A/en (visited on 01/30/2024).

[163] Catherine J. Cox et al. "Evaluation of the Coulter Counter® Model S-Plus IV". In: *American Journal of Clinical Pathology* 84.3 (Sept. 1985), pp. 297–306. ISSN: 0002-9173. DOI: 10.1093/ajcp/84.3.297. URL: https://doi.org/10.1093/ajcp/84.3.297 (visited on 05/03/2024).

[164] H E Kubitschek and J A Friske. "Determination of bacterial cell volume with the Coulter Counter". In: *Journal of Bacteriology* 168.3 (Dec. 1986). Publisher: American Society for Microbiology, pp. 1466–1467. DOI: 10.1128/jb.168.3.1466-1467.1986. URL: https://journals.asm.org/doi/abs/10.1128/jb.168.3.1466-1467.1986 (visited on 05/03/2024).

[165] Marshall Don. Graham. "The Coulter Principle: A history". en. In: *Cytometry Part A* 101.1 (2022), pp. 8–11. ISSN: 1552-4930. DOI: 10.1002/cyto.a.24505. (Visited on 02/20/2024).

[166] Ruitao Su, Fujun Wang, and Michael C. McAlpine. "3D printed microfluidics: advances in strategies, integration, and applications". en. In: *Lab on a Chip* 23.5 (Mar. 2023). Publisher: The Royal Society of Chemistry, pp. 1279–1299. ISSN: 1473-0189. DOI: 10.1039/D2LC01177H.

[167] Krystian L. Wlodarczyk, Duncan P. Hand, and M. Mercedes Maroto-Valer. "Maskless, rapid manufacturing of glass microfluidic devices using a picosecond pulsed laser". en. In: *Scientific Reports* 9.1 (Dec. 2019). Publisher: Nature Publishing Group, p. 20215. ISSN: 2045-2322. DOI: 10.1038/s41598-019-56711-5. URL: https://www.nature.com/articles/s41598-019-56711-5 (visited on 04/03/2024).

[168] Amid Shakeri et al. "The Fabrication and Bonding of Thermoplastic Microfluidics: A Review". en. In: *Materials* 15.18 (Jan. 2022). Number: 18 Publisher: Multidisciplinary Digital Publishing Institute, p. 6478. ISSN: 1996-1944. DOI: 10.3390/ma15186478. URL: https://www.mdpi.com/1996-1944/15/18/6478 (visited on 04/03/2024).

[169] Younan Xia and George M. Whitesides. "Soft lithography". In: *Annual Review of Materials Science* 28.1 (1998), pp. 153–184. ISSN: 00846600. DOI: 10.1146/annurev.matsci.28.1.153.

[170] Andre Lai et al. "Multi-Zone Visco-NPS:Microfluidic Platform for Multi-Frequency Viscoelastic Phenotyping of Single Cells". In: *Manuscript in preparation* (2024).

[171] Aslihan Gokaltun et al. "Recent advances in nonbiofouling PDMS surface modification strategies applicable to microfluidic technology". In: *Technology* 05.01 (2017), pp. 1–12. ISSN: 2339-5478. DOI: 10.1142/s2339547817300013.

[172] Zhi Min Zhang, Shan Chen, and Yi Zeng Liang. "Baseline correction using adaptive iteratively reweighted penalized least squares". In: *Analyst* 135.5 (2010), pp. 1138–1146. ISSN: 13645528. DOI: 10.1039/b922045c.

[173] Andre Lai et al. "Mechano-Node-Pore Sensing: A Rapid, Label-Free Platform for Multi-Parameter Single-Cell Viscoelastic Measurements". In: *Journal of Visualized Experiments* 2022.190 (2022), pp. 1–22. ISSN: 1940087X. DOI: 10.3791/64665.

[174] Jordi Alcaraz et al. "Microrheology of human lung epithelial cells measured by atomic force microscopy". In: *Biophysical Journal* 84.3 (2003), pp. 2071–2079. ISSN: 00063495. DOI: 10.1016/S0006-3495(03)75014-0.

[175] Falk Wottawah et al. "Optical rheology of biological cells". In: *Physical Review Letters* 94.9 (2005), pp. 1–4. ISSN: 00319007. DOI: 10.1103/PhysRevLett.94.098103.

[176] Jochen Guck et al. "Optical deformability as an inherent cell marker for testing malignant transformation and metastatic competence". In: *Biophysical Journal* 88.5 (2005), pp. 3689–3698. ISSN: 00063495. DOI: 10.1529/biophysj.104.045476.

[177] Yareni A. Ayala et al. "Rheological properties of cells measured by optical tweezers". In: *BMC Biophysics* 9.1 (2016). Publisher: BMC Biophysics, pp. 1–11. ISSN: 20461682. DOI: 10.1186/s13628-016-0031-4. URL: http://dx.doi.org/10.1186/s13628-016-0031-4.

[178] Eric M. Darling and Dino Di Carlo. "High-Throughput Assessment of Cellular Mechanical Properties". In: *Annual Review of Biomedical Engineering* 17.1 (Dec. 2015). Publisher: Annual Reviews, pp. 35–62. ISSN: 1523-9829. DOI: 10.1146/annurev-bioeng-071114-040545. (Visited on 06/11/2020).

[179] Mi Li et al. "Atomic force microscopy in characterizing cell mechanics for biomedical applications: A review". In: *IEEE Transactions on Nanobioscience* 16.6 (2017), pp. 523–540. ISSN: 15361241. DOI: 10.1109/TNB.2017.2714462.

[180] Xiaoqiong Tang et al. "Effects of substrate stiffness on the viscoelasticity and migration of prostate cancer cells examined by atomic force microscopy". en. In: *Beilstein Journal of Nanotechnology* 13.1 (June 2022). Publisher: Beilstein-Institut, pp. 560–569. ISSN: 2190-4286. DOI: 10.3762/bjnano.13.47. URL: https://www.beilstein-journals.org/bjnano/articles/13/47 (visited on 04/13/2024).

[181] Emad Moeendarbary and Andrew R. Harris. "Cell mechanics: Principles, practices, and prospects". In: *Wiley Interdisciplinary Reviews: Systems Biology and Medicine* 6.5 (2014), pp. 371–388. ISSN: 1939005X. DOI: 10.1002/wsbm.1275. (Visited on 06/12/2020).

[182] Philip Kollmannsberger and Ben Fabry. "Active soft glassy rheology of adherent cells". In: *Soft Matter* 5.9 (2009), pp. 1771–1774. ISSN: 1744683X. DOI: 10.1039/b820228a.

[183] Jeff Hardin, Gregory Bertoni, and Kelinsmith.Lewis J. *Becker's World of the Cell*. 2012.

[184] Elias H. Barriga and Roberto Mayor. "Adjustable viscoelasticity allows for efficient collective cell migration". In: *Seminars in Cell & Developmental Biology*. SI: Viscoelasticity 93 (Sept. 2019), pp. 55–68. ISSN: 1084-9521. DOI: 10.1016/j.semcdb.2018.05.027. URL: https://www.sciencedirect.com/science/article/pii/S1084952117305505 (visited on 03/18/2024).

[185] Bernat Corominas-Murtra and Nicoletta I. Petridou. "Viscoelastic Networks: Forming Cells and Tissues". In: *Frontiers in Physics* 9.June (2021), pp. 1–17. ISSN: 2296424X. DOI: 10.3389/fphy.2021.666916.

[186] Shuhuan Hu and Raymond H.W. Lam. "Characterization of viscoelastic properties of normal and cancerous human breast cells using a confining microchannel". In: *Microfluidics and Nanofluidics* 21.4 (2017). Publisher: Springer Berlin Heidelberg, pp. 1–11. ISSN: 16134990. DOI: 10.1007/s10404-017-1903-x.

[187] Qianqian Hu et al. "Label-Free and Noninvasive Single-Cell Characterization for the Viscoelastic Properties of Cryopreserved Human Red Blood Cells Using a Dielectrophoresis-On-a-Chip Approach". In: *Analytical Chemistry* 94.28 (2022), pp. 10245–10255. ISSN: 15206882. DOI: 10.1021/acs.analchem.2c01858.

[188] Torsten W. Remmerbach et al. "Oral cancer diagnosis by mechanical phenotyping". In: *Cancer Research* 69.5 (2009), pp. 1728–1732. ISSN: 00085472. DOI: 10.1158/0008-5472.CAN-08-4073.

[189] James F. Shackelford. *Introduction to materials science for engineers*. 4th ed. Upper Saddle River, N.J: Prentice Hall, 1996. ISBN: 978-0-02-409761-3.

[190] Nhan Phan-Thien and Nam Mai-Duy. *Understanding Viscoelasticity*. en. July 2017. ISBN: 978-3-319-61999-6. URL: https://link.springer.com/book/10.1007/978-3-319-62000-8 (visited on 05/04/2024).

[191] Paul A. Janmey, Penelope C. Georges, and Søren Hvidt. "Basic Rheology for Biologists". In: *Methods in Cell Biology*. Vol. 83. Cell Mechanics. Academic Press, Jan. 2007, pp. 1–27. DOI: 10.1016/S0091-679X(07)83001-9. URL: https://www.sciencedirect.com/science/article/pii/S0091679X07830019 (visited on 05/04/2024).

[192] R. IAN FRESHNEY. *Culture of Animal Cells: A Manual of Basic Technique*. arXiv: gr-qc/9809069v1 ISSN: 0717-6163. Wiley, 2005. ISBN: 978-0-471-74759-8.

[193] H. D. Soule et al. "A human cell line from a pleural effusion derived from a breast carcinoma1,2". In: *Journal of the National Cancer Institute* 51.5 (1973), pp. 1409–1416. ISSN: 14602105. DOI: 10.1093/jnci/51.5.1409.

[194] R. Cailleau et al. "Breast tumor cell lines from pleural effusions". In: *Journal of the National Cancer Institute* 53.3 (1974), pp. 661–674. ISSN: 14602105. DOI: 10.1093/jnci/53.3.661.

[195] Charles M. McGrath and Herbert D. Soule. "Renewal inhibition of human mammary cell growth in vitro: Cortisol and the recruitment of cells to terminal differentiation". In: *Journal of Cellular Physiology* 116.3 (1983), pp. 385–396. ISSN: 10974652. DOI: 10.1002/jcp.1041160317.

[196] Mark A. Labarge, James C. Garbe, and Martha R. Stampfer. "Processing of human reduction mammoplasty and mastectomy tissues for cell culture." In: *Journal of visualized experiments : JoVE* 71 (2013), pp. 1–7. ISSN: 1940087X. DOI: 10.3791/50011.

[197] James C. Garbe et al. "Molecular Distinctions between Stasis and Telomere Attrition Senescence Barriers Shown by Long-term Culture of Normal Human Mammary Epithelial Cells". In: *Cancer Research* 69.19 (Oct. 2009), pp. 7557–7568. ISSN: 0008-5472. DOI: 10.1158/0008-5472.CAN-09-0270. URL: https://doi.org/10.1158/0008-5472.CAN-09-0270 (visited on 02/06/2024).

[198] Martha Stampfer. *Human Mammary Epithelial Cell (HMEC) Bank Website*. URL: https://hmec.lbl.gov/mindex.html.

[199] Ikuko Fujiwara et al. "Latrunculin A Accelerates Actin Filament Depolymerization in Addition to Sequestering Actin Monomers". In: *Current Biology* 28.19 (2018). Publisher: Elsevier Ltd., 3183–3192.e2. ISSN: 09609822. DOI: 10.1016/j.cub.2018.07.082. URL: https://doi.org/10.1016/j.cub.2018.07.082.

[200] Martine Coué et al. "Inhibition of actin polymerization by latrunculin A". In: *FEBS Letters* 213.2 (1987), pp. 316–318. ISSN: 00145793. DOI: 10.1016/0014-5793(87)81513-2.

[201] H. Kubitschke et al. "Actin and microtubule networks contribute differently to cell response for small and large strains". In: *New Journal of Physics* 19.9 (2017). Publisher: IOP Publishing. ISSN: 13672630. DOI: 10.1088/1367-2630/aa7658.

[202] Günther Gerisch et al. "Mobile Actin Clusters and Traveling Waves in Cells Recovering from Actin Depolymerization". In: *Biophysical Journal* 87.5 (Nov. 2004), pp. 3493–3503. ISSN: 0006-3495. DOI: 10.1529/biophysj.104.047589. URL: https://www.sciencedirect.com/science/article/pii/S000634950473814X (visited on 02/06/2024).

[203] Ben Fabry et al. "Scaling the microrheology of living cells". In: *Physical Review Letters* 87.14 (2001), pp. 1–4. ISSN: 00319007. DOI: 10.1103/PhysRevLett.87.148102.

[204] Biran Wang et al. "A general approach for the microrheology of cancer cells by atomic force microscopy". In: *Micron* 44.1 (2013), pp. 287–297. ISSN: 09684328. DOI: 10.1016/j.micron.2012.07.006.

[205] M. R. Kaazempur Mofrad et al. "Exploring the molecular basis for mechanosensation, signal transduction, and cytoskeletal remodeling". In: *Acta Biomaterialia* 1.3 (2005), pp. 281–293. ISSN: 17427061. DOI: 10.1016/j.actbio.2005.02.008.

[206] Mohammad R.K. Mofrad. "Rheology of the cytoskeleton". In: *Annual Review of Fluid Mechanics* 41 (2009), pp. 433–453. ISSN: 00664189. DOI: 10.1146/annurev.fluid.010908.165236.

[207] Sundus F. Shalabi et al. "Evidence for accelerated aging in mammary epithelia of women carrying germline BRCA1 or BRCA2 mutations". en. In: *Nature Aging* 1.9 (Sept. 2021). Publisher: Nature Publishing Group, pp. 838–849. ISSN: 2662-8465. DOI: 10.1038/s43587-021-00104-9. URL: https://www.nature.com/articles/s43587-021-00104-9 (visited on 05/05/2024).

[208] Masaru Miyano et al. "Breast-Specific Molecular Clocks Comprised of ELF5 Expression and Promoter Methylation Identify Individuals Susceptible to Cancer Initiation". In: *Cancer Prevention Research* 14.8 (Aug. 2021), pp. 779–794. ISSN: 1940-6207. DOI: 10.1158/1940-6207.CAPR-20-0635. URL: https://doi.org/10.1158/1940-6207.CAPR-20-0635 (visited on 05/05/2024).

[209] Jiu-Tao Hang, Guang-Kui Xu, and Huajian Gao. "Frequency-dependent transition in power-law rheological behavior of living cells". In: *Science Advances* 8.18 (May 2022). Publisher: American Association for the Advancement of Science, eabn6093. DOI: 10.1126/sciadv.abn6093. URL: https://www.science.org/doi/10.1126/sciadv.abn6093 (visited on 05/06/2024).

[210] Kristen Cotner. "Integrated Node-Pore Sensing Techniques for Label-Free Single-Cell Measurements". English. ISBN: 9798380622585 Publication Title: ProQuest Dissertations and Theses 30246247. Ph.D. United States – California: University of California, Berkeley, 2022. URL: https://www.proquest.com/dissertations-theses/integrated-node-pore-sensing-techniques-label/docview/2884056298/se-2?accountid=14496.

[211] Michael R. Kellman et al. "Node-Pore Coded Coincidence Correction: Coulter Counters, Code Design, and Sparse Deconvolution". In: *IEEE Sensors Journal* 18.8 (2018). Publisher: IEEE, pp. 3068–3079. ISSN: 1530437X. DOI: 10.1109/JSEN.2018.2805865.

[212] Kalpana Mandal et al. "Mapping intracellular mechanics on micropatterned substrates". In: *Proceedings of the National Academy of Sciences* 113.46 (Nov. 2016). Publisher: Proceedings of the National Academy of Sciences, E7159–E7168. DOI: 10.1073/pnas.1605112113. URL: https://www.pnas.org/doi/full/10.1073/pnas.1605112113 (visited on 05/05/2024).

[213] Celine Denais and Jan Lammerding. *Nuclear Mechanics in Cancer - Cancer Biology and the Nuclear Envelope*. Vol. 773. Publication Title: Cancer Biology and the Nuclear Envelope Issue: Chapter 20. 2014. ISBN: 978-1-4899-8031-1. DOI: 10.1007/978-1-4899-8032-8. URL: http://link.springer.com/chapter/10.1007/978-1-4899-8032-8_20/fulltext.html%5Cnpapers3://publication/doi/10.1007/978-1-4899-8032-8_20.

[214] Andreas R. Bausch, Winfried Möller, and Erich Sackmann. "Measurement of Local Viscoelasticity and Forces in Living Cells by Magnetic Tweezers". In: *Biophysical Journal* 76.1 (Jan. 1999), pp. 573–579. ISSN: 0006-3495. DOI: 10.1016/S0006-3495(99)77225-5. URL: https://www.sciencedirect.com/science/article/pii/S0006349599772255 (visited on 05/06/2024).

[215] Olivia J. Scheideler et al. "Recapitulating complex biological signaling environments using a multiplexed, DNA-patterning approach". In: *Science Advances* 6.12 (Mar. 2020). Publisher: American Association for the Advancement of Science, eaay5696. DOI: 10.1126/sciadv.aay5696. URL: https://www.science.org/doi/10.1126/sciadv.aay5696 (visited on 04/08/2024).

[216] Molly Kozminsky et al. "Multiplexed DNA-Directed Patterning of Antibodies for Applications in Cell Subpopulation Analysis". In: *ACS Applied Materials & Interfaces* 13.39 (Oct. 2021), pp. 46421–46430. ISSN: 1944-8244. DOI: 10.1021/acsami.1c15047. URL: https://pubs.acs.org/doi/10.1021/acsami.1c15047.

[217] In: *Immunobiology: The Immune System in Health and Disease*. Ed. by Charles Janeway. 5. ed. New York, NY: Garland Science, 2001, Appendix II. CD Antigens. ISBN: 978-0-8153-3642-6 978-0-443-07098-3 978-0-443-07099-0. URL: https://www.ncbi.nlm.nih.gov/books/NBK10772/.

[218] Heddy Zola et al. "CD molecules 2006 — Human cell differentiation molecules". In: *Journal of Immunological Methods* 319.1 (Jan. 2007), pp. 1–5. ISSN: 0022-1759. DOI: 10.1016/j.jim.2006.11.001. URL: https://www.sciencedirect.com/science/article/pii/S002217590600336X (visited on 05/04/2024).

[219] Heddy Zola. "Medical Applications of Leukocyte Surface Molecules-the CD molecules". en. In: *Molecular Medicine* 12.11 (Nov. 2006), pp. 312–316. ISSN: 1528-3658. DOI: 10.2119/2006-00081.Zola. URL: https://doi.org/10.2119/2006-00081.Zola.

[220] "BD CD Marker Handbook". en. In: (2016). URL: https://www.bdbiosciences.com/content/dam/bdb/marketing-documents/cd_marker_handbook.pdf.

[221] Anna Meyfour et al. "The quest of cell surface markers for stem cell therapy". en. In: *Cellular and Molecular Life Sciences* 78.2 (Jan. 2021), pp. 469–495. ISSN: 1420-9071. DOI: 10.1007/s00018-020-03602-y. URL: https://doi.org/10.1007/s00018-020-03602-y (visited on 05/04/2024).

[222] Paul Carter, Leia Smith, and Maureen Ryan. "Identification and validation of cell surface antigens for antibody targeting in oncology". en_US. In: *Endocrine-Related Cancer* 11.4 (Dec. 2004). Publisher: BioScientifica Section: Endocrine-Related Cancer, pp. 659–687. ISSN: 1351-0088, 1479-6821. DOI: 10.1677/erc.1.00766. URL: https://erc.bioscientifica.com/view/journals/erc/11/4/0110659.xml (visited on 05/04/2024).

[223] Xunwu Hu and Ye Zhang. "Developing biomaterials to mediate the spatial distribution of integrins". In: *Biophysics Reviews* 2.4 (Nov. 2021), p. 041302. ISSN: 2688-4089. DOI: 10.1063/5.0055746. URL: https://doi.org/10.1063/5.0055746 (visited on 04/05/2024).

[224] Yasmin A. Kadry and David A. Calderwood. "Chapter 22: Structural and signaling functions of integrins". In: *Biochimica et Biophysica Acta (BBA) - Biomembranes* 1862.5 (May 2020), p. 183206. ISSN: 0005-2736. DOI: 10.1016/j.bbamem.2020.183206. URL: https://www.sciencedirect.com/science/article/pii/S0005273620300328 (visited on 05/04/2024).

[225] Luke R. Anderson, Thomas W. Owens, and Matthew J. Naylor. "Structural and mechanical functions of integrins". en. In: *Biophysical Reviews* 6.2 (June 2014), pp. 203–213. ISSN: 1867-2469. DOI: 10.1007/s12551-013-0124-0. URL: https://doi.org/10.1007/s12551-013-0124-0 (visited on 05/04/2024).

[226] Charles H. Streuli. "Integrins as architects of cell behavior". In: *Molecular Biology of the Cell* 27.19 (Oct. 2016). Publisher: American Society for Cell Biology (mboc), pp. 2885–2888. ISSN: 1059-1524. DOI: 10.1091/mbc.E15-06-0369. URL: https://www.molbiolcell.org/doi/10.1091/mbc.E15-06-0369 (visited on 11/29/2023).

[227] Zhiqi Sun, Mercedes Costell, and Reinhard Fässler. "Integrin activation by talin, kindlin and mechanical forces". In: *Nature Cell Biology* 21.1 (2019). Publisher: Springer US, pp. 25–31. ISSN: 14764679. DOI: 10.1038/s41556-018-0234-9. URL: http://dx.doi.org/10.1038/s41556-018-0234-9.

[228] Olachi J. Mezu-Ndubuisi and Akhil Maheshwari. "The role of integrins in inflammation and angiogenesis". en. In: *Pediatric Research* 89.7 (May 2021). Publisher: Nature Publishing Group, pp. 1619–1626. ISSN: 1530-0447. DOI: 10.1038/s41390-020-01177-9. URL: https://www.nature.com/articles/s41390-020-01177-9 (visited on 05/04/2024).

[229] Erin L. Baker and Muhammad H. Zaman. "The biomechanical integrin". In: *Journal of Biomechanics*. Special Issue on Cell Mechanobiology 43.1 (Jan. 2010), pp. 38–44. ISSN: 0021-9290. DOI: 10.1016/j.jbiomech.2009.09.007. URL: https://www.sciencedirect.com/science/article/pii/S0021929009004989 (visited on 11/28/2023).

[230] Keeley L. Mui, Christopher S. Chen, and Richard K. Assoian. "The mechanical regulation of integrin-cadherin crosstalk organizes cells, signaling and forces". In: *Journal of Cell Science* 129.6 (2016), pp. 1093–1100. ISSN: 14779137. DOI: 10.1242/jcs.183699.

[231] Shawn P. Carey, Jonathan M. Charest, and Cynthia A. Reinhart-King. "Forces During Cell Adhesion and Spreading: Implications for Cellular Homeostasis". en. In: *Cellular and Biomolecular Mechanics and Mechanobiology*. Ed. by Amit Gefen. Berlin, Heidelberg: Springer, 2011, pp. 29–69. ISBN: 978-3-642-14218-5. DOI: 10.1007/8415_2010_22. URL: https://doi.org/10.1007/8415_2010_22 (visited on 05/04/2024).

[232] Liang Zhang, Xiqiao Feng, and Shaofan Li. "Review and perspective on soft matter modeling in cellular mechanobiology: cell contact, adhesion, mechanosensing, and motility". en. In: *Acta Mechanica* 228.12 (Dec. 2017), pp. 4095–4122. ISSN: 1619-6937. DOI: 10.1007/s00707-017-2057-3. URL: https://doi.org/10.1007/s00707-017-2057-3 (visited on 05/04/2024).

[233] Nicholas M. Cronin and Kris A. DeMali. "Dynamics of the Actin Cytoskeleton at Adhesion Complexes". en. In: *Biology* 11.1 (Jan. 2022). Number: 1 Publisher: Multidisciplinary Digital Publishing Institute, p. 52. ISSN: 2079-7737. DOI: 10.3390/biology11010052. URL: https://www.mdpi.com/2079-7737/11/1/52 (visited on 05/04/2024).

[234] Wenxiu Zhao, Yvonne Li, and Xun Zhang. "Stemness-related markers in cancer". en. In: *Cancer Translational Medicine* 3.3 (2017), p. 87. ISSN: 2395-3977. DOI: 10.4103/ctm.ctm_69_16. URL: http://www.cancertm.com/text.asp?2017/3/3/87/207621 (visited on 04/05/2024).

[235] *Tumor Marker Tests in Common Use - NCI*. en. cgvArticle. Archive Location: nciglobal, ncienterprise. Jan. 2024. URL: https://www.cancer.gov/about-cancer/diagnosis-staging/diagnosis/tumor-markers-list (visited on 04/05/2024).

[236] Elahe Tahmasebi et al. "The current markers of cancer stem cell in oral cancers". In: *Life Sciences* 249 (May 2020), p. 117483. ISSN: 0024-3205. DOI: 10.1016/j.lfs.2020.117483. URL: https://www.sciencedirect.com/science/article/pii/S0024320520302319 (visited on 04/05/2024).

[237] Stephen Hearty, Paul Leonard, and Richard O'Kennedy. "Measuring Antibody-Antigen Binding Kinetics Using Surface Plasmon Resonance". en. In: *Antibody Engineering: Methods and Protocols, Second Edition*. Ed. by Patrick Chames. Methods in Molecular Biology. Totowa, NJ: Humana Press, 2012, pp. 411–442. ISBN: 978-1-61779-974-7. DOI: 10.1007/978-1-61779-974-7_24. URL: https://doi.org/10.1007/978-1-61779-974-7_24 (visited on 11/29/2023).

[238] João Crispim Encarnação et al. "Impact of assay temperature on antibody binding characteristics in living cells: A case study". In: *Biomedical Reports* 7.5 (Nov. 2017). Publisher: Spandidos Publications, pp. 400–406. ISSN: 2049-9434. DOI: 10.3892/br.2017.982. URL: https://www.spandidos-publications.com/10.3892/br.2017.982 (visited on 02/28/2024).

[239] Ruxiu Liu et al. "Combinatorial Immunophenotyping of Cell Populations with an Electronic Antibody Microarray". In: *Small* 15.51 (2019). ISSN: 16136829. DOI: 10.1002/smll.201904732.

[240] James Z. Hui et al. "LASIC: Light Activated Site-Specific Conjugation of Native IgGs". In: *Bioconjugate Chemistry* 26.8 (Aug. 2015). Publisher: American Chemical Society, pp. 1456–1460. ISSN: 1043-1802. DOI: 10.1021/acs.bioconjchem.5b00275. URL: https://doi.org/10.1021/acs.bioconjchem.5b00275 (visited on 04/10/2024).

[241] James Zhe Hui et al. "Facile Method for the Site-Specific, Covalent Attachment of Full-Length IgG onto Nanoparticles". en. In: *Small* 10.16 (2014), pp. 3354–3363. ISSN: 1613-6829. DOI: 10.1002/smll.201303629. URL: https://onlinelibrary.wiley.com/doi/abs/10.1002/smll.201303629 (visited on 04/10/2024).

[242] Chance John Luckey et al. "Differences in the Expression of Human Class I MHC Alleles and Their Associated Peptides in the Presence of Proteasome Inhibitors1". In: *The Journal of Immunology* 167.3 (Aug. 2001), pp. 1212–1221. ISSN: 0022-1767. DOI: 10.4049/jimmunol.167.3.1212. URL: https://doi.org/10.4049/jimmunol.167.3.1212 (visited on 02/15/2024).

[243] Kunikazu Tsuji et al. "Effects of Different Cell-Detaching Methods on the Viability and Cell Surface Antigen Expression of Synovial Mesenchymal Stem Cells". In: *Cell Transplantation* 26.6 (June 2017), pp. 1089–1102. ISSN: 0963-6897. DOI: 10.3727/096368917X694831. URL: https://www.ncbi.nlm.nih.gov/pmc/articles/PMC5657749/ (visited on 02/15/2024).

[244] Thermo Fisher Scientific. *Dissociation with TrypLE Express Enzyme maintains cell health and preserves surface marker expression.*

[245] "Flow Cytometry Staining Buffer (FCSB)". en. In: *Cold Spring Harbor Protocols* 2018.7 (July 2018). Publisher: Cold Spring Harbor Laboratory Press, pdb.rec104612. ISSN: 1940-3402, 1559-6095. DOI: 10.1101/pdb.rec104612.

[246] Juan Wang et al. "The analysis of viability for mammalian cells treated at different temperatures and its application in cell shipment". In: *PLoS ONE* 12.4 (Apr. 2017), e0176120. ISSN: 1932-6203. DOI: 10.1371/journal.pone.0176120. URL: https://www.ncbi.nlm.nih.gov/pmc/articles/PMC5395231/ (visited on 05/05/2024).

[247] Amelia Jerram et al. "Effects of storage time and temperature on highly multiparametric flow analysis of peripheral blood samples; implications for clinical trial samples". In: *Bioscience Reports* 41.2 (Feb. 2021), BSR20203827. ISSN: 0144-8463. DOI: 10.1042/BSR20203827. URL: https://doi.org/10.1042/BSR20203827 (visited on 05/05/2024).

[248] Sergey V. Litvinov et al. "Evidence for a Role of the Epithelial Glycoprotein 40 (Ep-CAM) in Epithelial Cell-Cell Adhesion". In: *Cell Adhesion and Communication* 2.5 (Jan. 1994), pp. 417–428. ISSN: null. DOI: 10.3109/15419069409004452. URL: https://doi.org/10.3109/15419069409004452 (visited on 04/13/2024).

[249] Johanna M. Gostner et al. "Effects of EpCAM overexpression on human breast cancer cell lines". In: *BMC Cancer* 11 (Jan. 2011). ISSN: 14712407. DOI: 10.1186/1471-2407-11-45.

[250] S. D. Soysal et al. "EpCAM expression varies significantly and is differentially associated with prognosis in the luminal B HER2+, basal-like, and HER2 intrinsic subtypes of breast cancer". In: *British Journal of Cancer* 108.7 (Apr. 2013), pp. 1480–1487. ISSN: 00070920. DOI: 10.1038/bjc.2013.80.

[251] Robert Königsberg et al. "Detection of EpCAM positive and negative circulating tumor cells in metastatic breast cancer patients". In: *Acta Oncologica* 50.5 (June 2011). Publisher: Taylor & Francis _eprint: https://doi.org/10.3109/0284186X.2010.549151, pp. 700–710. ISSN: 0284-186X. DOI: 10.3109/0284186X.2010.549151. URL: https://doi.org/10.3109/0284186X.2010.549151 (visited on 12/18/2023).

[252] Ying Qu et al. "Evaluation of MCF10A as a Reliable Model for Normal Human Mammary Epithelial Cells". en. In: *PLOS ONE* 10.7 (July 2015). Publisher: Public Library of Science, e0131285. ISSN: 1932-6203. DOI: 10.1371/journal.pone.0131285. URL: https://journals.plos.org/plosone/article?id=10.1371/journal.pone.0131285 (visited on 12/06/2023).

[253] Michael D. Walsh et al. "Heterogeneity of MUC1 expression by human breast carcinoma cell lines in vivo and in vitro". en. In: *Breast Cancer Research and Treatment* 58.3 (Dec. 1999), pp. 253–264. ISSN: 1573-7217. DOI: 10.1023/A:1006345301364. URL: https://doi.org/10.1023/A:1006345301364 (visited on 12/06/2023).

[254] Thorarinn Gudjonsson et al. "Myoepithelial Cells: Their Origin and Function in Breast Morphogenesis and Neoplasia". en. In: *Journal of Mammary Gland Biology and Neoplasia* 10.3 (July 2005), pp. 261–272. ISSN: 1573-7039. DOI: 10.1007/s10911-005-9586-4. URL: https://doi.org/10.1007/s10911-005-9586-4 (visited on 04/24/2024).

[255] Orit Katarina Sirka, Eliah R. Shamir, and Andrew J. Ewald. "Myoepithelial cells are a dynamic barrier to epithelial dissemination". In: *Journal of Cell Biology* 217.10 (2018), pp. 3368–3381. ISSN: 15408140. DOI: 10.1083/JCB.201802144.

[256] Stefan Hinz et al. "Deep proteome profiling of human mammary epithelia at lineage and age resolution". In: *iScience* 24.9 (Sept. 2021), p. 103026. ISSN: 2589-0042. DOI: 10.1016/j.isci.2021.103026. URL: https://www.sciencedirect.com/science/article/pii/S2589004221009949 (visited on 12/07/2023).

[257] Anouk Mentink et al. "Measuring antigen expression of cancer cell lines and circulating tumour cells". en. In: *Scientific Reports* 13.1 (Apr. 2023). Publisher: Nature Publishing Group, p. 6051. ISSN: 2045-2322. DOI: 10.1038/s41598-023-33179-y. URL: https://www.nature.com/articles/s41598-023-33179-y (visited on 04/13/2024).

[258] Maarten Balzar et al. "Cytoplasmic Tail Regulates the Intercellular Adhesion Function of the Epithelial Cell Adhesion Molecule". In: *Molecular and Cellular Biology* 18.8 (Aug. 1998), pp. 4833–4843. ISSN: 0270-7306. URL: https://www.ncbi.nlm.nih.gov/pmc/articles/PMC109068/ (visited on 04/13/2024).

[259] Guilhem Velve-Casquillas et al. "Microfluidic tools for cell biological research". In: *Nano Today* 5.1 (Feb. 2010), pp. 28–47. ISSN: 1748-0132. DOI: 10.1016/j.nantod.2009.12.001. URL: https://www.sciencedirect.com/science/article/pii/S1748013209001340 (visited on 05/01/2024).

[260] John Gounley, Erik W. Draeger, and Amanda Randles. "Numerical simulation of a compound capsule in a constricted microchannel". In: *Procedia Computer Science*. International Conference on Computational Science, ICCS 2017, 12-14 June 2017, Zurich, Switzerland 108 (Jan. 2017), pp. 175–184. ISSN: 1877-0509. DOI: 10.1016/j.procs.2017.05.209. URL: https://www.sciencedirect.com/science/article/pii/S1877050917308025 (visited on 05/01/2024).

[261] Marcele O. K. Mendonça, Isabela F. Apolinário, and Paulo S. R. Diniz. "Chapter 1 - Introduction to signal processing and machine learning theory". In: *Signal Processing and Machine Learning Theory*. Ed. by Paulo S. R. Diniz. Academic Press, Jan. 2024, pp. 1–34. ISBN: 978-0-323-91772-8. DOI: 10.1016/B978-0-32-391772-8.00007-7. URL: https://www.sciencedirect.com/science/article/pii/B9780323917728000077 (visited on 05/01/2024).

[262] Zijiang Zhu et al. "Classification and Reconstruction of Biomedical Signals Based on Convolutional Neural Network". en. In: *Computational Intelligence and Neuroscience* 2022 (July 2022). Publisher: Hindawi, e6548811. ISSN: 1687-5265. DOI: 10.1155/2022/6548811. URL: https://www.hindawi.com/journals/cin/2022/6548811/.

[263] Anne-Sophie Mertgen et al. "A low-fouling, self-assembled, graft co-polymer and covalent surface coating for controlled immobilization of biologically active moieties". In: *Applied Surface Science* 584 (May 2022), p. 152525. ISSN: 0169-4332. DOI: 10.1016/j.apsusc.2022.152525. URL: https://www.sciencedirect.com/science/article/pii/S0169433222001106 (visited on 05/02/2024).

[264] Karthik Ratna Balakrishnan. "Node-Pore Sensing: A Robust, High Dynamic Range Method for Multi-Parametric Screening of Biological Samples". ISBN: 9781369841091. Ph.D. University of California, Berkeley.

[265] Vasant Iyer, David A. Issadore, and Firooz Aflatouni. "The next generation of hybrid microfluidic/integrated circuit chips: recent and upcoming advances in high-speed, high-throughput, and multifunctional lab-on-IC systems". en. In: *Lab on a Chip* 23.11 (May 2023). Publisher: The Royal Society of Chemistry, pp. 2553–2576. ISSN: 1473-0189. DOI: 10.1039/D2LC01163H. URL: https://pubs.rsc.org/en/content/articlelanding/2023/lc/d2lc01163h (visited on 05/02/2024).

[266] Sina Faraji Alamouti et al. "A Sparse Sampling Sensor Front-End IC for Low Power Continuous SpO2 & HR Monitoring". en. In: *IEEE Transactions on Biomedical Circuits and Systems* 16.6 (Dec. 2022), pp. 997–1007. ISSN: 1932-4545, 1940-9990. DOI: 10.1109/TBCAS.2022.3223971. URL: https://ieeexplore.ieee.org/document/9960794/.

[267] Brian Li et al. "Evaluating sources of technical variability in the mechano-node-pore sensing pipeline and their effect on the reproducibility of single-cell mechanical phenotyping". In: *PLoS ONE* 16.10 October (2021). ISBN: 1111111111, pp. 1–19. ISSN: 19326203. DOI: 10.1371/journal.pone.0258982. URL: http://dx.doi.org/10.1371/journal.pone.0258982.